Human-Scale Ultrasound, Thermoacoustic, and Photoacoustic Tomography

Thesis by

David Christopher Garrett

In Partial Fulfillment of the Requirements
for the degree of
Doctor of Philosophy in Medical
Engineering

CALIFORNIA INSTITUTE OF TECHNOLOGY
Pasadena, California

2026
Defended February 6, 2026

David Christopher Garrett
ORCID: 0000-0002-9747-8494

ACKNOWLEDGEMENTS

I'd first like to thank my advisor, Prof. Lihong Wang, for his guidance throughout this work. Prof. Wang has the courage to take on large, meaningful projects, and he has the determination to see them through to completion. Thank you for breaking down complex problems into actionable insights and for demonstrating the power of hard work. I am thankful to all members of COILab, particularly Jinhua Xu, who was instrumental in completing this work, and Dr. Yousuf Aborahama and Dr. Donghyeon Oh for their key contributions. I also thank Dr. Yide Zhang, Dr. Li Lin, Dr. Shuai Na, Dr. Peng Hu, Dr. Alex Bengtsson, Yilin Luo, Siying Kong, Dr. Xin Tong, Karteek Dhara, Manxiu Cui, Cindy Liu, Suleyman Kahraman, and Dr. Kelvin Titimbo for the great conversations over the years. Thanks to Dr. Konstantin Maslov, Dr. Geng Ku, Dr. William Tseng, Katie Pichotta, Joanne Pineda, Christine Garske and Kathy Yi for their kind assistance. I thank my committee members, Prof. Ali Hajimiri, Prof. Azita Emami, and particularly Prof. Mikhail Shapiro for his enthusiasm and support. Thanks to Prof. Joe Kirschvink for inspiring me with new ideas and ways of thinking.

I also thank my BSc/MSc advisor Prof. Elise Fear and my high school/BSc advisor Prof. Gérard Lachapelle for their valuable mentorship. From Calgary, I particularly thank Dr. Bryce Besler, Akash Melethil, Will Robillard, Ajmer Atwal, Jéremie Bourqui, Dr. Alex Sheldon, Dr. Aaron Purchase, Callum McCormack, Simon Baruffaldi, Dr. Tushar Sharma, Dr. Anis Ben Arfi, Bruce Buffalo, and Bruce Rout for all the fun projects and adventures.

My roommates (and friends) over these years have been a great source of support and reprieve: Salvador Buse, Dr. David Millard, Dr. Sam and Logan Davis, Kian Faizi, Mari Ramirez, Jane and Nyla Miller, Dr. Musab Jilani, and Neehar Kondapaneini. I also thank my hiking buddies Andy Schacht and Dr. Gio Tomaleri for the great times in the mountains, Dylan Bannon, Megan Schill, Dr. Spencer Gordon, Samy Kamkar, and Dr. Di Wu. I thank Eryney Marrogi, Ben Andrew, Dr.

Andy York, Dr. Maria Ingaramo, and Richard Fuisz for inspiring me to work on interesting and important projects. Dr. Anand Muthusamy has been a wonderful friend and mentor to me. I thank the Midjourney team for a great few months: Dr. Tom Calloway, Alex Kristoffersen, Florian Maurer, Amaya Raphaelson, Dr. Linh Nguyen, Michael Valente, and David Holz.

My family has been an exceptional source of strength and love. I thank my parents for giving me the foundation for a happy, healthy, and fulfilled life, and for being there in my times of need. I thank my brother, for being an excellent role model and for dragging me up mountains that I could not climb alone, and Dani for her infectious joy. I thank Sanjay, Sheela, and Krish for their generous warmth and support. Lastly, I thank Shivani Pandey for being a listening ear, a caring heart, and a brilliant mind. This would not have been possible without you.

DEDICATION

To the memory of Eleanor Pow and Sheela Pandey

ABSTRACT

Modern healthcare relies on imaging modalities that visualize internal anatomy and pathology. While X-ray computed tomography (CT) and magnetic resonance imaging (MRI) provide clinically useful imaging across many applications, they face significant barriers to more frequent use: ionizing radiation limits repeated CT scanning, and MRI's high cost and long acquisition times create access disparities. Conventional handheld ultrasonography enables rapid, low-cost imaging but remains limited by narrow fields of view, operator dependence, and challenging image interpretation. Photoacoustic tomography has emerged as a promising alternative that combines optical absorption contrast with acoustic detection, offering molecular specificity without ionizing radiation. However, conventional photoacoustic imaging remains limited to depths of several centimeters, inhibiting applications in deep-tissue imaging like gastrointestinal or whole-body assessment.

In this thesis, we develop three approaches to extract clinically relevant information at human scales: ultrasound, thermoacoustic, and photoacoustic tomography. All three modalities leverage a custom 512-element, 60 cm diameter receiver array designed to detect acoustic signals across human-scale geometries. We validate these approaches through *in vivo* imaging, *ex vivo* tissue experiments, and phantom studies. First, we demonstrate ultrasound tomography of full human cross-sections in the abdomen and lower extremities, reconstructing backscatter contrast alongside quantitative maps of the speed of sound and attenuation coefficient. We show that ultrasound tomography enables visualization of features such as the liver, vasculature, muscle, and subcutaneous adipose across entire 2D human cross-sections. Second, we develop a thermoacoustic approach to guiding microwave ablation procedures. By modulating the microwave signal delivered through the probe, we record the generated thermoacoustic signals and use them to model the thermal dynamics during ablation. We show that this approach yields more accurate estimates of ablation zone geometry than standard look-up tables, which could allow for more precise ablation therapy. Third, we develop a method to extend the imaging depth of photoacoustic tomography using a wireless, ingestible capsule-based optical source. We

demonstrate imaging depth up to 12 cm, which could open the door to photoacoustic imaging of regions like the gastrointestinal tract. Together, these approaches aim to expand the range of safe, informative, and accessible imaging modalities available to patients and clinicians.

PUBLISHED CONTENT AND CONTRIBUTIONS

[**Garrett, David C.**, Jinhua Xu, Donghyeon Oh], Yousuf Aborahama, Geng Ku, Konstantin Maslov, William W. Tseng, and Lihong V. Wang. "Whole Cross-Sectional Human Ultrasound Tomography." Accepted for publication in: *Nature Biomedical Engineering.*

D.C.G. participated in the conception of the project, designed the system, constructed the system, performed experiments, analyzed the data, and wrote the manuscript.

Garrett, David C., Yousuf Aborahama, Jinhua Xu, Geng Ku, and Lihong V. Wang. "Microwave Ablation Monitoring Using Thermoacoustic and Ultrasound Tomography." In: *IEEE Journal of Microwaves* (2025). doi: 10.1109/JMW.2025.3612329

D.C.G. conceived of the project, configured the hardware, performed experiments, analyzed the data, and wrote the manuscript.

Garrett, David C. and Lihong V. Wang. "An Ingestible Light Source for Deep Photoacoustic Imaging." In: *arXiv preprint* arXiv:2601.01667 (2026).

D.C.G. participated in the conception of the project, designed and constructed the hardware, performed experiments, analyzed the data, and wrote the manuscript.

Garrett, David C., and Lihong V. Wang. "Acoustic sensing with light." In: *Nature Photonics News & Views* 15, no. 5 (2021): 324-326. doi: 10.1038/s41566-021-00804-z

D.C.G. performed the analysis and wrote the manuscript with L.V.W.

[Zhang, Yide, Zhe He, Xin Tong], **David C. Garrett**, Rui Cao, and Lihong V. Wang. "Quantum imaging of biological organisms through spatial and polarization entanglement." In: *Science Advances* 10, no. 10 (2024): eadk1495.
doi: 10.1126/sciadv.adk1495

D.C.G. helped write the manuscript.

[Titimbo, Kelvin, **David C. Garrett**, S. Süleyman Kahraman, Zhe He], and Lihong V. Wang. "Numerical modeling of the multi-stage Stern–Gerlach experiment by Frisch and Segrè using co-quantum dynamics via the Bloch equation." In: *Journal of Physics B: Atomic, Molecular and Optical Physics* 56, no. 20 (2023): 205004.
doi: 10.1088/1361-6455/acf971

D.C.G. developed initial numerical modelling software.

[He, Zhe, Kelvin Titimbo, **David C. Garrett**], S. Suleyman Kahraman, and Lihong V. Wang. "Numerical modeling of the multi-stage Stern–Gerlach experiment by Frisch and Segrè using co-quantum dynamics via the Schrödinger equation." In: *Journal of Physics B: Atomic, Molecular and Optical Physics* 56, no. 20 (2023): 205005.
doi: 10.1088/1361-6455/acef83

D.C.G. developed initial numerical modelling software.

Zhang, Yide, Binglin Shen, Tong Wu, Jerry Zhao, Joseph C. Jing, Peng Wang, Kanomi Sasaki-Capela, William G. Dunphy, **David C. Garrett**, Konstantin Maslov, Weiwei Wang, and Lihong V. Wang. "Ultrafast and hypersensitive phase imaging of propagating internodal current flows in myelinated axons and electromagnetic pulses in dielectrics." In: *Nature Communications* 13, no. 1 (2022): 5247. doi: 10.1038/s41467-022-33002-8

D.C.G. constructed the microwave transmission line used for ultrafast imaging and helped write the manuscript.

[Lin, Li, Peng Hu], Xin Tong, Shuai Na, Rui Cao, Xiaoyun Yuan, **David C. Garrett**, Junhui Shi, Konstantin Maslov, and Lihong V. Wang. "High-speed three-dimensional photoacoustic computed tomography for preclinical research and clinical translation." In: *Nature Communications* 12, no. 1 (2021): 882. doi: 10.1038/s41467-021-21232-1

D.C.G. assisted with the system construction and helped write the manuscript.

Na, Shuai, Xiaoyun Yuan, Li Lin, Julio Isla, **David C. Garrett**, and Lihong V. Wang. "Transcranial photoacoustic computed tomography based on a layered back-projection method." In: *Photoacoustics* 20 (2020): 100213. doi: 10.1016/j.pacs.2020.100213

D.C.G. assisted with experiments and helped write the manuscript.

[ ], equal contribution.

TABLE OF CONTENTS

Acknowledgements .... *iii*
Dedication .... *v*
Abstract .... *vi*
Published Content and Contributions .... *viii*
Table of Contents .... *x*
List of Figures and Tables .... *xii*
Abbreviations .... *xiv*
Introduction *1*
    Background and Motivation **1**
    Thesis Outline **4**
Whole Cross-Sectional Human Ultrasound Tomography *5*
    Introduction **6**
    Results **8**
        Whole cross-sectional human imaging 8
        Human adipose imaging 13
        Biopsy needle localization 16
    Discussion **18**
    Supplementary Information **22**
        Acquisition parameters 22
        Reflection-mode reconstruction algorithm 23
        Reflection-mode image quality 24
        Human imaging protocol 25
        Comparison to other modalities 27
        Additional human images 29
        Straight-ray transmission-mode reconstruction algorithm 33
        Transmission-mode reconstruction accuracy 35
        Transmitter lens correction 38
        Biopsy needle acoustic modes 39
        Adipose thickness estimation 40
Microwave Ablation Monitoring using Thermoacoustic and Ultrasound Tomography *45*
    Introduction **45**
    Methods **47**
        Thermoacoustic signal generation 48
        System hardware 52
        Image reconstruction 54
        Thermal modelling 55
    Results **57**

Discussion **61**

Supplementary Information **63**
System hardware 63
TA amplitude variation during the ablation procedure 63
Scaling TA images to heating functions 64
Comparison with thermometer 65
Thermal solver 65
Ablation widths for all samples 67

An Ingestible Light Source for Deep Photoacoustic Imaging ***69***

Introduction **69**

Methods **71**
Optical excitation 72
Acoustic power transfer 73
Wireless triggering 76

Results **78**

Discussion **80**

Supplementary Information **82**
Sensitivity analysis 82
Image generation 84
Acoustic power transfer 85
Device construction 87

Conclusion ***89***

Summary of Contributions **89**

Limitations **90**
Water immersion coupling 90
Acoustic heterogeneity and shadowing 90
Two-dimensional imaging 90

Future Outlook **91**
Enabling technologies 91
Toward longitudinal diagnostic imaging 91

Appendix A: Custom System Hardware ***93***
Ultrasonic receiver array 93
Acoustic receiver characterization 96
Imaging system construction 97

Appendix B: Acoustic Sensing With Light ***99***

Bibliography ***105***

LIST OF FIGURES AND TABLES

List of Figures

Figure 1.1. Historical development of wide field-of-view ultrasound imaging. 3
Figure 2.1. UST system for whole cross-sectional human imaging. 9
Figure 2.2. Whole cross-sectional UST of a healthy adult female (Subject 1).................11
Figure 2.3. Example reflection-mode UST images of a healthy female's abdomen (Subject 1) compared with T1-weighted MRI. 12
Figure 2.4. Quantitative tissue property mapping from transmission-mode UST in a healthy female (Subject 2). 13
Figure 2.5. Abdominal adipose imaging in healthy volunteers. 15
Figure 2.6. UST-guided biopsy needle localization...18
Figure 2.7. Each elevational scan of a female (Subject 1) from approximately the ribcage to the pelvis. 29
Figure 2.8. Reconstructed speed of sound for an adult female (Subject 1). 30
Figure 2.9. Reconstructed attenuation coefficient for an adult female (Subject 1). 31
Figure 2.10. Example images for three additional subjects. 32
Figure 2.11. In-plane and elevational resolution assessment..25
Figure 2.12. Signal processing flow for transmission-mode analysis. 33
Figure 2.13. Example cross-correlated transmission signals for water-only and the human abdomen. 34
Figure 2.14. Comparison of literature [37] and UST estimations of tissue speed of sound. 37
Figure 2.15. Comparison of UST transmission-mode estimations for a healthy subject's liver acoustic properties. 37
Figure 2.16. Determining the effective focal length for various pixel angles using a cylindrical TPX lens on the acoustic transmitter. 39
Figure 2.17. Expected acoustic modes in an unmodified biopsy needle. 40
Figure 2.18. Estimating adipose thickness in a phantom..42
Figure 2.19. Additional adipose comparisons between UST and MRI. 43
Figure 2.20. Abdominal adipose thickness assessment of healthy volunteers. 44
Figure 3.1. Overview of the methodology for thermoacoustic (TA) ablation monitoring. UST: ultrasound tomography...48
Figure 3.2. Modulating waveform and expected TA source signal structure. 51
Figure 3.3. System hardware for thermoacoustic ablation monitoring.............................53
Figure 3.4. Recorded and deconvolved TA signals for the ablation probe in water..........54
Figure 3.5. Scaling TA images to a heating function using the temperature-dependent coefficient of thermal expansion..58
Figure 3.6. Estimated ablation zones from TA ablation monitoring, UST, and photographs of dissected samples. 59
Figure 3.7. Photograph of an ex vivo bovine liver sample before ablation. 63
Figure 3.8. Example mean TA image amplitude near the probe during a 1-minute ablation...64

Figure 3.9. Determining the scaling factor K between TA images and heating function. 64
Figure 3.10. Extracting fiber thermometer location from UST and comparing estimated temperature against UST model..........65
Figure 3.11. Validating our thermal solver against a theoretical solution for an instantaneous 3D Gaussian thermal source..........67
Figure 3.12. Estimated ablation zones in the plane normal to the ablation probe from UST. 68
Figure 3.13. Estimated ablation zones in the plane normal to the ablation probe from photographs of dissected samples. 68
Figure 4.1. Wireless photoacoustic tomography device. 72
Figure 4.2. Optical excitation module..........73
Figure 4.3. Acoustic power transfer for wireless photoacoustic tomography. 76
Figure 4.4. Wireless triggering circuit. 78
Figure 4.5. WPAT device operation with acoustic power transfer through 12 cm of water. 79
Figure 4.6. Experimental configuration and results for WPAT phantom imaging..........80
Figure 4.7. Example recorded signals using WPAT excitation. 83
Figure 4.8. Example image from a single device location during raster-scanning. 84
Figure 4.9. Simulated acoustic beam profile for acoustic power transfer. 85
Figure 4.10. Example rectified voltage from the acoustic receiver to the capacitor bank used to energize the pulsed laser diode array..........86
Figure 4.11. Wireless photoacoustic device construction..........88
Figure A.1. Steps of the acoustic receiver array construction. 95
Figure A.2. Human-scale, ultrasound-based imaging hardware..........96
Figure A.3. Normalized frequency response the receiver array. 96
Figure A.4. Additional details of the human-scale imaging system construction. 97
Figure A.5. Potential adaptation of our system to enable immersion-free abdominal imaging. 98
Figure B.1. Comparison of NEPD between an example optical sensor [146] and typical piezoelectric transducers in the two variants of PAT. 104

List of Tables

Table 2.1. Comparison of abdominal imaging modalities. 27
Table 2.2. Comparison of adipose assessment modalities. 28
Table 2.3. Comparison of modalities for biopsy needle localization. 28
Table 2.4. Estimated speed of sound in m/s for ethanol-water mixtures. 36
Table 3.1. Estimated ablation widths from the manufacturer specifications, ultrasound tomography, thermoacoustic modelling, and photographs of the dissected tissues. 60

ABBREVIATIONS

2D. Two-dimensional

3D. Three-dimensional

BMI. Body mass index

CE. Capsule endoscopy

CNR. Contrast-to-noise ratio

CW. Continuous-wave

DAQ. Data acquisition module

FET. Field-effect transistor

FOV. Field-of-view

FWHM. Full width at half maximum

GI. Gastrointestinal

LiDAR. Light detection and ranging

MI. Mechanical index

MRI. Magnetic resonance imaging

MW. Microwave

MWA. Microwave ablation

NA. Numerical aperture

NEP. Noise-equivalent pressure

NEPD. Noise-equivalent pressure density

NIR. Near infrared

PAM. Photoacoustic microscopy

PAT. Photoacoustic tomography

PCB. Printed circuit board

PDMS. Polydimethylsiloxane

PVDF-TrFE. Polyvinylidene fluoride-trifluoroethylene (a piezoelectric material)

PZT. Lead zirconate titanate (a piezoelectric material)

RF. Radio frequency

SA. Subcutaneous adipose

SNR. Signal-to-noise ratio

SOS. Speed of sound

TA. Thermoacoustic

TPX. Polymethylpentene (used for acoustic lenses)

US. Ultrasound

WPAT. Wireless photoacoustic tomography

X-ray CT. X-ray computed tomography

Chapter 1

INTRODUCTION

Background and Motivation

Medical imaging plays a foundational role in modern healthcare by enabling visualization of internal anatomy and pathology that cannot be assessed through physical examination alone. The modalities available to the clinician are fundamentally constrained by the physics of tissue-penetrating energy and the contrast mechanisms generated through tissue interactions. Different energy forms (e.g., X-rays, electromagnetic fields, acoustic waves, or light) offer tradeoffs between spatial resolution, imaging depth, tissue contrast, temporal resolution, safety, and cost. System-level design choices (hardware and acquisition strategies) and modality-specific parameters (e.g., X-ray photon energy, magnetic field strength, or acoustic frequency) further shape these tradeoffs.

X-ray imaging, first demonstrated by Röntgen in 1895 [1], enables human-scale imaging based on contrast from tissue atomic number and density. X-ray-based techniques remain widely used in mammography, body composition analysis, and routine diagnostics. The later development of X-ray computed tomography (CT), enabled by advances in computing hardware and reconstruction algorithms [2], allows for the visualization of 3D volumes of tissue. Recent extensions of X-ray CT, such as photon-counting CT [3] and high-resolution peripheral quantitative CT [4], aim to further improve imaging resolution, contrast, and sensitivity. However, X-ray imaging fundamentally relies on ionizing radiation. While this is justified for many clinical indications such as surgical planning and acute diagnosis, repeated or population-level screening remains constrained by cumulative radiation dose.

Magnetic resonance imaging (MRI), developed in the 1970s based on advances in nuclear magnetic resonance [5], [6], [7], enables non-ionizing tissue visualization through contrast derived from proton density and relaxation properties. MRI has become the workhorse modality in neuroimaging, musculoskeletal assessment, and oncologic evaluation, where its superior soft-tissue contrast surpasses that of X-ray CT. Nevertheless, MRI remains limited by its long acquisition times and high cost. Clinical MRI systems typically cost over $1 million [8], with total installation costs (including facility construction and electromagnetic shielding) reaching $3-5 million. Operating expenses add substantially to this burden, including maintenance contracts (>$100k/year), helium costs, and energy consumption [9]. This economic barrier leads to global disparities in access: while the United States maintains relatively high MRI availability (~35 units per million population [10]), many developed nations like Canada have only 10 per million, and low-income countries often have fewer than 1 per million. MRI also remains unsuitable for patients with some implanted devices or claustrophobia, further limiting its clinical applicability. Although some companies have recently introduced direct-to-consumer MRI services for screening applications [11], scan costs exceeding $1000 remain prohibitive for routine use in many populations and are not conducive to frequent imaging.

Medical ultrasound imaging was first investigated in the mid-20th century using single-element transducers, either in water immersion tanks [12] or using articulating arms [13]. Initial results were promising, but the imaging acquisition was slow (minutes to hours) and image quality was poor, with only bistable (binary) display capability (Figure 1.1). Since then, the handheld probe with linear array transducers has become the most common form of diagnostic ultrasound, enabling real-time imaging. However, conventional ultrasound remains limited by its narrow field of view and imaging depth, operator dependence and training requirements, and challenging image interpretation. Extended field-of-view (also known as panoramic) ultrasound has been developed to image larger anatomical regions like the abdomen and lower extremities, where a handheld probe is continuously scanned across the skin while software stitches individual frames together (Figure 1.1d) [14]. While this approach expands the anatomical coverage, it inherits the operator dependence of conventional ultrasound and introduces additional challenges from image registration.

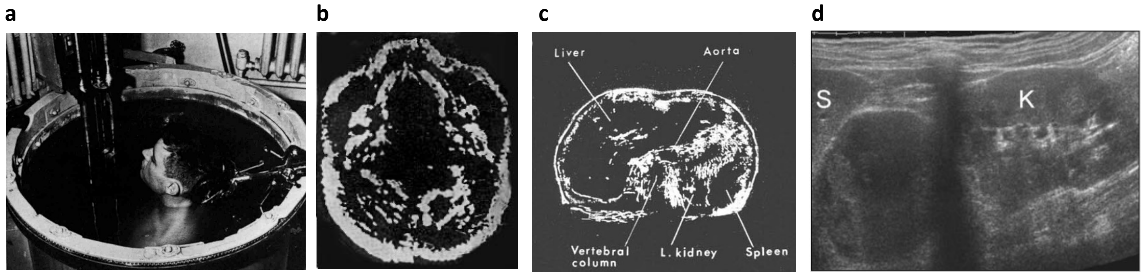

Figure 1.1. Historical development of wide field-of-view ultrasound imaging. **a**, Water immersion acoustic imaging system in 1957. **b**, Resulting "sonagram" of the human neck [15]. **c**, Early bistable images from a single-element articulating arm imaging approach [13]. **d**, Extended field-of-view ultrasound images of the abdomen obtained by co-registering multiple B-mode images from a scanned linear probe [14]. S: spleen. K: kidney.

For human-scale imaging, CT, MRI, and conventional ultrasound each exhibit fundamental limitations that restrict their use in certain clinical contexts. These constraints are particularly acute in procedure guidance applications such as needle biopsy and thermal ablation, where a safe method of real-time, wide-field visualization with good tissue differentiation is needed. Emerging modalities aim to fill these gaps by exploiting alternative contrast mechanisms. Photoacoustic tomography (PAT), for instance, captures rich optical absorption contrast from tissue chromophores while achieving imaging depths beyond the optical diffusion limit by detecting ultrasound waves generated through the photoacoustic effect. This hybrid approach combines the molecular specificity of optical imaging with the penetration depth and spatial resolution of ultrasound, positioning it as a complementary modality that may address unmet clinical needs in applications like human breast [16], brain [17], or extremities [18] imaging. However, scaling PAT to human-sized fields-of-view introduces challenges in optical delivery and acoustic detection geometry.

This thesis aims to overcome these challenges by performing human-scale imaging using three forms of contrast: acoustic (backscatter, speed of sound, and attenuation), microwave absorption, and optical absorption. While these contrast mechanisms arise from different physical phenomena, each of the techniques developed in this thesis involves the detection of low-MHz ultrasound signals which are either generated directly by acoustic waves (ultrasound tomography), induced by microwave absorption (thermoacoustic tomography) or through optical absorption (photoacoustic tomography).

Thesis Outline

The thesis is organized as follows. Chapter 2 presents a method for whole cross-sectional human ultrasound tomography of human anatomy. By revisiting configurations used by early ultrasound pioneers (water immersion and mechanical scanning) we generate *in vivo* images of the entire human cross-section in regions like the abdomen and lower extremities. In addition to reflection-mode images, this approach generates quantitative speed of sound and attenuation coefficient maps. We also develop an approach for video-rate biopsy needle localization over a human-scale field-of-view. Chapter 3 develops an approach for monitoring microwave ablation treatments using thermoacoustic detection and thermal modelling. We find that with modest modifications to existing clinical systems (using a modulated microwave source rather than continuous-wave), we can generate detectable thermoacoustic signals which relate to the thermal deposition in tissues. These signals can then be used to model the thermal dynamics in tissue, allowing for the estimation of the ablated tissue region. Chapter 4 develops a method for “inside-out” photoacoustic imaging using a wireless optical source in an ingestible capsule form factor. Such an approach could enable imaging of internal organs inaccessible to the external illumination conventionally used in photoacoustic imaging. Chapter 5 summarizes these contributions and discusses future directions for clinical translation.

Chapter 2

WHOLE CROSS-SECTIONAL HUMAN ULTRASOUND TOMOGRAPHY

[Garrett, David C., Jinhua Xu, Donghyeon Oh], Yousuf Aborahama, Geng Ku, Konstantin Maslov, William W. Tseng, and Lihong V. Wang. "Whole Cross-Sectional Human Ultrasound Tomography." Accepted for publication in: *Nature Biomedical Engineering.*

Abstract

Ultrasonography is a vital component of modern clinical care, with handheld probes routinely used for diagnostic imaging and procedural guidance. However, handheld ultrasound imaging is limited by factors such as the partial cross-sectional field of view, operator dependency, contact-induced distortion, and lack of transmission contrast. Here, we demonstrate a new system that enables whole cross-sectional ultrasound tomography of humans in both reflection and transmission modes. We generate 2D images of the entire *in vivo* human cross-section in the abdomen and thighs with uniform in-plane resolution using a custom 512-element circular ultrasound receiver array and a rotating transmitter. Sequential scans with our system show strong agreement with clinical MRI counterparts. To address unmet clinical needs, we explore two key applications. First, we observe abdominal adipose distributions in our images, enabling adipose thickness assessment without ionizing radiation or mechanical deformation. Second, we demonstrate an approach for video-rate biopsy needle localization with respect to internal tissue features. These capabilities make whole cross-sectional ultrasound tomography a potential practical tool for clinical needs currently unmet by other modalities.

Introduction

Since its inception in the mid-20th century, ultrasound imaging has revolutionized healthcare by enabling non-invasive and affordable visualization of soft tissue structure and function. Early systems employed single transducers scanned linearly or circularly with subjects immersed in a water bath [12], [19], later followed by membranes or articulating arms to image regions in the abdomen [13], [20]. Initial results were promising for disease diagnosis [21], but imaging required mechanical scanning over ~1 hour [22]. Later developments in transducers and electronics led to linear probes [23], where multiple channels could be used in parallel. These advances enabled the modern handheld probe, which has become the predominant form of ultrasonography across many clinical applications. However, probes require trained operation [24], have limited ability to visualize features behind bone or air pockets, and provide only reflection-mode images over a narrow field of view (FOV). The FOV can be expanded by scanning the probe around the periphery of regions like the human thigh and co-registering adjacent frames [25], [26]. However, existing approaches require manual probe movement to maintain contact with the skin, which can lead to image variation between operators and systems [14], [27].

More recently, alternate approaches using smaller immersion tanks with planar [28], linear [29], ring [30], or hemispherical [31] transducer arrays have been investigated for ultrasound tomography (UST) imaging of the breast [32] or limbs. These systems record both reflected and transmitted signals, allowing for the generation of reflectivity, speed of sound, and attenuation coefficient profiles. The extension to human-scale imaging has been historically constrained by acoustic propagation barriers, particularly at bone and air interfaces, where extreme impedance mismatches obstruct wave transmission. Nevertheless, a recent study achieved whole-cross-sectional imaging of ~12 cm diameter piglets post-mortem despite the presence of bone and air [33]. Although this method produces high-quality images, it requires substantial data acquisition time (15 – 25 minutes) and reconstruction time (20 – 25 minutes). Such extended protocols are challenging to adapt to *in vivo* human imaging due to subject motion. These times also rival those of MRI, which may limit the practicality and scalability of the technique in clinical settings. Another recent system enables volumetric reflection-mode imaging of vasculature and bones in human extremities like the arm [34]. However, both of these systems' parameters (e.g., array dimensions, acoustic frequency and power, and detection sensitivity) are not yet suitable for human-scale imaging in regions like the adult human abdomen.

In this work, we developed a system that enables UST of the entire human cross-section, resulting in 2D images of reflectivity, speed of sound, and attenuation coefficient profiles. We constructed a custom 512-element circular receiver array combined with a single-element transmitter that rotates around the subject. This geometry enables both reflection- and transmission-mode imaging with improved robustness to acoustic occlusions, while maintaining practicality for *in vivo* human abdominal imaging compared to planar or hemispherical alternatives. To image deep in the body, we enhance the signal sensitivity by using low-noise parallel preamplifiers directly coupled with the receiver array and by exciting the transmitter with a chirp waveform. Compared to handheld probes, we reduce issues of acoustic shadowing from regions containing bone or air pockets by using full 360° viewing angles. In comparison to MRI and other standard imaging modalities, whole cross-sectional UST is a potential low-cost, safe, fast, and convenient tool for screening and monitoring abdominal conditions.

We demonstrate this technique by imaging cross-sections of the abdomen and legs of healthy volunteers, where we clearly observe several organs and key features in reflection-mode images, and we obtain profiles of speed of sound and attenuation coefficient. This approach visualizes abdominal adipose layers, offering a promising modality for mapping adipose thickness distributions without ionizing radiation or tissue compression. We also demonstrate a method for localizing biopsy needle tips deep in tissue with respect to internal features. By coupling an acoustic transmitter to a commercial needle and detecting the resulting scattered signals from the needle tip, we obtain 30-frame-per-second images of the needle tip location. Together, these techniques showcase whole cross-sectional UST as a safe and practical modality for a variety of clinical applications.

Results

Whole cross-sectional human imaging

We developed a custom 60 cm diameter, 512-element circular acoustic receiver array with 1 MHz center frequency (Appendix A). A 1.5-inch-diameter transducer (Olympus V395) with a custom cylindrical diverging polymethylpentene (TPX) lens is used as a transmitter, and it is mounted on a plastic gear that rotates around the subject using a stepper motor. All receiver channels are preamplified using custom circuit boards within the array (Figure A.1), and these signals are digitized in parallel using two data acquisition modules (DAQs, Photosound Legion) housed in shielded enclosures. The array is mounted on two vertical motor stages to adjust its height in a water immersion tank. Water acts as acoustic coupling between the skin and transducers. An arbitrary function generator (Siglent SDG2042X) connected to a 300-Watt RF power amplifier (ENI A300) excites the transmitter. The system hardware is shown in Figure 2.1a.

To enhance the signal-to-noise ratio (SNR) without exceeding the mechanical index (MI) safety standard, we use a 400 μs chirp signal spanning 0.3 – 2.0 MHz. We first record the transducer response using only water in the imaging domain, which is then cross-correlated with the target response to recover a pulse-like representation. We display example signals from the receiver array for water and the human abdomen in Figure 2.1d-e, showing both backscattered and transmitted signals recorded in parallel. Figure 2.1f shows pulse-compressed signals obtained through cross-correlation with the water reference. This approach also enables channel calibration using the water scan, where we expect the same received amplitude for channels directly opposite the transmitter.

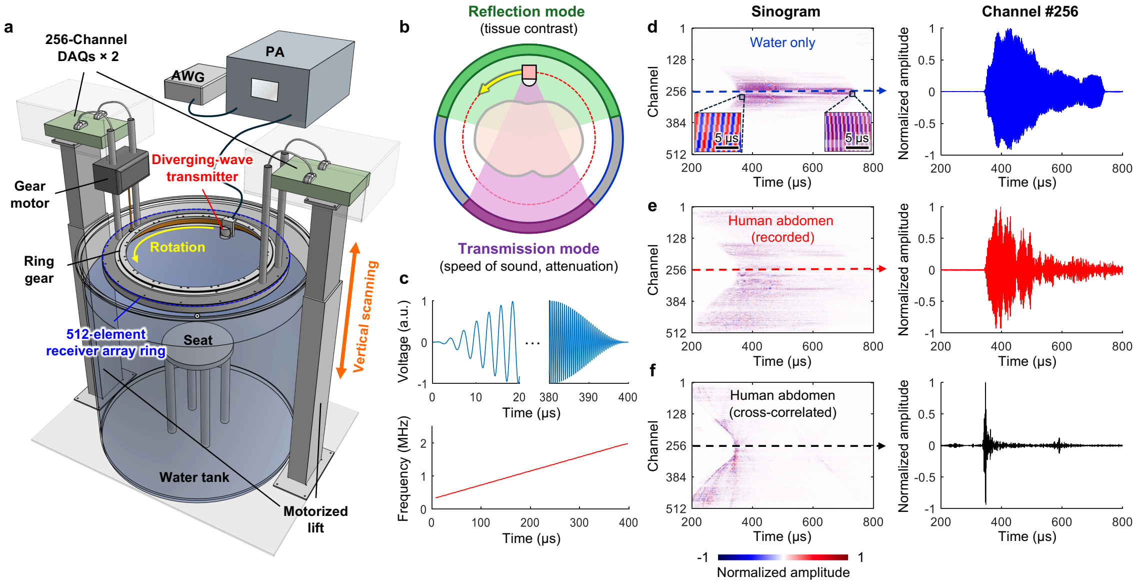

Figure 2.1. UST system for whole cross-sectional human imaging. **a**, System diagram. AWG, arbitrary waveform generator; PA, power amplifier; DAQs, data acquisition modules. **b**, Schematic diagram of the orbiting single-element transmitter and receiver ring array. During a 10-second scan, the diverging-wave transmitter rotates around the body while all 512 receivers record the backscattered (reflection mode) and transmitted (transmission mode) signals. The colored sectors on the receiver ring indicate the acoustic aperture window for reflection imaging (green, 160° angular aperture) and transmission imaging (purple, 90° aperture), which provide tissue contrast and quantitative parameters such as speed of sound or attenuation coefficient, respectively. **c**, Chirp excitation waveform. Top, temporal profile of the amplified chirp-encoded waveform coupled to the transmitter, with Hamming window apodization at the beginning and end of the signal. Bottom, instantaneous frequency of the 400 μs chirp spanning 0.3–2.0 MHz. **d-f**, Demonstration of pulse compression in received time-domain channel data. The left column shows sinograms, while the right column shows a recorded signal profile from channel 256 (dashed line in sinogram). **d**, Reference recording in water. Inset panels display the initial and terminal segments of the chirp pulse, highlighting the gradual increase in frequency content. **e**, Raw signal recorded from the human abdomen. **f**, Pulse-compressed signal obtained by cross-correlating **e** with the corresponding water reference, demonstrating recovery into a sharp profile.

We demonstrate cross-sectional UST in healthy volunteers. For abdominal imaging, subjects sit on a stool in the water immersion tank with their head supported against a cushion to reduce motion and with their arms raised to elevate the rib cage. During a 10-second scan, subjects are asked to hold their breath while remaining motionless. Figure 2.2a shows example reflection-mode images of the abdomen of a 31-year-old female volunteer (Subject 1). The images are displayed in inverse grayscale (brighter regions are more anechoic) normalized to the peak pixel amplitude. The outer boundary is extracted using an automated segmentation tool [35]. We performed scans at 1 cm vertical intervals, from approximately the rib cage to the pelvis. The subject was in the immersion tank for approximately 10 minutes over the entire imaging session. With the same volunteer standing in the immersion tank, we also imaged the thighs (Figure 2.2b) where the femur, surrounding muscle groups, and adipose boundaries are observed.

We compare our abdominal images with T1-weighted images from 3-Tesla MRI (Siemens Prisma) in Figure 2.3. The elevational slices between UST and MRI are aligned using the navel as a reference point. UST visualizes various structures, such as the liver, stomach, kidneys, abdominal aorta, vena cava, and vertebral body. We labeled regions using an anatomical atlas and through consultation with a clinical collaborator. Supplementary Video 2.1 compares the UST and MRI images across all slices. Note that despite the presence of bone and potential air pockets, our geometry enables imaging of regions deep in the body. Due to our lower acoustic frequency compared to that in typical probe-based ultrasonography, our images primarily correspond to reflections from tissue boundaries rather than scattering within tissues [36].

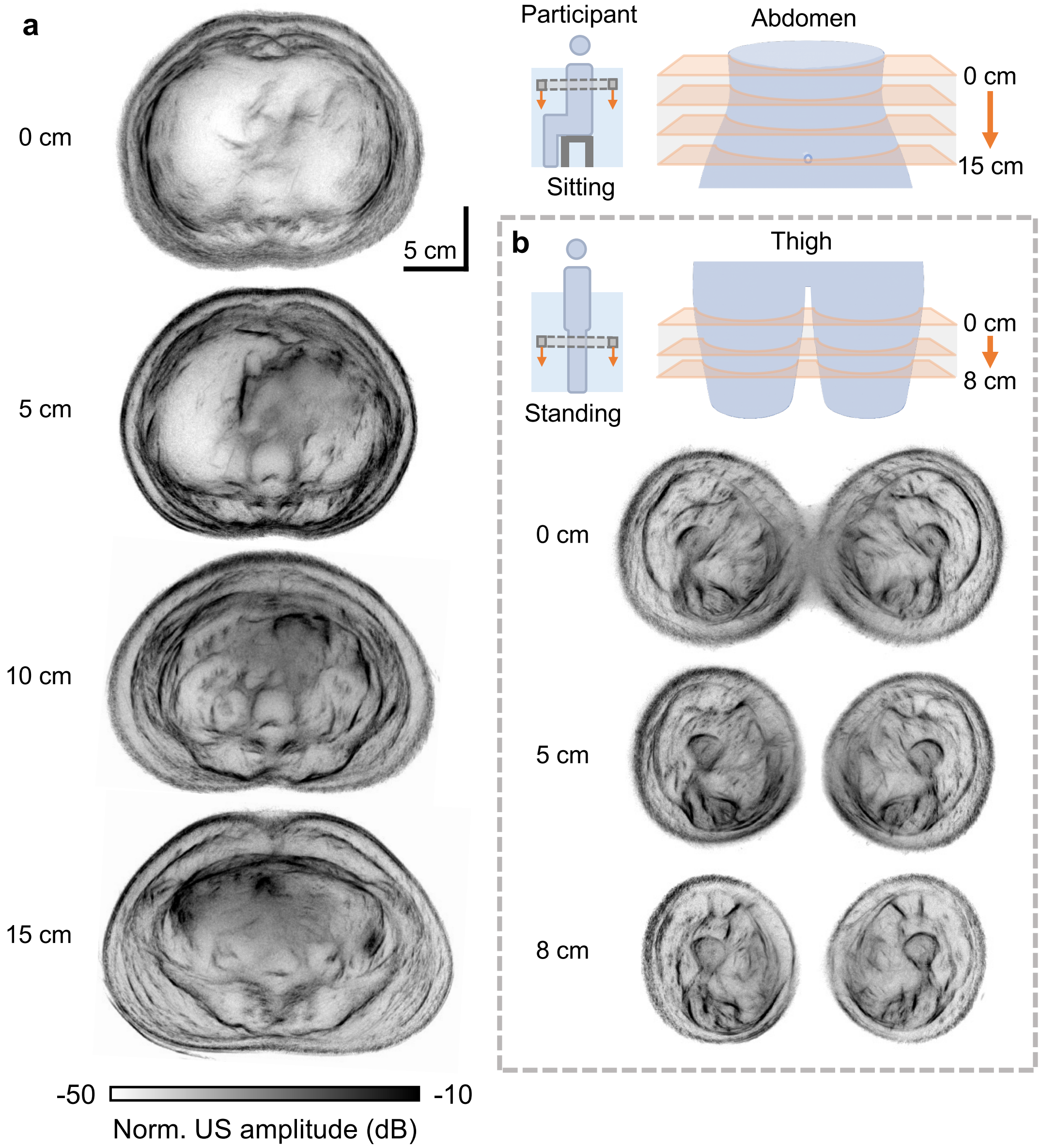

Figure 2.2. Whole cross-sectional UST of a healthy adult female (Subject 1). **a**, Serial UST slices of the abdomen spanning from approximately the ribcage to the pelvis, acquired with the subject seated in the water immersion tank. The sequential cross-sections delineate abdominal organs, musculature, and adipose distributions. **b**, UST images of the thighs acquired with the subject standing in the tank, demonstrating clear separation of subcutaneous fat and musculoskeletal compartments. Full scanned image sequences are available in Figure 2.8.

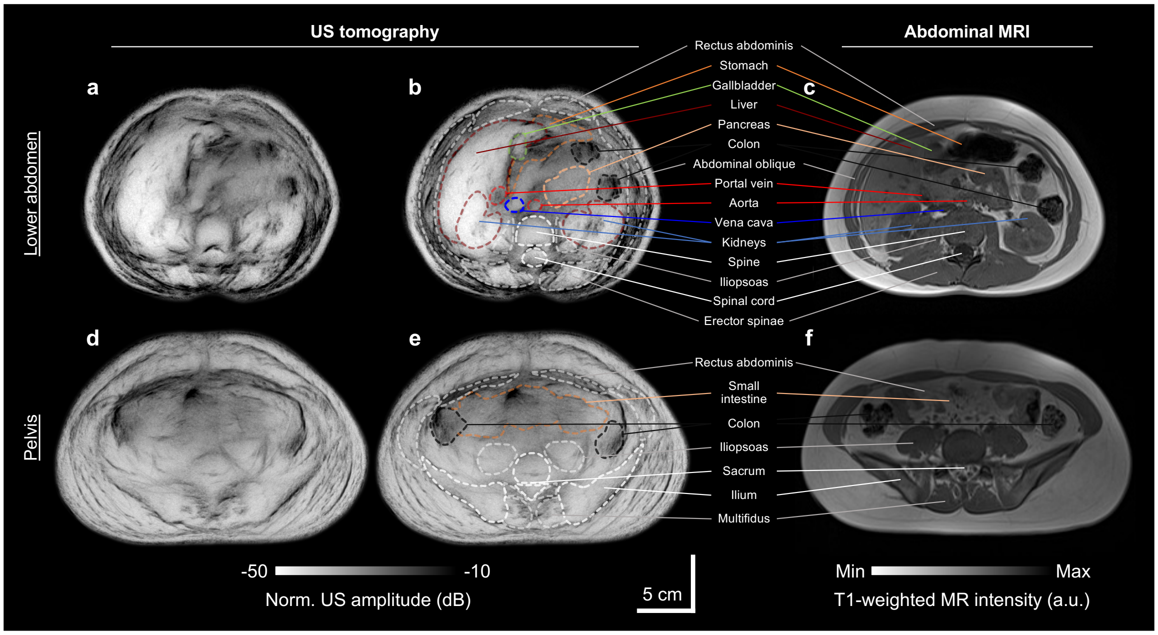

Figure 2.3. Example reflection-mode UST images of a healthy female's abdomen (Subject 1) compared with T1-weighted MRI. **a**, Unlabeled reflection-mode UST image 6 cm inferior to the starting position. **b**, Labeled UST image identifying various organs and structures. **c**, T1-weighted MRI image of a corresponding region. **d**, Unlabeled UST image 15 cm inferior to the starting position. **e**, Labeled UST image. **f**, MRI image of a corresponding region.

Acoustic signals transmitted through the body enable reconstruction of speed of sound and attenuation coefficient maps by comparing arrival time and amplitude, respectively, with those from the water-only scan. We show example reconstructions for a 23-year-old female volunteer (Subject 2) overlaid on reflection-mode images in Figure 2.4c-d. The liver exhibits a higher speed of sound than surrounding organs, consistent with literature values [37], while elevated attenuation is observed in the spine and stomach. Overall, the measured values are in good agreement with literature reports for multiple organs, including the liver (Figure 2.14). To validate this method, we imaged reference ethanol–water mixtures containing five targets (~3 cm diameter) with speeds of sound ranging from 1510 to 1610 m/s. Our estimates demonstrated less than 3% error (Table 2.4), supporting the potential of this approach for quantitative evaluation of conditions such as liver fibrosis and non-alcoholic fatty liver disease [38]. We show the reconstructed speed of sound and attenuation coefficient for Subject 1 in Figure 2.9 and Figure 2.10.

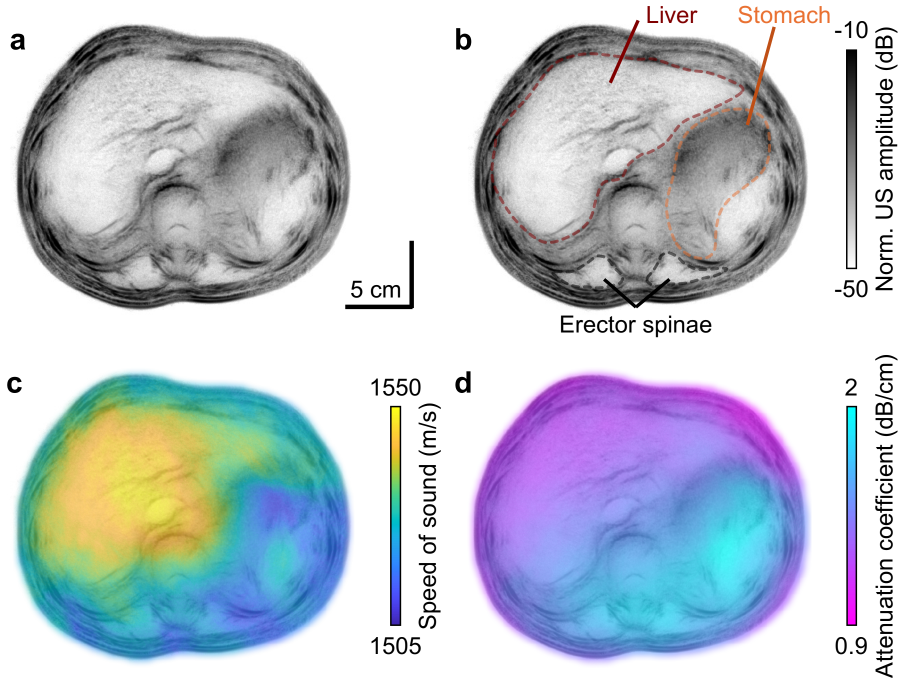

Figure 2.4. Quantitative tissue property mapping from transmission-mode UST in a healthy female (Subject 2). **a**, Reflection-mode UST image, and **b**, with representative organs and anatomical landmarks labeled (liver, stomach, erector spinae). **c**, Speed of sound overlaid on **a**, demonstrating distinct acoustic velocities across different tissue compartments. **d**, Attenuation coefficient map overlaid on **a**, highlighting contrast between tissue regions.

Human adipose imaging

Subcutaneous adipose (SA) and preperitoneal adipose (PA) distributions serve as key indicators of metabolic health [39]. SA thickness can be measured with calipers and probe-based ultrasound. Calipers are known to be less accurate for individuals with larger SA thickness, are operator-dependent, and have only moderate agreement with estimates from MRI [40]. Probe-based ultrasound, though more accurate and capable of measuring PA thickness than calipers [41], requires extensive operator training and suffers from probe-induced tissue compression [42]. Both methods also require instrument repositioning at each measurement site, making frequent whole-body adipose distribution assessment impractical [43]. We compare our approach with existing methods in Table 2.2.

Cross-sectional UST offers unique advantages for SA assessment by enabling clear visualization of the adipose layers around the abdominal periphery without mechanical deformation. To validate this approach, we first imaged a phantom consisting of a lard layer of varying known thicknesses, held in place with plastic ribbon over a 4% agar core. We extracted the reflection-mode image amplitude along lines normal to the phantom surface. We estimated the lard layer thickness by determining the distance between the two dominant peaks along this line (Figure 2.18). Our estimated thicknesses of 1.04 ± 0.02 cm and 2.02 ± 0.05 cm agree well with the true values of 1.00 cm and 2.00 cm, respectively, despite a lower speed of sound in lard (~1440 m/s versus ~1500 m/s in water).

We compare *in vivo* adipose regions identified by UST and fat-only T1-weighted MRI in Figure 2.5a-d in Subject 1. This subject has a body mass index (BMI) of $18.8 \text{ kg} \cdot \text{m}^{-2}$. Two distinct SA layers are visible: the superficial adipose layer (SAL) and the deep adipose layer (DAL). We extract profiles in the UST and MRI images to estimate the SA thickness along three lines (Figure 2.5b-d). We estimate the thickness using the two dominant amplitude peaks for UST and the 50% normalized intensity crossings for MRI. Since the MRI images are acquired with the subject in the supine position, we choose regions that are less susceptible to adipose deformation [43]. The measurements show very close agreement, with differences of less than 1 mm between UST and MRI. Additional profiles are shown in Figure 2.19. We then imaged a 27-year-old male volunteer (Subject 3) with BMI of $25.1 \text{ kg} \cdot \text{m}^{-2}$ and greater SA thickness (Figure 2.5e). The anterior side of the abdomen clearly shows the SA and PA regions relative to the skin surface and rectus abdominus muscles. Within the SA, we observe the SAL and DAL, separated by the superficial (or Scarpa's) fascia [44], [45], [46]. We show additional images for Subject 3 in Figure 2.20. Since whole cross-sectional UST is fast, safe, and more cost-effective than MRI, it shows promise for guiding and assessing weight loss regimes, clinical trials of weight loss drugs, or liposuction planning and evaluation [47].

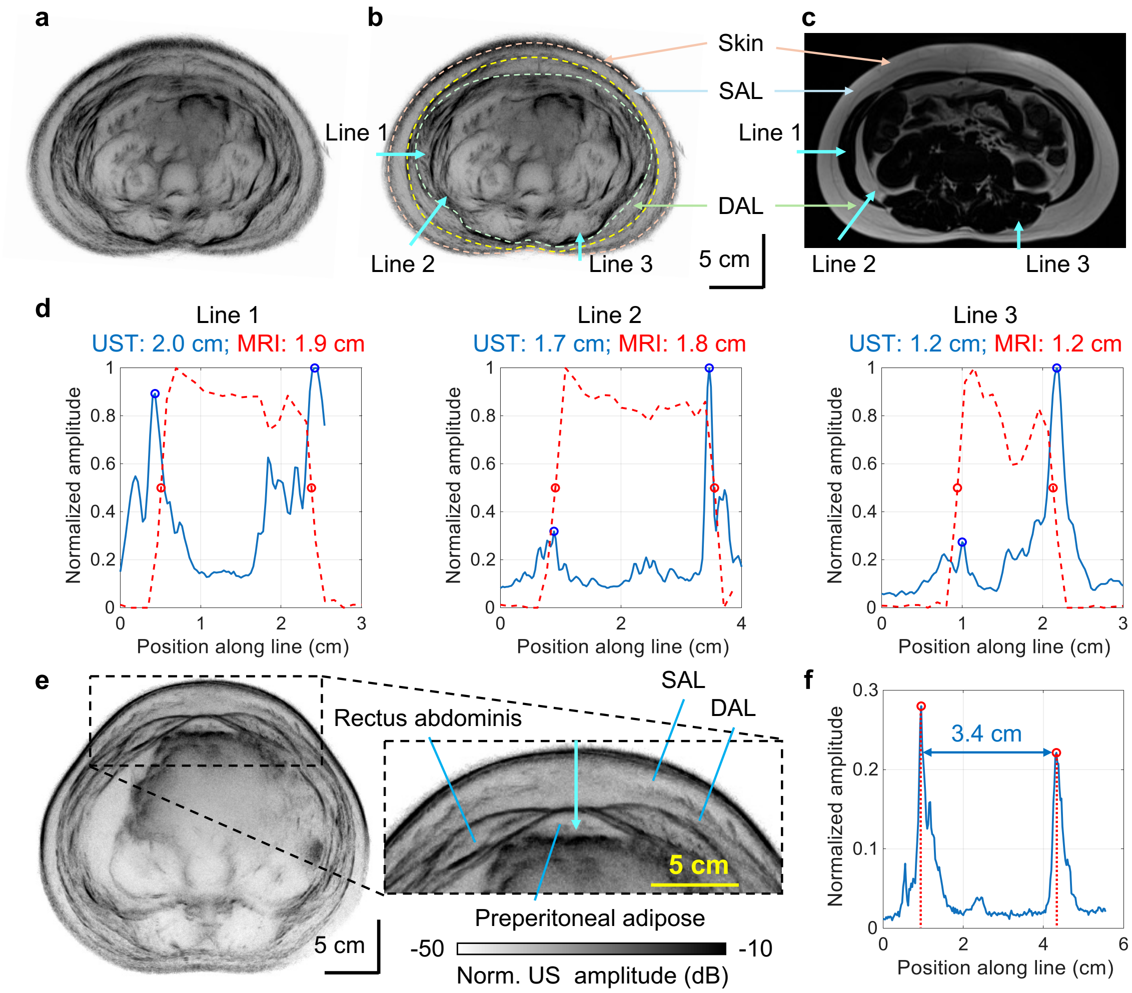

Figure 2.5. Abdominal adipose imaging in healthy volunteers. **a**, Unlabeled UST image 10 cm inferior to the starting position in a healthy female (Subject 1, BMI 18.8 $\mathrm{kg \cdot m^{-2}}$). **b**, Labeled UST image highlighting the differentiation of the skin, superficial adipose layer (SAL), and deep adipose layer (DAL). Cyan arrows show the lines used for the thickness estimation in **d**. **c**, T1-weighted fat-only MRI reconstruction of a corresponding region. **d**, Extracted line profiles used to estimate adipose thickness with UST (blue) and MRI (red). Circles show the estimated adipose boundaries. **e**, Abdominal UST of a healthy male (Subject 3, BMI = 25.1 $\mathrm{kg \cdot m^{-2}}$). **f**, Extracted UST line profile.

Biopsy needle localization

Next, we demonstrate UST-guided biopsy needle localization. In clinical practice, tissue samples from suspected cancerous regions are collected via needle biopsy, typically guided by ultrasound or X-ray CT imaging [48]. However, probe-based ultrasound localization is generally only used for superficial targets like in the breast, and it requires that the needle is approximately orthogonal to the imaging probe to provide sufficient backscatter to the probe. While manufacturers have developed treatments like scoring or bubble-filled polymer coatings to generate more isotropic scattering and improve the ultrasound visibility [49], these approaches can increase the insertional friction of the needle [50]. Moreover, probe-based localization requires the operator to simultaneously manipulate both the probe and needle, which requires substantial training [51] and becomes particularly challenging in complex tissue regions. CT needle guidance, while providing whole-body localization, involves a cumbersome workflow requiring multiple positioning cycles. Each adjustment requires the clinical team to exit and re-enter the scanning room, taking several minutes to complete. This interrupted workflow, combined with a concerning radiation exposure (approximately 10 mSv [52]), highlights the need for alternative guidance approaches.

Our approach uses a commercial 16-gauge core biopsy needle consisting of a solid stainless-steel core (1.5 mm diameter) that translates within a hollow sleeve. We found that ultrasound signals can be coupled into the unmodified needle using an ultrasonic transducer interfaced with the plastic handle. These signals propagate along the needle as an acoustic waveguide, and they are scattered nearly isotropically at the needle tip (Figure 2.6a). To enhance SNR, we employ the same chirp signal used in UST imaging. The scattered signals from the tip are detected with our acoustic array and are cross-correlated with the water chirp response. The propagation time along the needle is calibrated for and remains constant. We expect the dominantly excited mode to be longitudinal with approximately constant phase velocity over our frequency range (Figure 2.17).

The needle tip location is determined using one-way delay-and-sum beamforming, accounting for the propagation time along the length of the needle. The needle's image response (Figure 2.6b) demonstrates a full width at half maximum (FWHM) of ~0.7 mm. This approach enables 30-frame-per-second needle localization over a human-scale FOV. Example video frames (Figure 2.6c and d) show the needle response overlaid on a UST reflectivity image of an agarose phantom supported by a steel post. We normalize the needle response images by the same expected maximum value across all video frames. The needle's center response is automatically determined based on the 5th-order moment of the needle image. The full video is given in Supplementary Video 2.2. As seen, the acoustic image quickly and accurately tracks the location of the needle tip with respect to the phantom, even when moving rapidly or inserted into the tissue. To validate this approach in more realistic conditions, we used layered *ex vivo* porcine tissue (consisting of skin, adipose, and muscle) as an anatomical phantom. With the needle oriented approximately horizontally, this approach tracks its position during movement around and into the tissue (Figure 2.6e and f). Supplementary Video 2.2 demonstrates continuous localization of the needle tip throughout the insertion path.

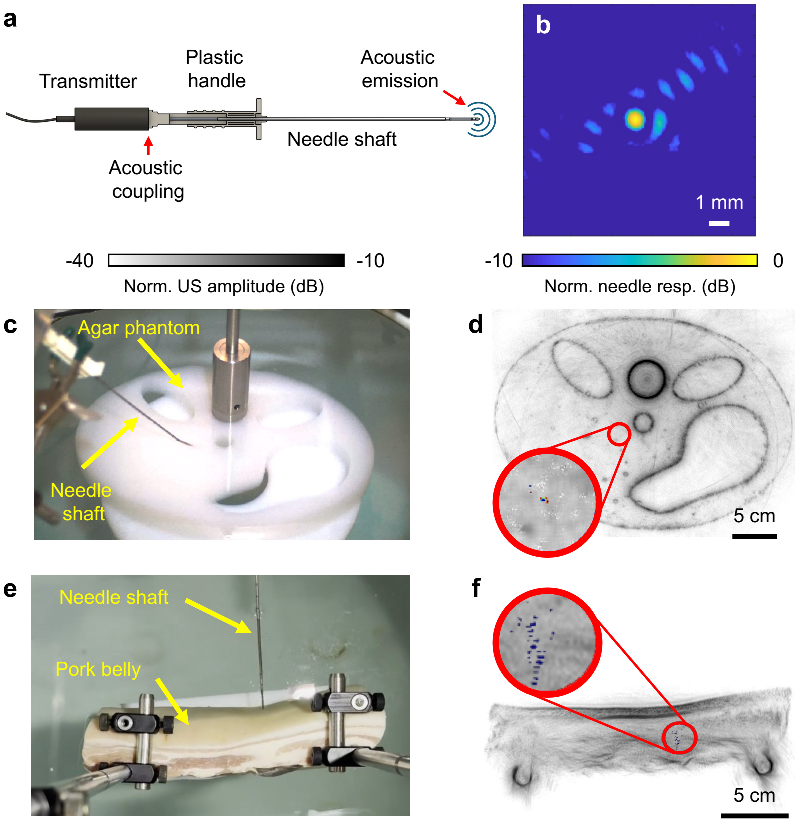

Figure 2.6. UST-guided biopsy needle localization. **a**, Schematic of the needle configuration. **b**, Acoustic response of the needle tip in water. **c**, Photograph showing the needle inserted into an agar phantom. **d**, Corresponding reconstructed frame overlaid on the reflection-mode UST image, with the red circle marking the automatically detected needle tip as the centroid of the acoustic response. **e**, Needle insertion into *ex vivo* pork belly tissue. **f**, Reconstructed frame overlaid on the reflection-mode UST image. Full video sequences are provided in Supplementary Video 2.2.

Discussion

We developed a system for whole cross-sectional human ultrasound imaging that advances beyond conventional probe-based ultrasonography in several key ways. Our approach captures complete body cross-sections while simultaneously providing three contrast mechanisms: reflectivity, speed of sound, and attenuation coefficient. Conventional short pulses would yield substantially reduced signal after penetrating the entire human body. To improve the signal-to-noise ratio, we employ chirped pulses in conjunction with matched filtering, enabling us to achieve higher-quality images. Chirped signals deliver more ultrasound energy while adhering to safety standards. Unlike clinical ultrasonography, which requires extensive operator training to visualize regions of interest, our approach could be largely automated since it requires minimal subject positioning. These advantages could be particularly attractive for applications requiring frequent imaging, and they could help reduce costs compared to other modalities.

Cross-sectional UST offers several potential clinical applications that warrant further study. This technique could enable screening of organs or tissue for indications of inflammation or disease [53]. For instance, liver cirrhosis may be visualized and tracked over time. Aortic aneurysms may also be visualized with UST in patients who are often asymptomatic. The quantitative measurements of speed of sound and attenuation coefficient could serve as diagnostic tools, for instance, to assess changes due to non-alcoholic fatty liver disease [53]. Additionally, our speed of sound maps could enhance acoustic focusing in therapeutic applications such as shockwave lithotripsy for kidney or gallbladder stones. Pancreas screening represents an important potential application of our technique, as no dedicated screening tool currently exists for this purpose.

Compared with other emerging techniques, such as low-field MRI [40], whole cross-sectional UST is faster (~10 seconds per 2D slice) with comparable or finer resolution (~1 mm), and it does not require a shielded room or a magnet-compatible environment. Further, it is more portable, more open, and less noisy than MRI. Due to its magnet-free operation, it can be used for subjects with implants that are incompatible with MRI. Together, these features make cross-sectional ultrasound tomography a potential practical tool for clinical needs currently unmet by other modalities. Although our system’s resolution does not match clinical CT or MRI, it offers unique advantages for longitudinal monitoring by enabling frequent scans without ionizing radiation exposure, large-magnet hazards, or lengthy scanning times. The system's efficiency in both cost and time could make it practical to track changes over weeks or months, especially for conditions where broad structural changes are most relevant, such as organ size variation or adipose redistribution.

The cost of UST patient care per visit is substantially lower compared to standard MRI, and the shorter visits also provide greater convenience for patients. We provide a comparison of cross-sectional UST with other clinical modalities in Table 2.1.

Our large FOV enables adipose assessment around the entire body. Unlike calipers or probe-based ultrasound, this approach visualizes subcutaneous and preperitoneal adipose around the entire periphery without mechanical deformation. This could be an appealing tool for liposuction planning and evaluation, weight loss monitoring [54], or pharmaceutical trials for anti-obesity drugs, where MRI and CT are prohibitively costly or harmful. Improved image quality or contrast may further enable the evaluation of visceral adipose regions. Muscle regions are also observed in our images (e.g., abdominal and leg muscles), which may be useful for guiding athletic training. A key advantage of our system is the intuitive nature of the cross-sectional images, which may reduce the amount of trained analysis required compared to conventional ultrasound. While interpretation is currently aided by clinical collaborators, future development of automated analysis pipelines could further enhance usability. In particular, AI-based segmentation and organ labeling methods, like those developed for MRI or CT [55], could provide guidance and annotation for non-expert users. Such advances could facilitate longitudinal screening and broaden the scalability of this technology for use in diverse clinical settings.

Cross-sectional UST shows promise in image-guided needle biopsy, where X-ray imaging is conventionally used. Our human-width FOV enables biopsy needle localization relative to internal features without ionizing radiation. Unlike CT guidance, which requires iterative needle positioning and imaging, UST provides real-time feedback during insertion. This technique could also be used for localization during minimally invasive robotic surgery [56], where the needle or tool tracked relative to internal features is particularly valuable during procedures that deform tissues.

Our current 10-second slice acquisition time enables imaging within a single breath hold. Two primary factors limit shorter acquisitions: the mechanical scanning rate of the transmitter and the data acquisition transfer rate, which depends on the repetition rate and acquisition length. We could achieve faster scanning using a slip ring for electrical connection to the transmitter and a more powerful driving motor. Given the ~1 ms roundtrip acoustic propagation time within the immersion tank, the repetition rate could potentially increase from our current device limit of 180 Hz to ~1 kHz. While an acoustic array could also be used to transmit and receive signals, this may compromise sensitivity due to electrical switching and reduced chirp signal length and quality. Water immersion could be eliminated through several alternatives: inflatable water bags like those used in shockwave lithotripsy [57], gel or liquid standoff pads [58], or with skin-coupled conformal acoustic arrays [59]. However, water immersion may be practical for specific applications like assessing adipose distribution. For example, fitness or wellness centers could conveniently integrate immersion-based scanning where users already swim or bathe. These users might value periodic scans to track changes in adipose and muscle thickness, similar to how dual-energy X-ray absorptiometry is used to monitor body composition [60].

In the future, we also plan to enhance this system with additional laser-induced photoacoustic and microwave/RF-induced thermoacoustic contrast. Using the same acoustic receivers, these images would be inherently co-registered with our UST images to overlay optical and microwave/RF absorption profiles. We also plan to improve our transmission-mode reconstruction quality using techniques such as full-wave inversion [61], enabling better localization of the speed of sound and attenuation coefficient variations. Additional acoustic elements could also reduce image acquisition time and provide 3D imaging capability.

Supplementary Information

Acquisition parameters

To enhance the signal-to-noise ratio (SNR) while limited by the mechanical index, a linear chirp signal versus time (t) is used with a time-varying frequency $f(t) = f_r t + f_0$, where $f_r = (f_1 - f_0)/T$ is the linear chirp rate, $f_0 = 0.3$ MHz is the lower frequency, $f_1 = 2.0$ MHz is the upper frequency, and $T = 400$ μs is the chirp duration. The transmitted frequencies are limited by the bandwidths of the transmitter and receivers. We used a maximal pulse duration given our maximal acquisition time of 800 μs, allowing for recovery of the round-trip reflected signals over the entire FOV. The resulting transmitted chirp signal is

$$x(t) = \sin\left[2\pi\left(\frac{f_r}{2}t^2 + f_0 t\right)\right]. \tag{2.1}$$

Compared to a pulse with similar peak pressure, this results in an expected SNR gain of $\sim \sqrt{T \cdot B}$, where $B = f_1 - f_0$ is the acoustic bandwidth [62]. In addition to the target, we also perform a scan with only water in the imaging domain, resulting in recorded signals $x_{w,i}(t)$ for each receiver element i. This provides the response of each transducer to the chirp which is then cross-correlated with the target's chirp response $x_{c,i}(t)$. The pulse response for the target signals $\chi_{s,i}(t)$ is then recovered for each element i as:

$$\chi_{s,i}(t) = \frac{x_{w,i}(t) \star x_{c,i}(t)}{\max\left[x_{w,i}(t) \star x_{w,i}(t)\right]}, \tag{2.2}$$

where $\star$ denotes cross-correlation. We normalize by the maximum of the autocorrelation of $x_{w,i}(t)$ to account for sensitivity variation in the receiver elements. The transmitter operates with a pulse repetition rate of 180 Hz. With the gear rotation time of 10 seconds, this results in 1800 transmitted pulses over a full circular scan around the target.

Reflection-mode reconstruction algorithm

We employ a 2D delay-and-sum algorithm for reflection-mode ultrasound reconstruction. We first cross-correlate each channel's recorded signal with its direct transmission water-only response to obtain a pulse-like representation. We then band-pass filter the cross-correlated signals within 0.3 – 2.0 MHz and normalize them based on the water-only autocorrelation. We use the Hilbert transform to obtain complex representations of the signals, which are used for reconstruction. Then, for each transmitter position, we determine the time delay between the transmitter focal point and each pixel for a given background speed of sound. We mathematically correct for the angle-dependent focal point with the acoustic lens, as shown in Figure 2.16. Next, we calculate the delay time from each pixel to each receiver position. We use the 256 receiver channels on the side of the transmitter to limit reconstruction to back-scattered signals. For each transmitter position, complex pixel values are found from the sum of the cross-correlated received signals at the total round-trip delay time.

After forming the angle-stacked complex image for each transmitter position, we improve image quality with coherent-subset scaling. The transmitter positions are partitioned into overlapping subsets of $M = 80$ consecutive angles, advanced by $M/2$ so each new subset shares 50 % of its angles with the previous one. Within each subset, we apply a Hann angular apodisation, coherently sum the complex data, and take the magnitude to generate an envelope image for that subset. Finally, we incoherently average the envelopes from all subsets to produce a compounded amplitude image. This procedure preserves coherent information within each narrow angular window while suppressing speckle through incoherent averaging across windows, resulting in a cleaner, higher-contrast reflection image.

We implemented this algorithm using CUDA kernel called from MATLAB, computed using a NVIDIA GeForce RTX 3070 graphics processing unit (GPU). Reconstruction was performed over a 512 mm x 512 mm grid with 0.125 mm x 0.125 mm pixel size, consisting of 4096 x 4096 pixels. For each slice, the required computational time was approximately

12 minutes. We expect this could be greatly shortened with more capable GPUs. To visualize the images, we first used a 2D Wiener filter with a 4-pixel neighborhood size. We then normalized the images to their maximum amplitude and displayed them on a logarithmic scale. Background segmentation was done using an automated segmentation tool [63].

Reflection-mode image quality

We assessed our in-plane resolution using a thin (< 0.1 mm) metallic wire. The reconstructed image and axis profiles are given in Figure 2.7. We find an in-plane FWHM of approximately 0.9 mm. To determine our elevational resolution, we imaged a thin brass disc positioned such that its edges were at the center and outer boundary of our typical FOV. The height of the disc was scanned, and a UST image was obtained at 2.5 mm increments. An elevational FWHM of 15 mm and 25 mm was found for the center and edge of the FOV, respectively. Neither the transmitter nor the receivers are focused in the elevational direction, but their larger dimensions in this direction reduce their acceptance angles.

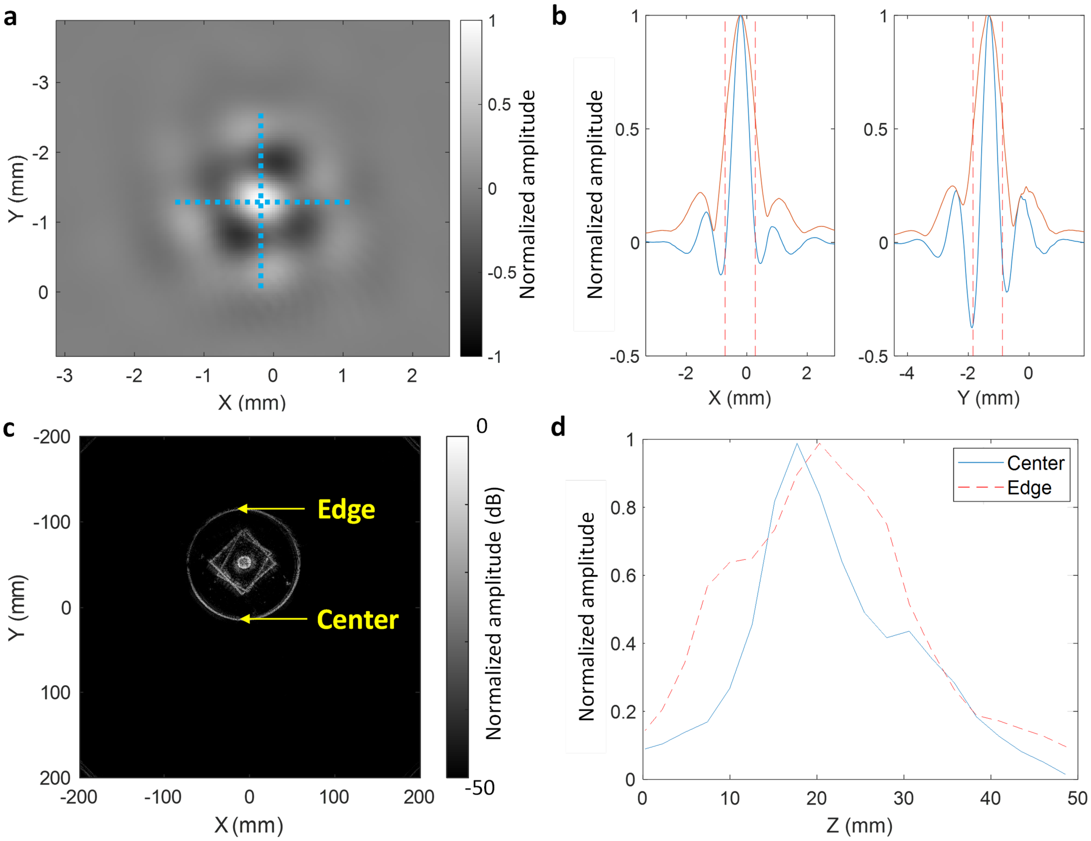

Figure 2.7. In-plane and elevational resolution assessment. **a**, Reconstructed reflectivity image of a thin wire. **b**, Profiles along the x and y axes: pixel amplitude (blue), the magnitude of its Hilbert transform (orange), and the full width at half maximum (FWHM, dashed vertical lines). **c**, Example reflectivity image of a brass disc used for elevational resolution assessment. **d**, Profiles of the center and edge responses at different z positions.

Human imaging protocol

Five volunteers (three females, two males) consented to be imaged using this system. This imaging procedure was approved by the Caltech Institutional Review Board (protocol IR21-1099). Before human imaging, we used a calibrated hydrophone (Onda HGL-0085) positioned immediately in front of the transmitter to evaluate the safety of our system. We used a mechanical index of less than 0.2 over the entire chirp bandwidth, whereas the limit from the U.S. Food and Drug Administration (FDA) is 1.9 [64]. We evaluated the spatial peak temporal average intensity (I_{SPTA}) as 24 mW/cm^2, whereas the FDA limit is 720 mW/cm^2. We calculated the thermal index from the empirical formula as listed in [65] to be 0.65, which is also much lower than the FDA limit of 6.0 for diagnostic ultrasound devices.

Prior to imaging, we filled the water immersion tank with warm (~30 °C) tap water using rubber tubing. We provided a private room for volunteers to change into a swimsuit and to dry using a towel and space heater after the imaging session. Volunteers entered the tank using an external ladder with handrails and anti-slip coatings (Figure A.4). After volunteers entered the water tank, we asked them to use their hands to wipe away air bubbles that may have accumulated on their abdomens. An emergency off button was accessible to the volunteers during scanning, shutting electrical power to all system devices. All electrical devices were powered through a ground-fault circuit interrupter in case of water exposure. The operators ensured volunteer comfort verbally and visually. The volunteers remained seated on an immersed stool during image acquisition with their shoulders resting on a backrest to reduce motion. We performed these human experiments in a dedicated imaging room. Written informed consent was obtained from participants in accordance with our IRB protocol. Volunteers were compensated $100.

Comparison to other modalities

We compare cross-sectional UST to other diagnostic modalities in Table 2.1. While the commercial cost of our approach is not yet known, we expect it to be low given the relatively small (< $100k) material and equipment cost we used to develop our system.

Table 2.1. Comparison of abdominal imaging modalities.

	X-ray CT	***MRI***	***Probe-based ultrasound***	***Cross-sectional UST***
Whole cross-section penetration (~35 cm)	Yes	Yes	No	Yes
Whole abdominal imaging time	Moderate (5 – 10 min.)	Very long (30 – 60 min.)	Moderate overall time despite very fast individual images (10 – 20 min.)	Moderate (5 – 10 min.)
Safety	Ionizing radiation (~5 – 15 mSv)	Strong magnetic fields, radiofrequency exposure	Safe	Safe
In-plane resolution	Very good (~0.5 – 1 mm)	Good (~1 – 2 mm)	Very good, scalable (~0.3 – 2 mm)	Good (~1 mm)
System cost	Moderate	Very high	Low	Low
Operational cost	Moderate (Maintenance, X-ray tubes)	Very high (Technicians, liquid helium)	Moderate (Trained operation)	Low (Water refilling, minimal operator training)

We compare cross-sectional UST to conventional methods of adipose assessment in Table 2.2. Note that calipers, probe-based ultrasound, and our approach estimate subcutaneous adipose (SA) thickness, whereas DXA estimates body composition in 2D projections.

Table 2.2. Comparison of adipose assessment modalities. DXA: dual-energy X-ray absorptiometry. SA: subcutaneous adipose.

	Calipers	***DXA***	***Probe-based ultrasound***	***Cross-sectional UST***
Measured property	Thickness of a pinched fold of skin and SA	Dual energy X-ray absorption	Acoustic backscatter	Acoustic backscatter
Estimated value	SA thickness	Fat content instead of thickness	SA thickness	SA thickness
Safety and comfort	Slight pinch on skin, procedural intimacy	Low ionizing radiation exposure (~1 – 10 μSv)*	Procedural intimacy	Water immersion
Assessed region	Individual superficial sites	Whole body in 2D projections	Individual sites	Whole abdomen and lower body
Operator dependence	High (Location selection, mechanical deformation)	Very low, but strong dependence on calibration	High (Location selection, mechanical deformation)	Low
System cost	Very low	Low	Low	Low
Operational cost	Moderate (Trained operation)	Low (Minimal operator training)	Moderate (Trained operation)	Low (Water refilling, minimal operator training)

*Despite the low ionizing radiation exposure, some patients may prefer to avoid any additional exposure. The recommended annual radiological exposure limit is 1 mSv [66].

We compare approaches for biopsy needle localization in Table 2.3.

Table 2.3. Comparison of modalities for biopsy needle localization.

	X-ray CT	***Probe-based ultrasound***	***Cross-sectional UST***
Feedback time	Iterative, long (~minutes)	Real-time	Real-time
Operational complexity	Minimal	High (Manipulating the probe and needle simultaneously)	Minimal
Safety	Ionizing radiation (~10 mSv)	Minimal	Minimal
Field of view	Whole cross-section	Local to the probe	Whole cross-section
Anatomical sites	Any organ	With ultrasound window	With ultrasound window

Additional human images

We imaged an adult female (Subject 1) in 1-cm increments from the ribcage toward the pelvis and at several regions in the thigh, shown in Figure 2.8.

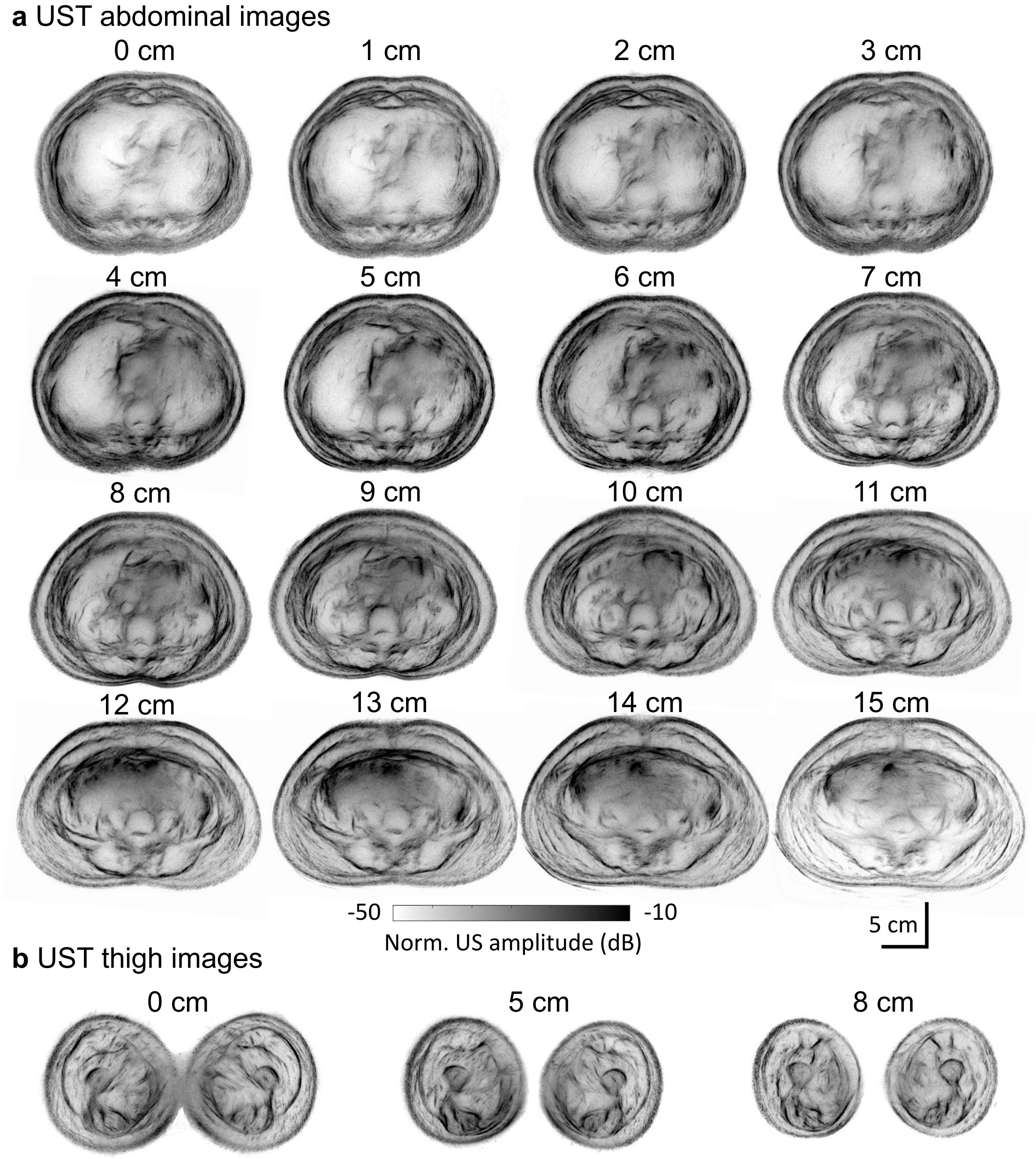

Figure 2.8. Each elevational scan of a female (Subject 1) from approximately the ribcage to the pelvis.

The estimated speed of sound for each slice is overlaid on the reflection-mode image in Figure 2.9. As expected, organs like the liver are found to have higher speed of sound than adipose regions (e.g., posterior regions in slice 12 – 15 cm).

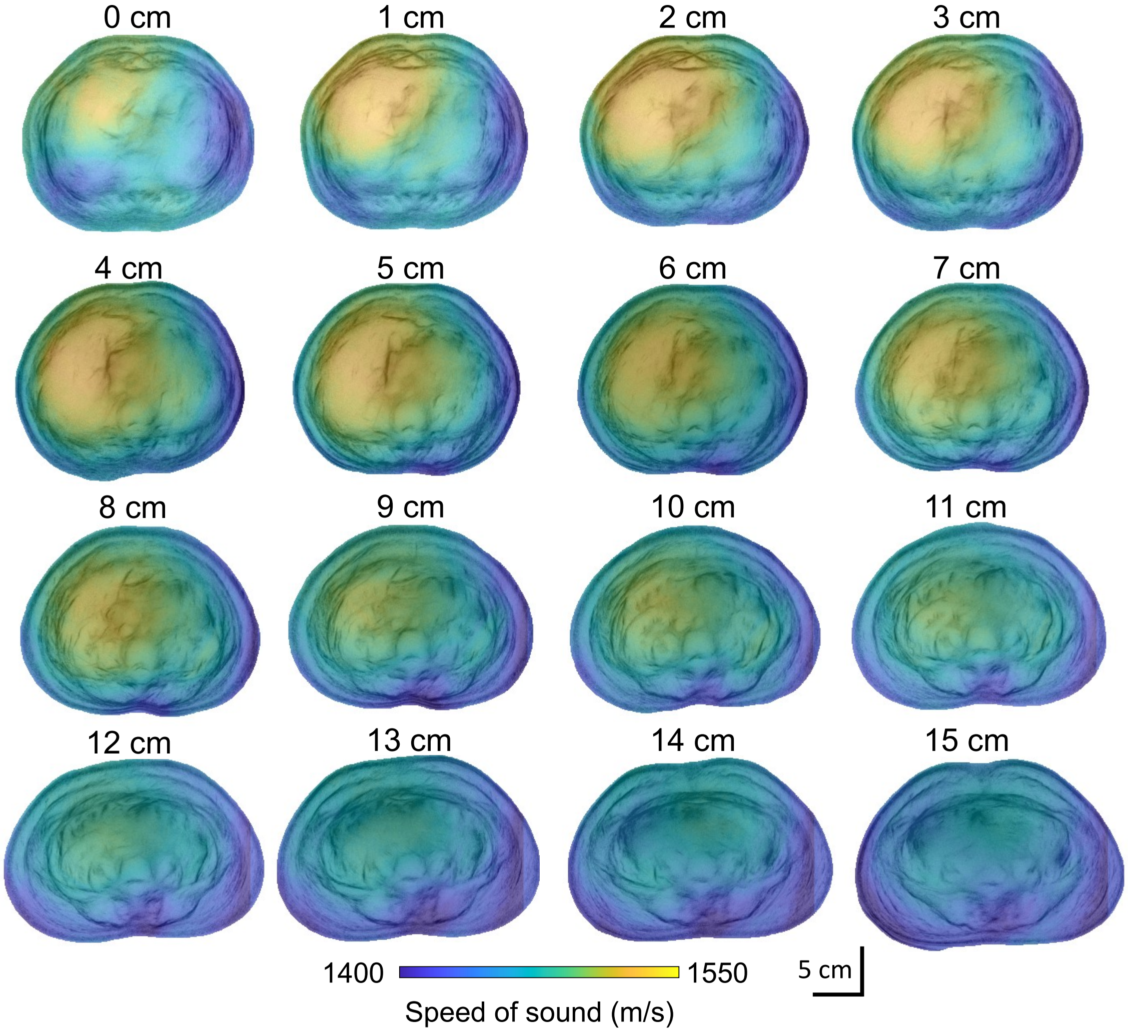

Figure 2.9. Reconstructed speed of sound for an adult female (Subject 1).

The estimated attenuation coefficient for each slice is overlaid on the reflection-mode image in Figure 2.10. Note that the upper slices have artificially high attenuation coefficient owing to acoustic occlusion from the inferior of the lungs and the ribs. In lower slices, adipose is found to have lower attenuation coefficient than the interior organs (e.g., intestines), which may contain air pockets.

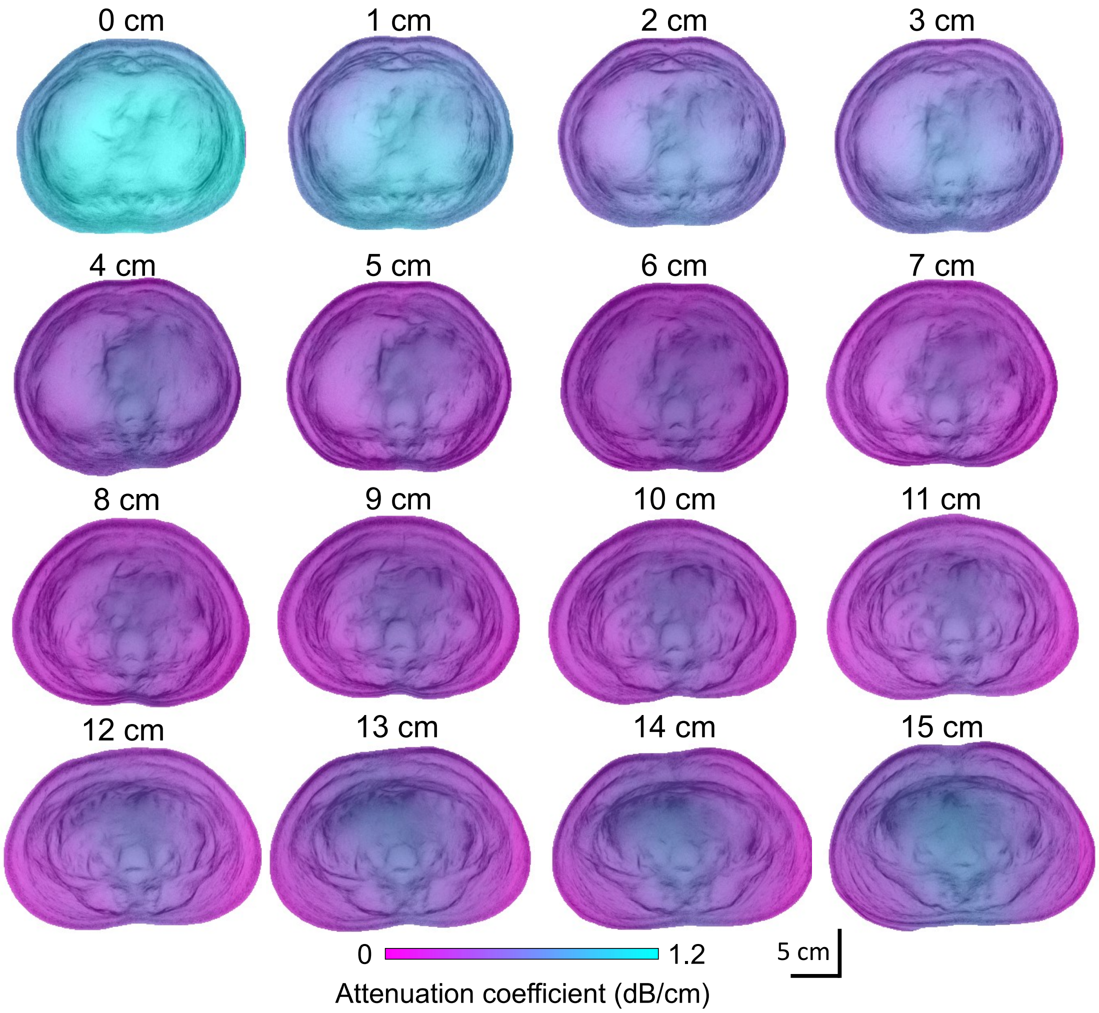

Figure 2.10. Reconstructed attenuation coefficient for an adult female (Subject 1).

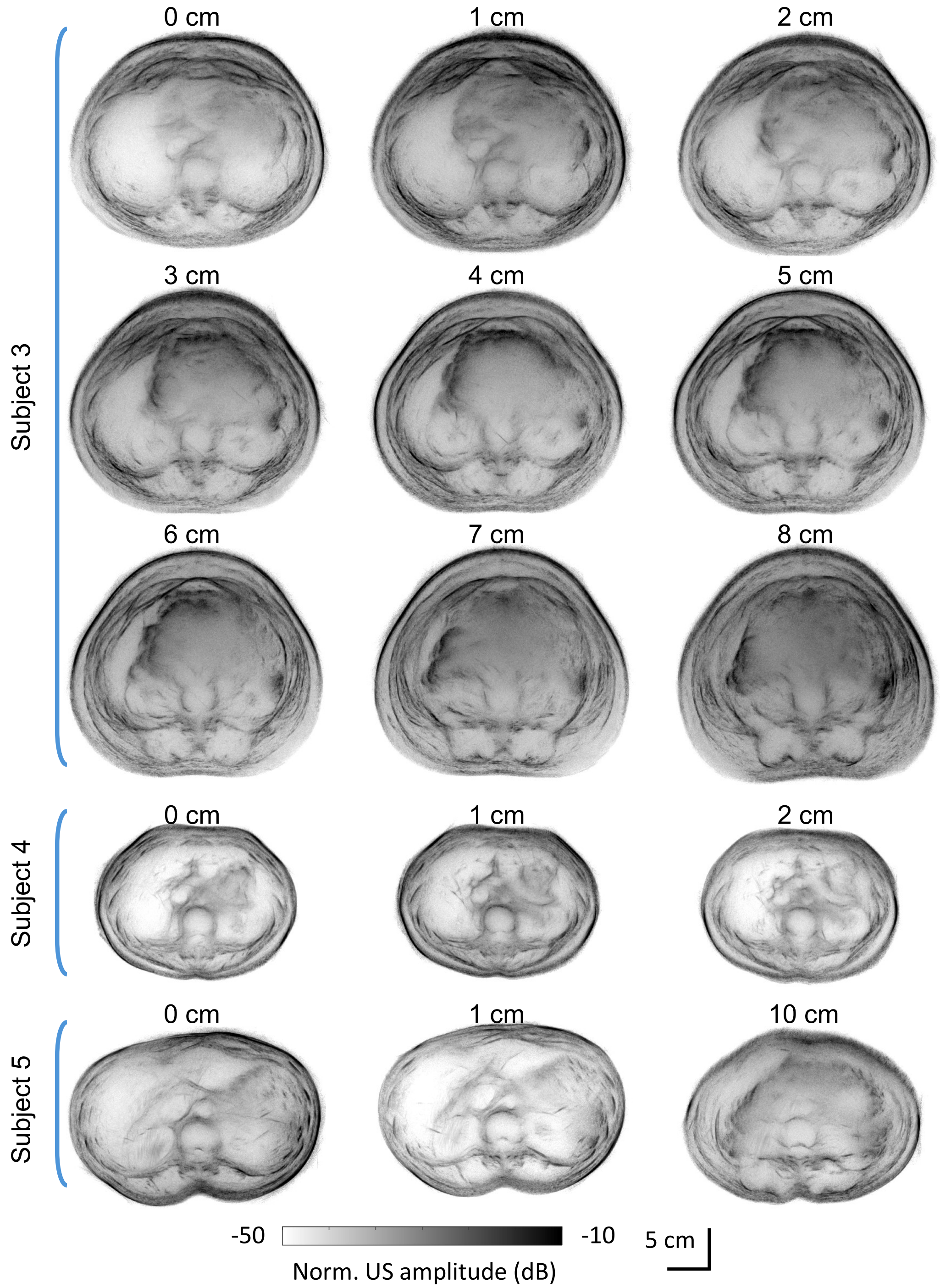

Figure 2.11. Example images for three additional subjects. Labeled positions denote the distance from the starting imaging plane. Subject 3 is a 27-year-old male. Subject 4 is a 20-year-old female. Subject 5 is a 29-year-old male.

Straight-ray transmission-mode reconstruction algorithm

Our data processing steps for transmission-mode imaging are shown in Figure 2.12. Starting from the recorded water-only and target signals, we first perform cross-correlation to obtain pulse-like representations of the transmitted signals. We then determine the arrival time of the water and target signals, and we determine the arrival time difference for each receiver and transmitter position pair. This is used for reconstruction of the speed of sound. Similarly, we also determine the amplitude ratio between the water and target signals, which is used for attenuation coefficient reconstruction.

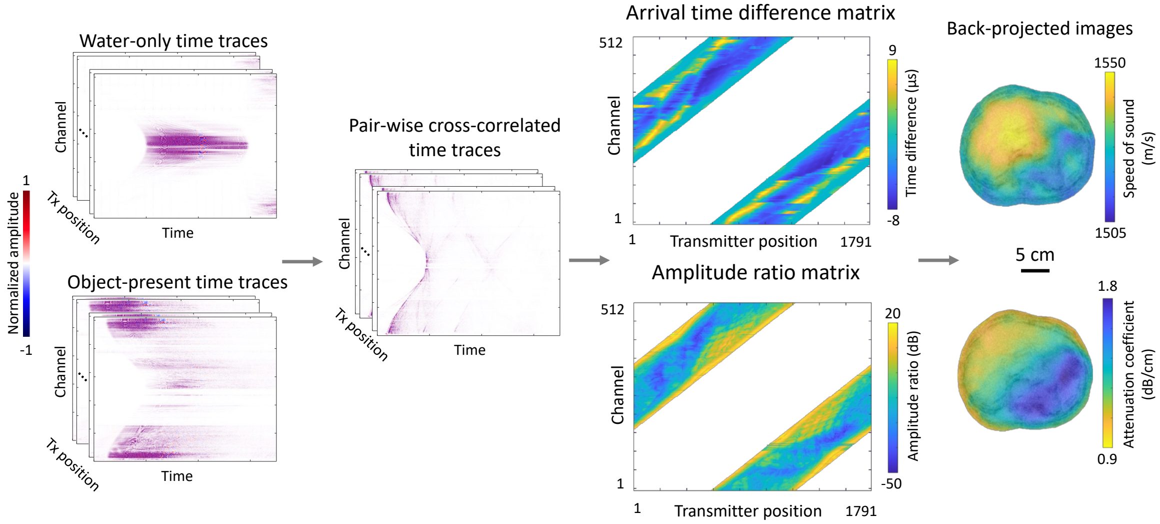

Figure 2.12. Signal processing flow for transmission-mode analysis.

We use the first-break method [67] to determine signal arrival time. For a given cross-correlated target signal $\chi_s(i)$ at discrete time samples i, an energy ratio er is defined for a window size N_e as:

$$\mathrm{er}(i) = \frac{\sum_{j=i}^{i+N_e} {\chi_s}^2(j)}{\sum_{j=i-N_e}^{i} {\chi_s}^2(j)}. \qquad (2.3)$$

We use a window N_e of 4 μs as a compromise between robustness and precision. The modified energy ratio (mer) is then calculated as:

$$\mathrm{mer}(i) = (|\chi_s(i)| \times \mathrm{er})^3. \tag{2.4}$$

The signal arrival time is determined from the maximum value of mer. As an example, the calculated transmission-mode arrival times through water and a human abdomen are shown in Figure 2.13.

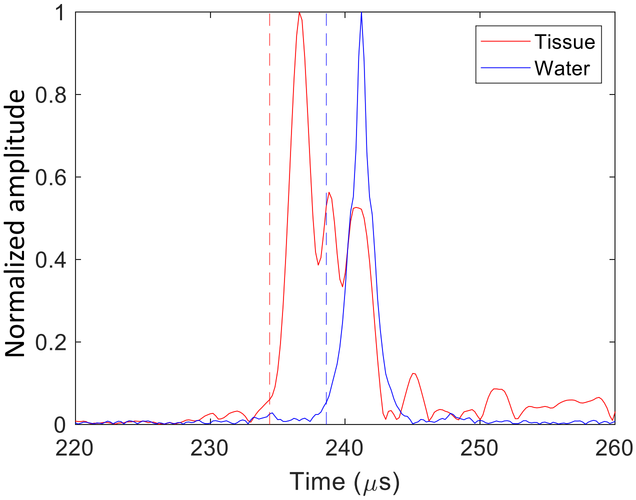

Figure 2.13. Example cross-correlated transmission signals for water-only and the human abdomen. The vertical dashed lines show the estimated arrival times using the first-break method.

We then perform reconstruction as follows. Along the straight ray L_i between the i^{th} transmitter-receiver pair, the total delay τ_i can be modeled as $\int_{L_i} \frac{dl}{c(\vec{r})} = \tau_i$, where $c(\vec{r})$ represents the location-dependent speed of sound. This equation can be discretized as $\sum_{j \in \{L_i\}} \Delta l_{ij} \cdot x_j = \tau_i$, where $x_j = \frac{1}{c_j}$ is the inverse of the speed of sound at the j^{th} pixel along ray L_i and Δl_{ij} represents the length of ray L_i crossing the j^{th} pixel. The linear equation can be arranged into the matrix form $AX = T$, where X and T are the vectorized x_j and τ_i.

One technical issue with solving the linear equation is with the memory required for matrix A which is of the size $(N_t \cdot N_r) \times (N_x \cdot N_y)$ ($>10^{11}$ in our implementation). Rather than saving and inverting the matrix directly, we take advantage of the fact that $A' = A^T A$ is close to diagonal (as neighboring rays go through neighboring pixels), and therefore $X' \approx A^T A X$ can be estimated as a vector with elements $x'_j \approx A'_{jj} x_j = \left(\sum_i \Delta l_{ij}^2\right) \cdot x_j$. The right-hand side of the equation is then converted to $B = A^T T$, with elements $b_j = \sum_i \tau_i \, \Delta l_{ij}$. Thereby, simple element-wise division of B by $\sum_i \Delta l_{ij}^2$ solves for X.

The attenuation coefficient map can be rearranged as $\int_{L_i} \mu_a(\vec{r}) dl = a_i \Rightarrow \sum_{j \in \{L_i\}} \Delta l_{ij} \cdot \mu_{a\,j} = a_i$ and solved concurrently. We also tested methods such as global path tracing [68], an adapted algorithm of dynamic time warping used in seismology field, to enforce the smoothness prior between neighboring frames, and matched filtering which requires accurate knowledge of the transmitted waveform. In practice, we found these methods to perform similarly given the SNR of the time traces collected.

Transmission-mode reconstruction accuracy

To assess the accuracy of our speed of sound profiles, we imaged ethanol-water mixtures with speed of sound ranging from approximately 1510 to 1610 m/s. Note that the speed of sound increases with ethanol content until ~50%, but decreases at higher content [69]. The reference speed of sound was determined using a single-element transducer immersed in the mixture and by varying the distance to an acoustic reflector to record the time-of-flight using an ultrasonic pulser (Olympus 5072PR). Measurements were recorded over 21 distances at 1 mm intervals. The speed of sound was then calculated as $v = \Delta d / 2\Delta t$, where Δd is the difference in position, and Δt is the difference in arrival time. The arrival time is determined using the first-break approach. Table 2.4 shows the mean and standard error of the speed of sound estimations for each mixture.

We then held the five mixtures in thin membranes with ~3 cm diameter and imaged together in the same session. For transmission-mode reconstruction, we used both the unmasked and masked approaches, where the masked method uses the reflection-mode image to segment each mixture during reconstruction. The resulting speed of sound estimations are given in Table 2.4. We find typical errors of less than 1%, but a maximum error of 1.52% and 2.84% for the unmasked and masked approaches, respectively.

Table 2.4. Estimated speed of sound in m/s for ethanol-water mixtures. Reference values were determined using a single-element transducer at varying distances in the mixtures. Percent error from the reconstructed values is shown in parentheses.

Method	**Ethanol content**				
	5%	**10%**	**20%**	**50%**	**60%**
Reference	1508.6	1532.4	1578.9	1609.5	1531.4
(Standard error)	(0.18)	(0.24)	(0.26)	(0.50)	(0.18)
Unmasked	1511.0	1524.5	1580.2	1604.2	1508.1
(% error)	(0.15%)	(-0.52%)	(0.08%)	(-0.33%)	(-1.52%)
Masked	1509.39	1542.04	1578.83	1563.77	1520.03
(% error)	(0.04%)	(0.63%)	(0.00%)	(-2.84%)	(-0.74%)

Since we obtain distinct organ boundaries from the reflection-mode images, we can also segment organ contours to constrain the transmission-mode reconstruction for bulk organ regions. From our human images, we then compared our estimates of several tissues' speed of sound (from Subject 2) with literature values [37], as shown in Figure 2.14. Our estimates for the liver and stomach speed of sound match closely with literature values, but there is less agreement for other organs like the spleen. This is likely because these regions are smaller and therefore undergo less temporal shift from their speed of sound variations.

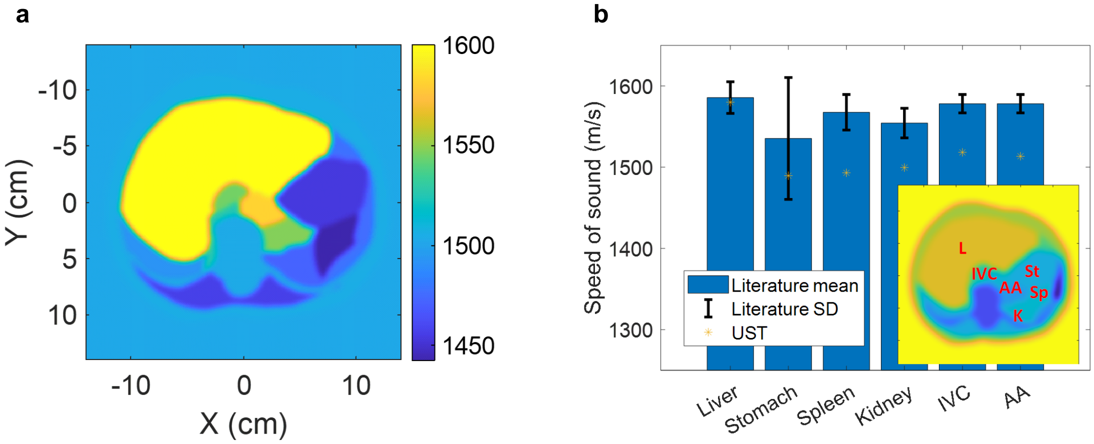

Figure 2.14. Comparison of literature [37] and UST estimations of tissue speed of sound. **a**, Reconstructed speed of sound using segmented tissue regions. **b**, Comparison to literature values. SD: standard deviation. L: liver. St: stomach. Sp: spleen. K: kidney. IVC: inferior vena cava. AA: abdominal aorta. The inset shows the segmented tissue regions used for speed of sound reconstruction.

Since liver health assessment is a potential application of cross-sectional UST, we compared our estimated properties with reported values in various diseased states. Figure 2.15 shows the reported speed of sound [70] and attenuation coefficient [71] of the healthy and diseased liver. These values are shown alongside our estimations (from the subject in Fig. 2) across six image slices spaced by 1 cm vertically. As expected, our estimated values fall within the expected range for healthy subjects.

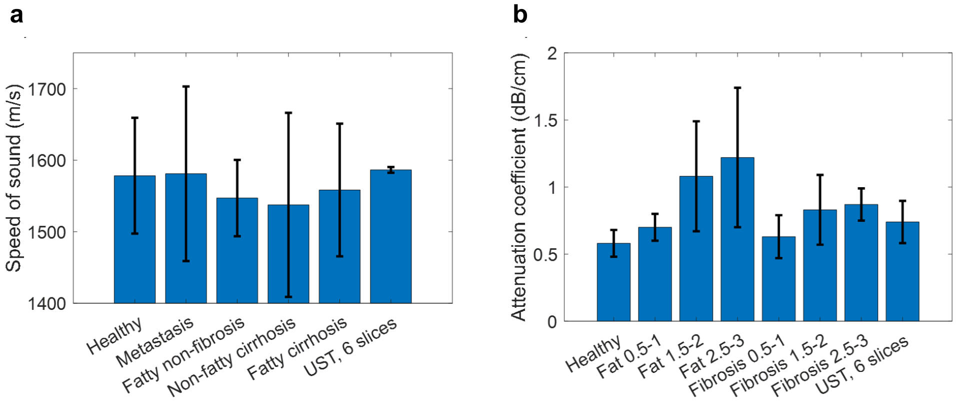

Figure 2.15. Comparison of UST transmission-mode estimations for a healthy subject's liver acoustic properties. **a**, Literature speed of sound values for the liver under various diseased conditions [70]. **b**, Literature attenuation coefficient values for the liver at

varying pathological stages of disease [71]. Error bars show the standard deviation of literature values and UST estimations across six images.

Transmitter lens correction

For manufacturing simplicity, we used a cylindrical TPX lens to diverge the transmitter beam, shown in Figure 2.16a. If uncorrected, this geometry causes cylindrical aberration where different emission angles correspond to varying effective focal lengths. We correct for this aberration during reconstruction. For each transmitter position, we determine the angle to each pixel and assign an appropriate focal length. We consider a plane wave emitted from the flat transducer surface as shown in Figure 2.16b. Wavefronts emerging at position x along the transducer surface arrive at the lens interface at depth $y = \sqrt{r_{\text{lens}}^2 - x^2}$. The angle normal to the lens surface at this position is:

$$\theta_{\text{norm}} = \tan^{-1}(x/y). \tag{2.5}$$

The wavefront refracts at an angle relative to the normal angle as:

$$\theta_{\text{ref}} = \sin^{-1}\left[\sin(\theta_{\text{norm}})\frac{c_{\text{water}}}{c_{\text{lens}}}\right], \tag{2.6}$$

where $c_{\text{water}} \sim 1500$ m/s and $c_{\text{lens}} \sim 2090$ m/s are the water and TPX lens speed of sound, respectively. The angle into the imaging plane is therefore $\theta_{\text{pix}} = \theta_{\text{norm}} - \theta_{\text{ref}}$. This line intersects with the centerline of the transducer at distance f behind the emitting surface:

$$f = \frac{x}{\tan \theta_{\text{pix}}} - y. \tag{2.7}$$

During reconstruction, from a given θ_{pix}, we can therefore calculate the appropriate focal length f. Example calculated values are shown in Figure 2.16c. This is incorporated in our GPU-based reconstruction.

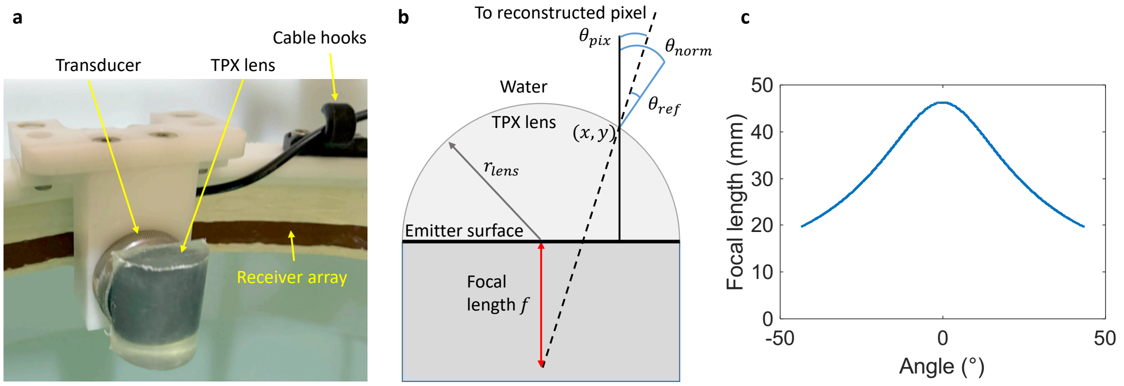

Figure 2.16. Determining the effective focal length for various pixel angles using a cylindrical TPX lens on the acoustic transmitter. **a**, Photograph of TPX lens mounted on the transmitting transducer. **b**, Diagram of TPX lens and transmitter surface. **c**, Calculated focal length for varying angles to reconstructed pixels (θ_{pix}).

Biopsy needle acoustic modes

The biopsy needle acts as an acoustic waveguide where different modes are supported depending on the frequency and form of excitation. These modes can be longitudinal, torsional, or flexural. We expect the dominant mode to be the longitudinal L(0,1) mode which, fortunately, has approximately uniform phase velocity and low attenuation over our frequency range for this needle diameter (~1.5 mm), as shown in Figure 2.17a and b [72]. The phase velocity is close to the bulk longitudinal velocity of stainless steel (~5790 m/s). During reconstruction, we therefore consider a constant propagation delay down the needle length of ~50 μs.

An example received waveform spectrogram is shown in Figure 2.17c, showing that the linear chirp is maintained after propagation along the needle and emission at the tip. There is some reverberation after the dominant chirp signal due to other acoustic modes. A weak second-order chirp (at twice the dominant frequencies) is also visible due to nonlinearities in the power amplifier.

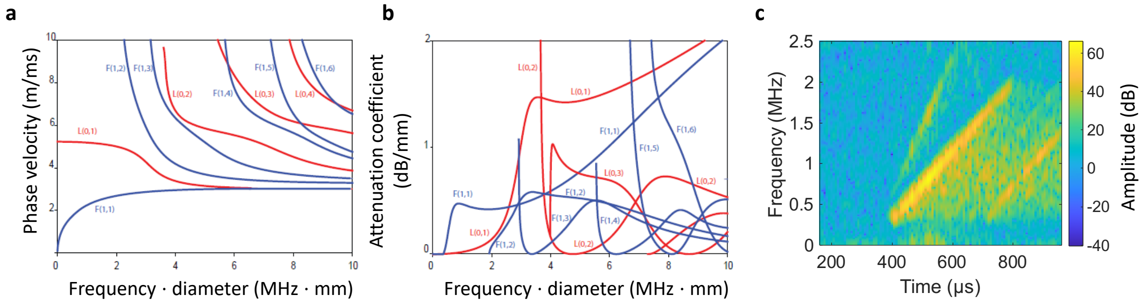

Figure 2.17. Expected acoustic modes in an unmodified biopsy needle. **a** and **b**, Phase velocity and attenuation coefficient, respectively, for acoustic modes supported by a stainless steel rod immersed in water, adapted with permission from [72]. **c**, Example waveform received from the scattered emission from the biopsy needle.

Adipose thickness estimation

To validate our adipose thickness estimation method, we constructed a phantom consisting of a lard layer over a 4% agar core (Figure 2.18a and b). A plastic ribbon of 0.25 mm thickness defines the material boundaries. Ridges in plastic plates on the top and bottom of the phantom align the ribbon in precise shapes. Heated liquid agar was first poured in the center mold and allowed to cure at room temperature for two hours. We then melted pork lard and poured it into the outer mold. The phantom then cooled at room temperature for one hour. The lard thickness on two sides of the phantom is 1.0 and 2.0 cm, and the phantom is 7.5 cm tall.

We then imaged the phantom in the UST system (Figure 2.18d). To estimate the lard layer thickness, we first extract line profiles from the reflection-mode images and plot the image amplitude A versus position s along the line. Figure 2.18e and f show the normalized image amplitude along lines on two sides of the phantom. We estimate the layer thickness by determining the two dominant amplitude peaks (at positions $s_{0,1}$ and $s_{0,2}$) and calculating the distance between them.

We estimate the adipose layer thickness uncertainty σ_t as

$$\sigma_t = \sqrt{\frac{\sigma_{w1}^2}{\mathrm{CNR}_1} + \frac{\sigma_{w2}^2}{\mathrm{CNR}_2}}, \tag{2.8}$$

where σ_{w1} and σ_{w2} are the root mean square widths of the amplitude peaks, and CNR_1 and CNR_2 are their amplitude-based contrast-to-noise ratio (CNR). Since the peaks do not necessarily follow Gaussian shapes, we calculate the widths for each peak i as:

$$\sigma_{w,i} = \sqrt{\int_{s_{0,i}-s_{win}}^{s_{0,i}+s_{win}} \left(s - s_{0,i}\right)^2 \cdot A(s)ds \Big/ \int_{s_{0,i}-s_{win}}^{s_{0,i}+s_{win}} A(s)ds}. \tag{2.9}$$

We consider a window s_{win} around each side of the peaks (chosen as 5 mm) to capture the dominant interface response without extending to neighboring features. We calculate the CNR in a linear scale as

$$\mathrm{CNR}_i = \frac{A\left(s_{0,i}\right) - \overline{A_{out}}}{\mathrm{std}(A_{out})}. \tag{2.10}$$

Here, A_{out} is a 4 cm portion of the line profile outside the target used to characterize the background.

The estimated thicknesses of 1.05 $\pm$ 0.02 cm and 2.02 $\pm$ 0.05 cm agree closely with the true values of 1.00 cm and 2.00 cm, respectively. A ~3% overestimation in thickness is expected due to the slower speed of sound in lard (~1440 m/s) than room temperature water (~1483 m/s), which we do not correct for here. We used the same methodology to estimate the adipose thickness in our human images in Fig. 4.

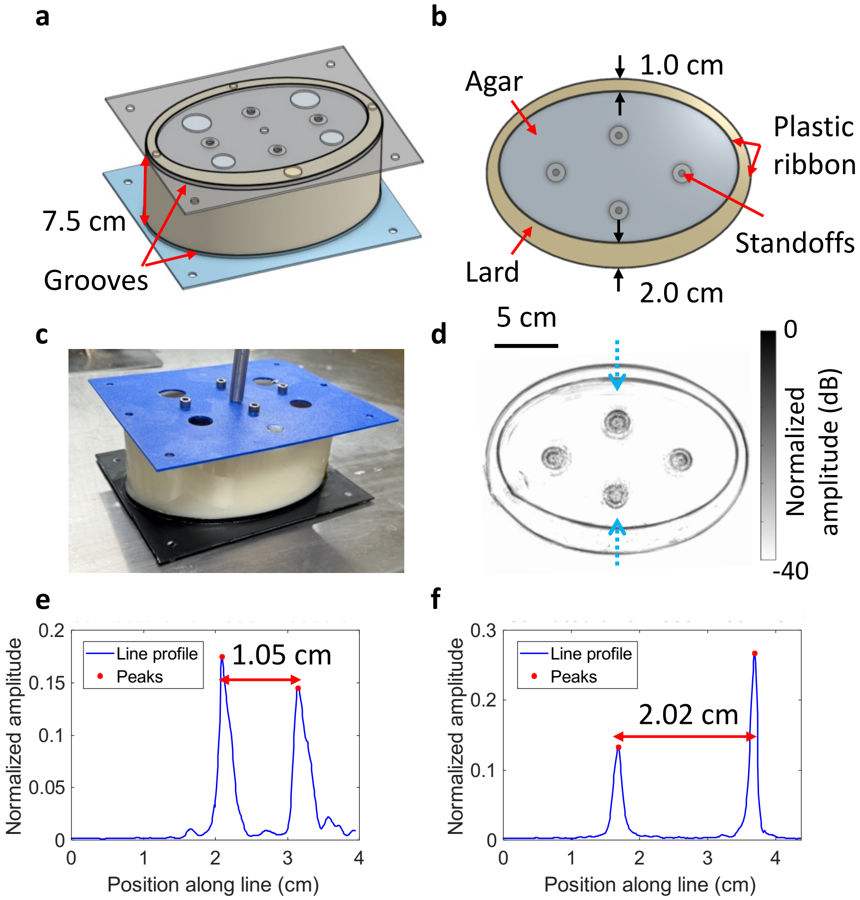

Figure 2.18. Estimating adipose thickness in a phantom. **a**, Phantom design. A plastic ribbon holds a layer of pork lard around an agar core. The lard thickness on two sides is to be 1.0 cm and 2.0 cm. **b**, Reflection-mode UST image of the adipose phantom. Dashed lines show the lines used for extracting the lard layer thickness, with the arrow showing the direction of the line profile. Panels **c** and **d** show the normalized amplitude (in linear scale) extracted from the drawn lines in the UST image on the 1.0 cm and 2.0 cm lard thickness sides of the phantom, respectively.

We show further examples of compared adipose thicknesses between UST and MRI in Figure 2.19. For various image planes and line profiles, we observe a maximum difference between the two modalities of 3 mm. We chose regions on the posterior of the body since they are expected to deform less between MRI (subject in the supine position) and UST (subject seated).

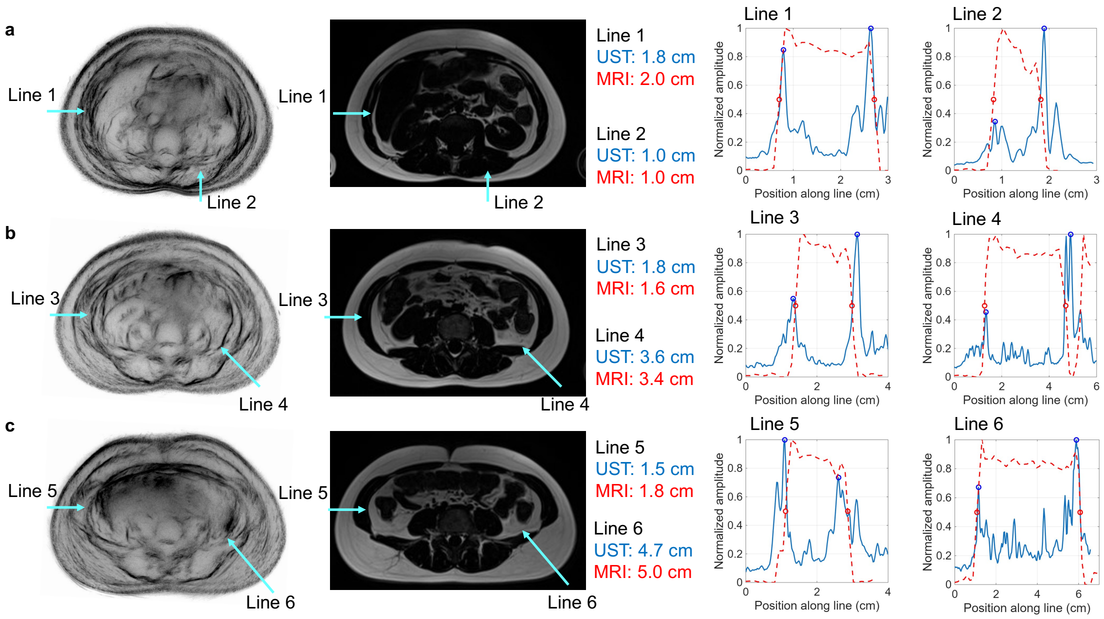

Figure 2.19. Additional adipose comparisons between UST and MRI. Each row shows a separate imaging plane. Left: UST image. Middle: Fat-weighted 3T MRI image. Right: line profiles for UST and MRI with estimated adipose thicknesses. **a** - **c** show images at 8 cm, 11 cm, and 14 cm inferior to the starting imaging plane.

We then imaged a healthy subject (25-year-old female) to compare our UST SA thickness estimates with caliper measurements. As shown in Figure 2.20a, our adipose thickness estimation from the extracted line profile (1.59 ± 0.06 cm) agrees reasonably with the caliper measurement of 1.3 cm used at the same location. We then imaged a 27-year-old male volunteer with greater SA thickness (Figure 2.20c). While internal features are less well visualized due to the greater tissue depth and potential increased air content in organs, the adipose layers remain clearly visible. To assess caliper accuracy in individuals with greater SA thickness, we obtained a UST image during caliper measurement. Figure 2.20e demonstrates that calipers underestimate the total SA thickness [73], measuring 1.9 cm compared to approximately 3.2 cm in the UST image.

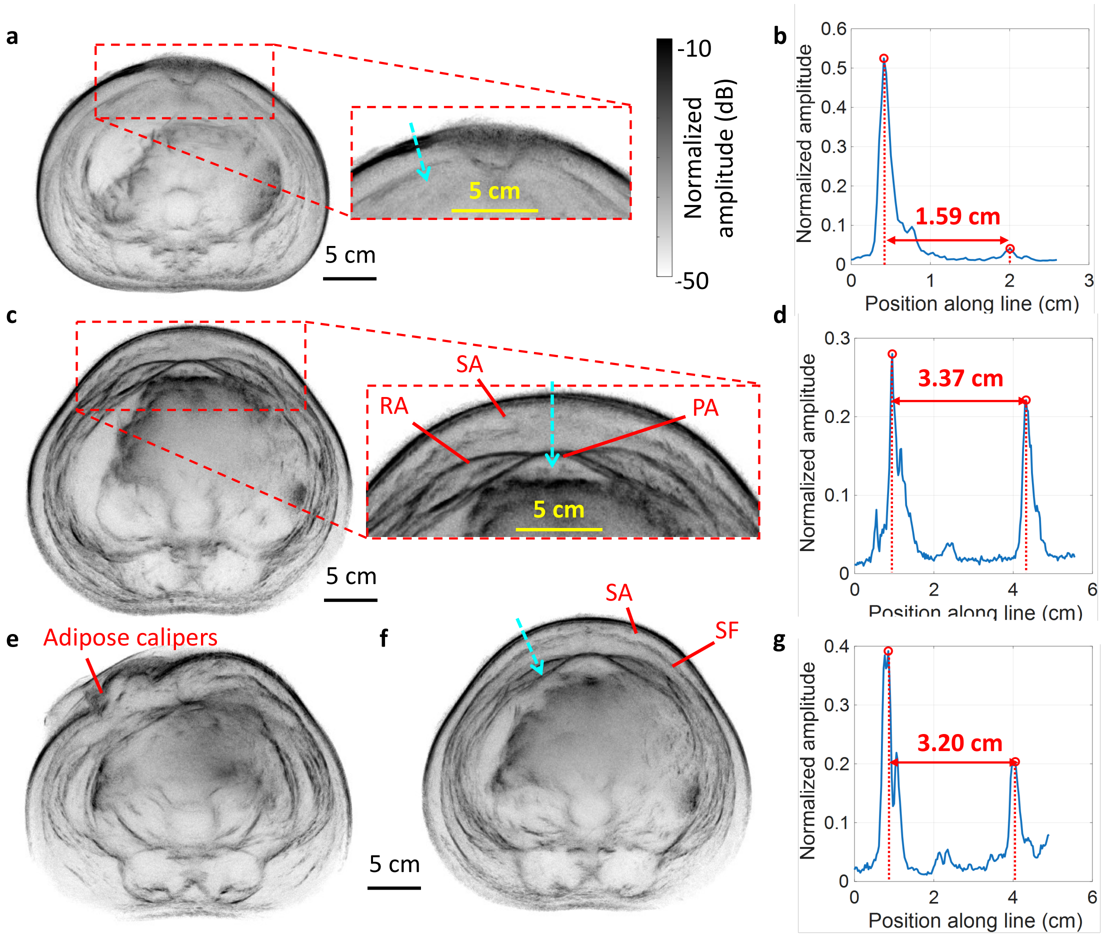

Figure 2.20. Abdominal adipose thickness assessment of healthy volunteers. Panels **a** and **b** show UST results for a 25-year-old female, and panels **c** to **g** are of a 27-year-old male. **a** UST image of a female volunteer. **b**, Image amplitude along the line drawn in **a** (in the direction of the arrow), estimating an adipose layer thickness of 1.59 cm near the navel. **c**, UST image of the entire body of a male volunteer, with an inset showing adipose regions in the anterior region of the abdomen. RA: rectus abdominus. SA: subcutaneous adipose. PA: preperitoneal adipose. **d**, Image amplitude along the line drawn in **c**. **e**, UST image with adipose calipers positioned on the abdomen. **f**, Abdominal image showing Scarpa's fascia (SF) in SA. **g**, Image amplitude along the line drawn in **f**, where the adipose calipers were also positioned.

Chapter 3

MICROWAVE ABLATION MONITORING USING THERMOACOUSTIC AND ULTRASOUND TOMOGRAPHY

Garrett, David C., Yousuf Aborahama, Jinhua Xu, Geng Ku, and Lihong V. Wang. "Microwave Ablation Monitoring Using Thermoacoustic and Ultrasound Tomography." In: *IEEE Journal of Microwaves* (2025). doi: 10.1109/JMW.2025.3612329

Abstract

Microwave ablation is an established minimally invasive technique that induces thermal necrosis in centimeter-scale tumors in organs such as the liver and kidney. However, the efficacy of clinical protocols is challenged by patient-specific and tissue-specific variations that may require personalized parameters to achieve optimal therapeutic outcomes. To address these limitations, we introduce an imaging technique employing modulated microwave signals that maintain peak and average powers comparable to those of existing clinical systems (~100–200 W). This modulation introduces time-varying tissue heating, generating detectable thermoacoustic signals that are used to reconstruct images proportional to the spatial heat deposition. When combined with thermal models of the tissue, we estimate the spatial temperature profile and ablation status over time. We validate this approach in *ex vivo* bovine liver compared against ultrasound tomography and tissue dissection. This approach may enable closed-loop monitoring and adaptive control of ablation procedures to optimize lesion coverage while sparing surrounding healthy tissue.

Introduction

Microwave ablation (MWA) has emerged as a preferred minimally invasive approach for treating cancerous tissues, offering reduced recovery times and lower complication risks compared to traditional surgical methods [74], [75]. Unlike radiofrequency ablation, which is limited by tissue charring and impedance changes that restrict energy delivery [76], MWA generates larger, more uniform heating zones through a needle-based radiating element [77], [78] typically operating at 915 MHz or 2.45 GHz. However, the success of MWA treatments relies on a delicate balance between comprehensive tumor cell elimination and the preservation of surrounding healthy tissue. Currently, clinical MWA protocols use standardized ablation parameters established from ex vivo bovine liver experiments, with microwave power (10–200 W) and duration selected according to the desired ablation size. However, patient- and tissue-specific variations may result in suboptimal ablation [79], [80], for instance, due to differences in tumor type or proximity to blood vessels. Although imaging modalities like CT and MRI can effectively evaluate the ablation zone post-procedure, neither of them offers practical methods of real-time assessment during treatment [81], [82]. Contrast-enhanced ultrasound can provide intraoperative visualization, but its usefulness is limited by operator dependence, shallow imaging windows, and the short lifespan of microbubbles in circulation (several minutes) [83]. This gap highlights the need for imaging technology that provides immediate and accurate intraoperative feedback during MWA procedures.

Thermoacoustic (TA) tomography has recently emerged as a promising method to track tissue changes during MWA. Thermoacoustic signals arise from time-varying heating rates in tissues due to transient microwave absorption. These MHz-scale acoustic signals are collected by acoustic detectors and are used to reconstruct images of the microwave absorption profile. TA systems have been more commonly developed for medical imaging, generally using high-power (~kW to MW) sources with sub-microsecond pulse duration. Two approaches have been investigated for TA monitoring of MWA: using an independent TA system with a separate antenna to image tissue property changes [84], [85], or simultaneously ablating and generating TA signals using a pulsed microwave source coupled to the ablation probe [86], [87]. Using a TA imaging system during MWA poses several practical challenges, including achieving sufficient imaging depth for clinically relevant tissue volumes, shielding other devices from the strong microwave signals, and positioning a separate antenna to illuminate the ablation region. Performing TA imaging using signals generated from the ablation probe is advantageous in isolating changes from the ablation region. Previous approaches using pulsed sources, however, require custom probe designs to avoid dielectric breakdown at high peak microwave power, have low average microwave power (<10 W), and require specialized microwave sources like pulsed magnetrons or klystrons. Demonstrations to date have been limited to single-element acoustic receivers, where the extracted parameters of time of arrival and amplitude may not be robust against patient positioning and tissue shrinkage. Furthermore, high-power microwave sources may not be compatible with the sensitive electronics present in clinical settings.

Here, we propose an approach for TA monitoring of MWA using similar peak (~190 W) and average (100 W) microwave powers as existing commercial systems. By modulating a 2.45 GHz continuous-wave (CW) microwave source at ultrasound-scale frequencies (~MHz), TA signals are generated without altering the heat deposition while providing spatial information on the deposited microwave energy. We perform this using a commercial microwave power amplifier and MWA probe. The TA signals are detected using a human-scale 512-element acoustic detector array, and they are used to obtain TA images of the ablated region with temporal resolution of 1 s throughout procedures of several minutes. We demonstrate this technique in ex vivo bovine liver samples. We calibrate our TA images to a heating function by considering the temperature-dependent thermal expansion coefficient in tissues like liver, which we relate to an observed initial rise in TA amplitude during the first few seconds of the procedure. Ultrasound tomography (UST) is also used to image the location of the needle with respect to tissue features and to observe tissue changes due to ablation. This approach could be readily adapted to commercial systems and may allow for more precise MWA treatment.

Methods

Our methodology is outlined in Figure 3.1. First, we excite the ablation probe using a modulated microwave source to generate detectable TA signals. We employ a linear chirp to enhance the signal-to-noise ratio (SNR) of broadband detected TA profiles given a limited peak microwave power. Due to their quadratic relation to the applied electric field, the resulting TA signals arise at twice the modulation frequencies. These TA signals are captured using a human-scale, 512-element ultrasonic ring array. The recorded signals are deconvolved with the expected chirp and are then used to reconstruct TA images throughout the ablation procedure. We then calibrate these images to estimate the heating function in absolute units, which serves as the source term in a thermal diffusion model incorporating temperature-dependent tissue properties. Finally, we estimate the ablation zone using the Arrhenius damage integral and compare it with photographs of the dissected tissue samples and with UST images captured before and after ablation.

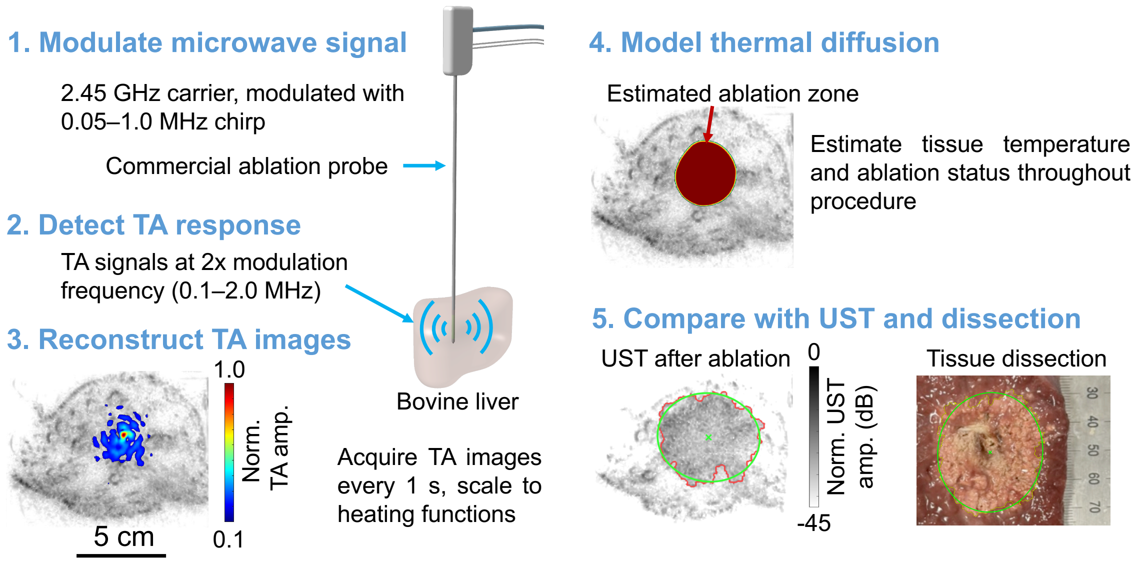

Figure 3.1. Overview of the methodology for thermoacoustic (TA) ablation monitoring. UST: ultrasound tomography.

Thermoacoustic signal generation

During time-varying microwave-induced heating $Q(\mathbf{r},t)$, the resulting TA pressure wave equation is [88]:

$$\left(\nabla^2 - \frac{1}{v_s^2(\mathbf{r})}\frac{\partial^2}{\partial t^2}\right) p(\mathbf{r},t,\tau) = -\frac{\beta(\mathbf{r},\tau)}{C_p(\mathbf{r},\tau)}\frac{\partial Q(\mathbf{r},t,\tau)}{\partial t}, \tag{3.1}$$

where $p(\boldsymbol{r}, t, \tau)$ is the TA pressure, v_s is the tissue speed of sound, β is the coefficient of thermal expansion, and C_p is the specific heat capacity at constant pressure. We use two time scales: t denotes the fast (~microseconds) variation introduced by the modulated microwave absorption, and τ denotes the slow (~seconds) variation due to temperature change and tissue ablation. Note that (3.1) is valid under thermal confinement, which is met with fast-time variation in the source term. The heating function in tissue due to narrowband microwave absorption is found as

$$Q(\boldsymbol{r}, t, \tau) = \sigma_{\text{eff}}(\boldsymbol{r}, \tau) E^2(\boldsymbol{r}, t, \tau), \tag{3.2}$$

where $E(\boldsymbol{r}, t, \tau)$ is the instantaneous scalar electric field amplitude. The static conductivity σ_s and dielectric loss ε_r'' are combined into a single term $\sigma_{\text{eff}} = \sigma_s + 2\pi f_c \varepsilon_0 \varepsilon_r''$, where f_c is the microwave carrier frequency. We assume that σ_{eff} is approximately constant over a narrow modulation frequency $f_m \ll f_c$, but that it may vary over ~seconds due to changing temperature and ablation status as water content and protein structures are altered. Magnetic losses are considered negligible in endogenous tissue ($\mu_r'' \sim 0$).

To generate detectable TA signals, we modulate the microwave carrier frequency $f_c = 2.45$ GHz at acoustic-scale frequencies using dual-sideband suppressed carrier (DSB-SC) modulation. To improve the signal-to-noise ratio (SNR) with a limited peak microwave power, we modulate the microwave carrier signal using a chirp. A similar approach has been used for TA imaging at nontherapeutic power levels [89]. The linear chirp has time-varying frequency $f_m(t) = f_r t + f_0$, where $f_r = (f_1 - f_0)/t_c$ is the linear chirp rate, $f_0 = 0.05$ MHz is the lower frequency, $f_1 = 1.0$ MHz is the upper frequency, and $t_c = 400$ µs is the chirp duration. These parameters are chosen based on the bandwidth of our acoustic receivers and the maximal recording time of our data acquisition hardware. The modulating chirp signal is

$$x(t) = \sin\left[2\pi\left(\frac{f_r}{2}t^2 + f_0 t\right)\right], 0 \leq t \leq t_c. \tag{3.3}$$

The temporal variation of the electric field is therefore:

$$E(\boldsymbol{r},t,\tau) = E_0(\boldsymbol{r},\tau)x(t)\sin(2\pi f_c t). \tag{3.4}$$

We assume that the electric field amplitude $E_0(\boldsymbol{r},\tau)$ is constant across the narrow modulation bandwidth but may vary slowly during the ablation procedure. Since the heating rate is proportional to the squared electric field,

$$\begin{gathered} Q(\boldsymbol{r},t,\tau) = \frac{1}{4}\sigma_{\text{eff}}(\boldsymbol{r},\tau)E_0^2(\boldsymbol{r},\tau)g(t), \\ g(t) = \left[1 - \cos\left[4\pi\left(\frac{f_r}{2}t^2 + f_0 t\right)\right] + A_{\text{MW}}(t)\right], \ \ 0 \le t \le t_c, \end{gathered} \tag{3.5}$$

where $A_{\text{MW}}(t)$ are terms with frequencies of $f_c \pm f_m$ and $2f_c$. Since f_c is in the GHz range, TA signals corresponding to these terms would quickly attenuate and fall outside of our detection band, so we do not consider them in our analysis. By differentiating (3.5) and substituting into the right-hand side of (3.1), the resulting TA source term is

$$p_s(\boldsymbol{r},t,\tau) = -\pi\frac{\beta(\boldsymbol{r},\tau)}{C_p(\boldsymbol{r},\tau)}Q_0(\boldsymbol{r},\tau)f_m(t)x_{2f}(t), \tag{3.6}$$

where $Q_0(\boldsymbol{r},\tau) = \sigma_{\text{eff}}(\boldsymbol{r},\tau)E_0^2(\boldsymbol{r},\tau)$ is the average heating function which is expected to vary on the order of seconds as the tissue becomes ablated, and $x_{2f}(t) = \sin[2\pi f_r t^2 + 4\pi f_0 t], 0 \le t \le t_c$ is the linear chirp at twice the modulation frequency (0.1–2.0 MHz). Note that the TA pressure is directly proportional to the average heating function $Q_0(\boldsymbol{r},\tau)$ in (3.6) but scaled through $-\pi\left(\frac{\beta(r,\tau)}{C_p(r,\tau)}\right)f_m(t)$. Importantly, the recovery of $Q_0(\boldsymbol{r},\tau)$ from the TA signals does not require knowledge of $\sigma_{\text{eff}}(\boldsymbol{r},\tau)$ or $E_0(\boldsymbol{r},\tau)$, which are difficult to estimate in tissues.

To maintain average microwave power comparable to clinical systems (100 W), after the chirp we apply a 9.5 ms single-tone modulating signal at half the power of the chirp. The modulation waveforms are shown in Figure 3.2, where we apply Hamming windows on the waveform edges to reduce sidelobes after deconvolution.

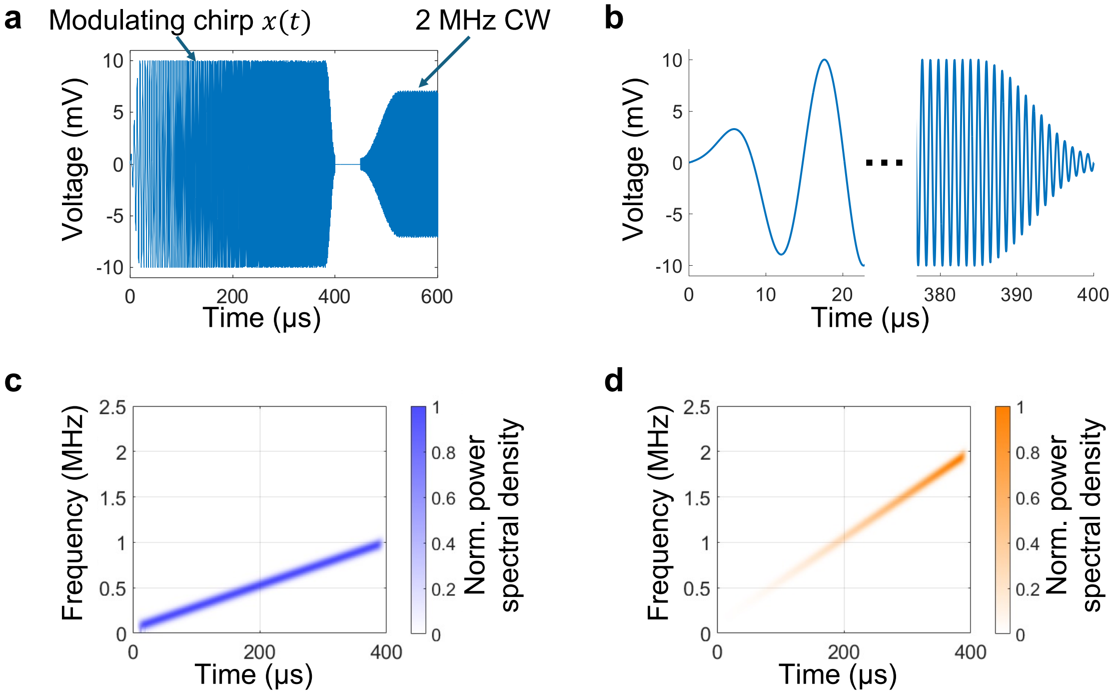

Figure 3.2. Modulating waveform and expected TA source signal structure. **a**, Time domain waveform used to modulate the 2.45 GHz microwave source. The 400 μs chirp is followed by a ~9.5 ms CW signal to maintain microwave energy deposition during a 10 ms period. **b**, Hamming windows are applied to the beginning and end of the chirp. **c**, Spectrogram of the modulating chirp spanning 0.05–1.0 MHz. **d**, Spectrogram of the expected TA signal source term, consisting of a ramp-weighted chirp spanning 0.1–2.0 MHz.

We then recover a pulse-like response $\chi_{s,i}(t)$ from the recorded TA signals $x_{\mathrm{TA},i}(t)$ on each detector i using Wiener deconvolution with the expected response $r(t) = (f_r t + f_0)x_{2f}(t)$:

$$\chi_{s,i}(t) = F^{-1}\left\{\frac{R^*(f)}{|R(f)|^2 + \lambda} X_{\mathrm{TA},i}(f)\right\}, \tag{3.7}$$

where F^{-1} denotes the inverse Fourier transform, $R(f)$ and $X_{\mathrm{TA},i}(f)$ are the Fourier transforms of $r(t)$ and $x_{\mathrm{TA},i}(t)$, respectively, and λ is a noise-to-signal parameter (set to 0.1) that regularizes the inversion. Multiplying this filter with the spectrum of the recorded signals suppresses noise amplification while compensating for the system response. The pulse-like responses $\chi_{s,i}(t)$ from each channel are then used to reconstruct images of the estimated heating function. Compared to a microwave pulse with similar peak power, a linear chirp results in an expected SNR improvement of $\sim \sqrt{t_c \cdot (f_1 - f_0)}$ [62].

System hardware

We show the system hardware in Figure 3.3. Note that a similar microwave power amplifier is used as in clinical systems [90], and that the microwave modulation only requires a modulating source (from a low-cost arbitrary waveform generator) and a mixer. The chirp waveform $x(t)$ is first programmed in an arbitrary waveform generator (AWG, Siglent SDG2042) and coupled to one input of a mixer (Analog Devices DC1983A) with 20 $\mathrm{mV_{pp}}$ maximum amplitude. The other mixer input is fed from a microwave source (LibreVNA) providing a 2.45 GHz CW signal at -1 dBm. The modulated signal is then amplified in two stages (Mini-Circuits ZX-60-43S+ and Mini-Circuits PHA-102+), followed by a high-power amplifier (Mini-Circuits ZHL-2425-250X+). The resulting modulated signal consists primarily of two first-order sidebands in the frequency domain at 2.45 GHz ± $f_m(t)$. The carrier and higher-order sidebands remain at least 15 dB below the first-order sidebands. We use an in-line power detector (Bird 5012D) to record the peak and average microwave power delivered to the probe. A circulator (Ditom D3C2327N) directs the reflected signals from the probe into a matched load.

We use a 20 cm Covidien Emprint ablation probe, which has a 2.45 GHz operating frequency and supports 100 W average power. The probe is water-cooled using a peristaltic pump during operation (Emprint Ablation Pump). A fiber-optic thermometer (Omega FOM-L201 and FOS-LT-5) is also inserted in the tissue to monitor the temperature. The tissue sample is immersed in water for acoustic coupling to the receiver array. It is mounted on a plastic support plate held by a single stainless-steel post.

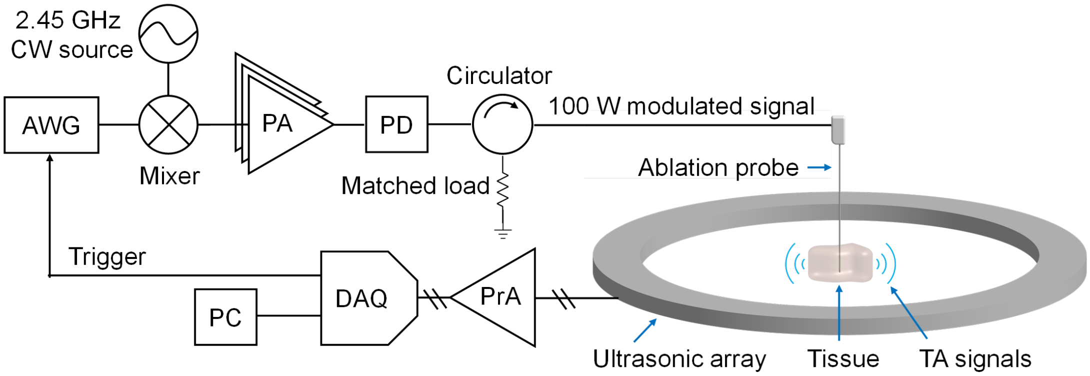

Figure 3.3. System hardware for thermoacoustic ablation monitoring. AWG: arbitrary waveform generator. PA: power amplifier (in three stages). PD: power detector. PrA: preamplifiers. DAQ: data acquisition module. PC: personal computer. CW: continuous-wave.

The ablation probe is inserted into tissue, and the generated TA signals are launched in water immersion. We detect the TA signals using the custom 512 element, 60 cm diameter acoustic receiver array with 1 MHz center frequency described in [91]. Each channel is preamplified by 15 dB and digitized in parallel at 5 MSPS (Photosound Legion) using 51 dB gain. We acquire TA signals at a 100 Hz repetition rate. On each trigger, the 400 µs chirp-modulated signal is delivered to the ablation probe. We average and store the detected signals every 100 shots, corresponding to 1-second acquisitions. Before and after microwave ablation, we also image the sample using UST with the approach described in [91]. We show an example spectrogram and deconvolved TA response from the ablation probe immersed in water in Figure 3.4. Note that the amplitude of the recorded chirp also depends on the spatial distribution of absorbers. For the broad absorption profiles found here, this results in a low-frequency weighting of the launched TA signals compared to the general source term shown in Figure 3.2.

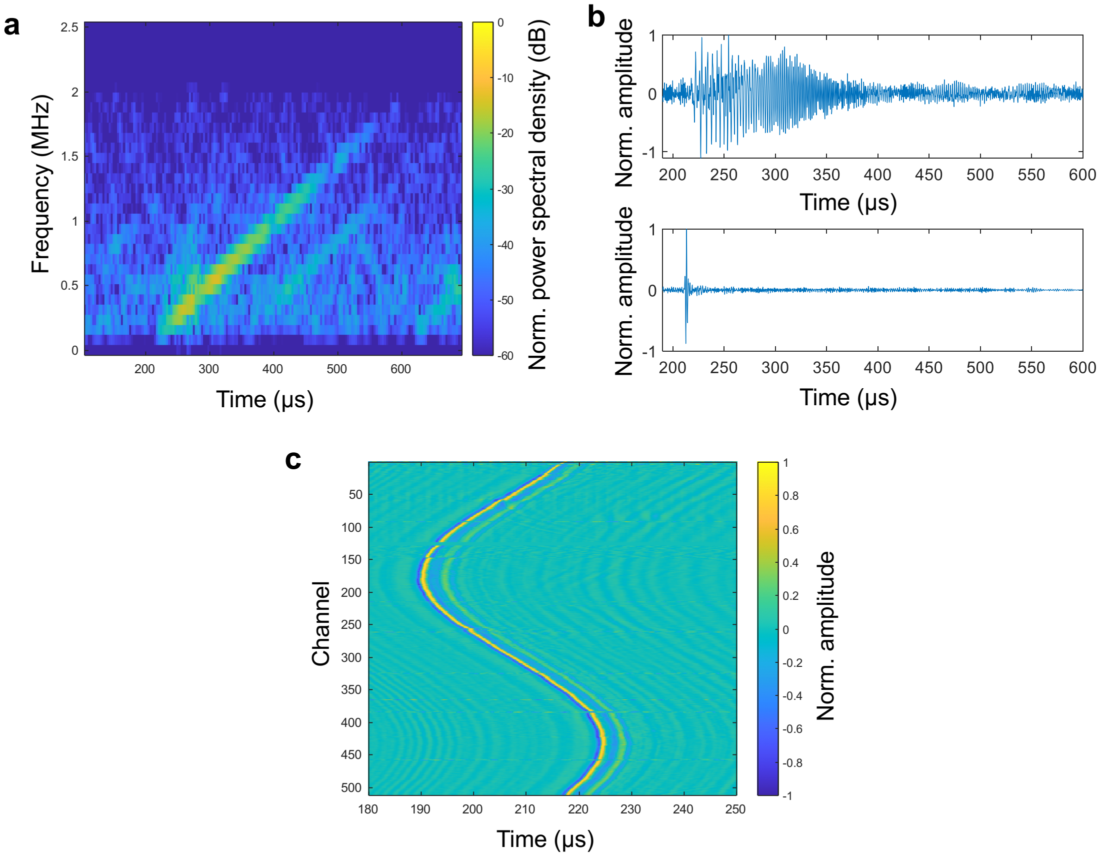

Figure 3.4. Recorded and deconvolved TA signals for the ablation probe in water. **a**, Spectrogram of an example recorded TA channel. The recorded chirp spans the expected range (~0.1–2.0 MHz) covering twice the modulation frequencies (0.05–1.0 MHz). **b**, Top: example recorded TA signal. Bottom: example TA signal after deconvolution with the expected scaled chirp response. **c**, Deconvolved response over all array elements. These signals are then used for image reconstruction.

Image reconstruction

The detected TA signals are deconvolved with the chirp waveform to recover a pulse-like representation. We then use universal back-projection [92] to recover a TA image proportional to the microwave absorption profile. For each frame, we perform reconstruction using both the deconvolved signals and their Hilbert transform, resulting in TA images $I_{\mathrm{TA,re}}$ and $I_{\mathrm{TA,im}}$. These images are combined as $I_{\mathrm{TA}}(\boldsymbol{r},\tau) = \sqrt{I_{\mathrm{TA,re}}(\boldsymbol{r},\tau)^2 + I_{\mathrm{TA,im}}(\boldsymbol{r},\tau)^2}$, which results in a non-negative image related to the heating function. We apply a 5 cm diameter circular mask centered on the probe to isolate the signal of interest and remove background noise from our thermal model.

We perform TA image reconstruction using a CUDA kernel called from MATLAB, computed using a NVIDIA A100 Tensor Core graphics processing unit (GPU). Reconstruction is performed over a 128 mm × 128 mm grid with 0.25 mm × 0.25 mm pixel size, consisting of 512 × 512 pixels. For each image, the required computational time is approximately 0.3 s. We reconstruct UST images using the method described in [91].

Thermal modelling

We model the thermal dynamics in tissue using the heat diffusion equation

$$\frac{\partial T(\boldsymbol{r},\tau)}{\partial \tau} = \nabla \cdot [\alpha(T(\boldsymbol{r},\tau))\nabla T(\boldsymbol{r},\tau)] + \frac{Q_0(\boldsymbol{r},\tau)}{\rho C_P(T(\boldsymbol{r},\tau))}, \tag{3.8}$$

where α is the thermal diffusivity and ρ is the mass density. These properties are expected to vary based on temperature T in °C as [93]

$$\begin{aligned} \rho C_P(T) &\approx 3.542 + 1.79 \times 10^{-4} \exp(0.233 \cdot T)\ [\mathrm{MJ} \cdot \mathrm{m}^{-3} \cdot {}^{\circ}\mathrm{C}^{-1}], \\ \alpha(T) &\approx 1.55 \times 10^{-7} + 4.95 \times 10^{-16} \exp(0.201 \cdot T)\ [\mathrm{m}^2 \cdot \mathrm{s}^{-1}]. \end{aligned} \tag{3.9}$$

where MJ denotes units of megajoules. The mass density is assumed constant [94]. We solve (3.8) numerically in 3D using a grid spacing of 0.25 mm and a time step of 10 ms.

We use the generated TA image series to estimate $Q_0(\boldsymbol{r},\tau)$. We first approximate the heating function distribution in the z dimension by considering the radiating region $r_{\mathrm{probe}} \approx 1$ cm along the ablation probe. We apply a weighting function $w(z) = \sqrt{r_{\mathrm{probe}}^2 - z^2},\ |z| < r_{\mathrm{probe}}$. To obtain heating function maps in absolute units, one method is to calibrate the array detection sensitivity where $Q_0(\boldsymbol{r},\tau)$ is then found by scaling the pressure in (3.6). However, acoustic attenuation and scattering in tissue may result in inaccurate absolute pressures recovered deep in tissue. Instead, we take advantage of the variation of β versus temperature near the beginning of the MWA procedure, where temperature increases rapidly before the tissue is ablated. We approximate the coefficient of thermal expansion as linear versus temperature:

$$\beta(T) \approx 3.5 \times 10^{-4} + 3 \times 10^{-6}(T - 37\ ^{\circ}\mathrm{C})\ [^{\circ}\mathrm{C}^{-1}]. \tag{3.10}$$

Since these values are not well characterized in the literature, we use an approximation similar to the temperature-dependence of β in water. We then approximate the TA images to the heating function through a scaling term K. Since for a fixed $Q_0(\boldsymbol{r}, \tau)$ the TA images would increase in amplitude proportionally to β during heating, we also normalize by the increase in $\beta(T)$:

$$Q_0(\boldsymbol{r}, \tau) \approx \frac{K}{\beta(\boldsymbol{r}, T)/\beta(\boldsymbol{r}, T_0)} w(z) I_{\mathrm{TA}}(\boldsymbol{r}, \tau). \tag{3.11}$$

We compare the TA amplitude rise with the modeled β rise to estimate K. We consider the mean of the TA image $I_{\mathrm{TA}}(\boldsymbol{r}, \tau)$ in a 5 mm diameter region around the probe tip, denoted $I_{\mathrm{TA,avg}}(\boldsymbol{r}_{\mathbf{tip}}, \tau)$, and the mean of the estimated β over the same region $\beta_{\mathrm{avg}}(\boldsymbol{r}_{\mathbf{tip}}, T)$. We normalize both the TA images and β estimates to $\tau = 0$, and we estimate K to minimize their difference over the first five seconds of ablation, with τ sampled in discrete 1-s increments:

$$\hat{K} = \underset{K}{\operatorname{argmin}} \sum_{\tau=0}^{\tau=5\ \mathrm{s}} \left[I_n(\boldsymbol{r}_{\mathbf{tip}}, \tau) - \beta_n(\boldsymbol{r}_{\mathbf{tip}}, T, K)\right]^2,$$

$$I_n(\boldsymbol{r}_{\mathbf{tip}}, \tau) = \frac{I_{\mathrm{TA,avg}}(\boldsymbol{r}_{\mathbf{tip}}, \tau)}{I_{\mathrm{TA,avg}}(\boldsymbol{r}_{\mathbf{tip}}, 0)}, \tag{3.12}$$

$$\beta_n(\boldsymbol{r}_{\mathbf{tip}}, T, K) = \frac{\beta_{\mathrm{avg}}\left(\boldsymbol{r}_{\mathbf{tip}}, T\big(K I_{\mathrm{TA}}(\boldsymbol{r}, \tau)\big)\right)}{\beta_{\mathrm{avg}}(\boldsymbol{r}_{\mathbf{tip}}, T_0)}.$$

Here, we assume that $Q_0(\boldsymbol{r},\tau)$ is constant over the first 5 s, which is supported by the relative consistency of $\sigma_{\text{eff}}(\boldsymbol{r},\tau)$ and the relative permittivity of liver tissue up to ~50 °C [95]. $T(KI_{\text{TA}}(\boldsymbol{r},\tau))$ numerically solves (3.8) using the heating function from (3.11) with scaling factor K.

From the modeled temperature in Kelvin $T_K(\boldsymbol{r},\tau)$ throughout the entire MWA procedure, we then estimate the tissue ablation status $\Omega(\boldsymbol{r},\tau)$ using the Arrhenius integral [96] as

$$\Omega(\boldsymbol{r},\tau) = A\int_0^{\tau} \exp\left(\frac{-E_a}{RT_K(\boldsymbol{r},\tau')}\right) d\tau'. \tag{3.13}$$

A tissue region is considered ablated if $\Omega > 1$, where approximately 63% of cells are likely to be ablated. We use typical values [97] for the frequency factor $A = 7.39 \times 10^{39}\ \mathrm{s}^{-1}$ and the activation energy $E_a = 2.577 \times 10^5\ \mathrm{J/mol}$. $R = 8.314$ J/(mol · K) is the universal gas constant. We model the temperature distribution over the entire ablation procedure and 60 s after microwave exposure. We treat β for ablated tissue as $3 \times 10^{-4}\ {}^{\circ}\mathrm{C}^{-1}$.

Results

We used samples of store-bought fresh bovine liver with an initial temperature of 15–20 °C. MWA was performed for durations of 1, 3, and 5 minutes at 100 W average power. In each case, TA signals were recorded and averaged over 1-s intervals continuously throughout the ablation procedure. Samples were immersed in room temperature water for acoustic coupling to the receiver array. An example TA frame overlaid on a UST image is shown in Figure 3.5. We first use the initial increase in TA image amplitude (~15–25% increase over the first 5 s) around the probe to scale to an estimated heating function $Q(r,\tau)$. The normalized average TA amplitude and β are shown in Fig. 5c for the estimated $\widehat{K}$ found from (12). From the estimated scaling factor and TA images, we then approximate the heating function using (3.11), which is used for thermal modelling.

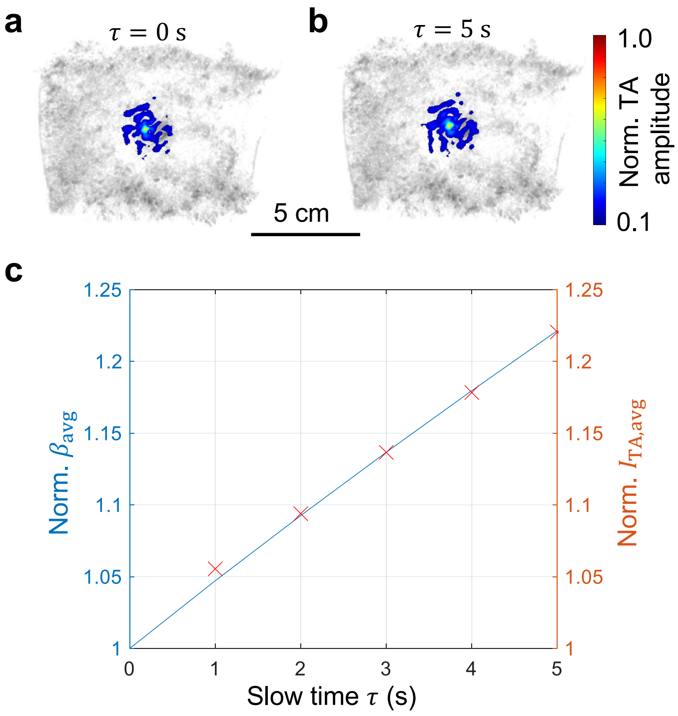

Figure 3.5. Scaling TA images to a heating function using the temperature-dependent coefficient of thermal expansion. **a**, TA image at $\tau = 0$ s overlaid on the UST image. **b**, TA image at $\tau = 5$ s overlaid on the UST image. **c**, Example of the average TA amplitude and estimated coefficient of thermal expansion in a 5 mm region around the ablation probe, both normalized to their value at $\tau = 0$ s. Both quantities exhibit near-linear increases. We minimized the differences between these values to estimate the scaling factor $\widehat{K}$.

We performed a UST acquisition approximately one minute after the ablation completion. We then dissected and photographed the liver tissues to assess the ablation diameter. For both UST images and the photographs, we segmented the ablated region and fit an ellipse to it. The ablation zone is estimated as the geometric mean of the major and minor axes of the ellipse. The estimated ablation diameters are compared in Figure 3.6. We also compare against the expected ablation widths using the manufacturer's specifications.

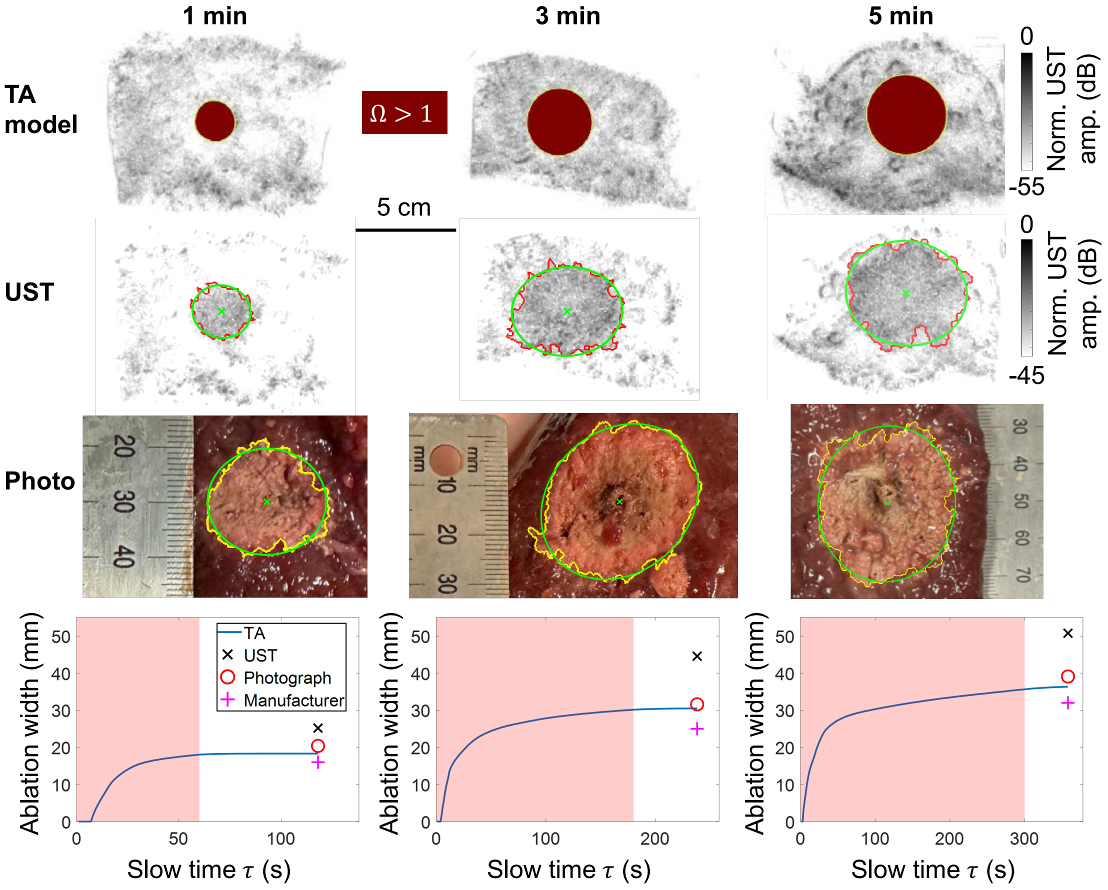

Figure 3.6. Estimated ablation zones from TA ablation monitoring, UST, and photographs of dissected samples. Columns show three example samples ablated for 1, 3, and 5 minutes. The first row shows the final frame of the estimated ablation zone using TA modelling, where red regions are considered ablated by the Arrhenius damage integral. The second row shows the UST image performed after ablation, where the ablation zone is segmented and fit to an ellipse. The third row shows photographs of the dissected tissue, where the ablation zone is segmented and fit to an ellipse. The final row shows the estimated ablation diameter from TA compared with the other estimates. The red window shows the time when microwave power is applied. We then simulate the thermal model for an additional 60 seconds to estimate the final ablation width.

Table 3.1. Estimated ablation widths from the manufacturer specifications, ultrasound tomography, thermoacoustic modelling, and photographs of the dissected tissues. Errors are calculated for each modality relative to the photographs.

Ablation time (min)	Photo est. (mm)	Manufacturer spec. (mm)	UST est. (mm)	TA est. (mm)	Manufacturer error (%)	UST error (%)	TA error (%)
1	20.4	16	25.2	18.3	-21.6	23.5	-10.2
	19.2		26.3	24.4	-16.5	37.4	27.4
3	31.6	25	44.6	30.5	-20.9	41.1	-3.5
	26.4		44.5	23.3	-5.3	68.4	-11.9
5	32.7	32	44.8	32.8	11.8	56.5	14.6
	39.1		50.8	36.4	-18.2	28.8	-7.0
Mean error (%)					**-11.8**	**42.6**	**1.6**
RMS error (%)					**16.7**	**45.4**	**14.6**

Our results for all six samples are summarized in Table 3.1. Note that UST consistently overestimates the ablation diameter compared with the photographs. This may be due to the generation of air bubbles and coagulation that increase acoustic scattering outside of the ablation zone, which has been previously observed [98]. We also highlight that for the 3- and 5-minute ablation durations, the ablation width varies by more than 4 mm between the two samples. Whereas the manufacturer specifications cannot discern differences between the two samples, the TA model tracks changes that may be due to differing tissue properties or structures. Despite our simplified model of the coefficient of thermal expansion, we find a lower overall RMS error using TA modelling compared with UST or the manufacturer's specifications. We expect this could further improve with better characterization of tissue properties over temperature and ablation status. Supplementary Videos 3.1-3.6 show the TA images, estimated temperature distributions, and estimated ablation zones throughout the ablation duration for each sample.

Discussion

This work introduces a TA imaging framework that models MWA progress and tissue dynamics during the ablation procedure. By modulating the microwave source at MHz-scale frequencies, we generate TA signals whose reconstructions map the spatial distribution of absorbed microwave energy. Treating these TA maps as the heating function term in a thermal diffusion model then provides ongoing estimates of tissue temperature and ablation status throughout the procedure. A brief calibration period, using the first few seconds of data and assuming a temperature-dependent thermal expansion coefficient, links TA image amplitude to absolute power deposition. This calibration implicitly accounts for the acoustic attenuation between the probe and detectors. Since this approach requires no hardware changes to typical MWA generators or antennas, the method is conveniently compatible with existing clinical systems.

This first demonstration highlights both this technique's promise and areas for refinement. Our implementation infers a 3D heating field from a stack of 2D TA slices, so true volumetric TA acquisition should improve accuracy. Experiments were performed in *ex vivo* bovine liver lacking perfusion, so future studies could incorporate blood flow, e.g., through the Pennes bioheat formulation [99] or porous-media extensions [100], to capture *in vivo* heat sinks. Although the technique avoids prior knowledge of tissue permittivity or antenna fields, it still relies on accurate temperature dependences for β and thermal diffusivity. Systematic measurements across tissue types will improve model accuracy and broaden applicability. Steam-generated bubbles could shadow TA signals late in ablation, leading to underestimation of deposited power. A fusion of UST and TA could help account for the acoustic attenuation caused by these bubbles.

The speed of sound in tissue is also expected to change during ablation, from ~1540 m/s at baseline (37 °C) to a maximum of ~1560 m/s at 60 °C [101]. Over a 5 cm diameter ablation zone, this could cause a ~0.6 mm error in our reconstruction of the microwave absorption profile. This would lead to incoherent summation of higher frequency signals recorded with wavelengths less than ~1.2 mm, but the lower frequencies are expected to remain robust to speed of sound changes. Future approaches could perform UST speed of sound estimation throughout the procedure to account for variation during ablation.

To achieve a human-scale field of view, our UST system uses lower frequency (~1 MHz) ultrasound compared to conventional handheld probes (~5–15 MHz). This results in poorer resolution. However, for imaging broader tissue changes like cm-scale tissue necrosis, lower frequencies may be advantageous in visualizing regions deep in the body with reduced acoustic attenuation.

To improve its clinical practicality, skin-coupled detector arrays mounted with an inflatable water bag or conformal pads could collect TA data without immersing the patient in water. Embedding one or more thermocouples in the probe would tighten model calibration and provide a real-time safety check. The hybrid of TA imaging (for energy deposition) and UST (for anatomy) may offer several complementary advantages in the future. UST could run concurrently to provide structural context, measuring temperature-induced speed-of-sound shifts, and identifying macroscopic tissue shrinkage. This may help refine the TA image reconstruction, correct acoustic path aberrations, and improve the fidelity of the thermal model.

In summary, we present a TA-guided thermal-modeling approach that delivers ongoing maps of energy absorption, temperature, and ablation progress during MWA. With continued work on volumetric imaging, perfusion modeling, and bubble mitigation, this technique could enable closed-loop control that adapts power and duration to patient-specific tissue responses, ultimately improving the precision and safety of thermal ablation therapies.

Supplementary Information

System hardware

An image of a sample before ablation is shown in Figure 3.7. The liver sample is immersed in water for acoustic coupling to the receiver array. It is mounted on a plastic support plate held by a single stainless-steel post.

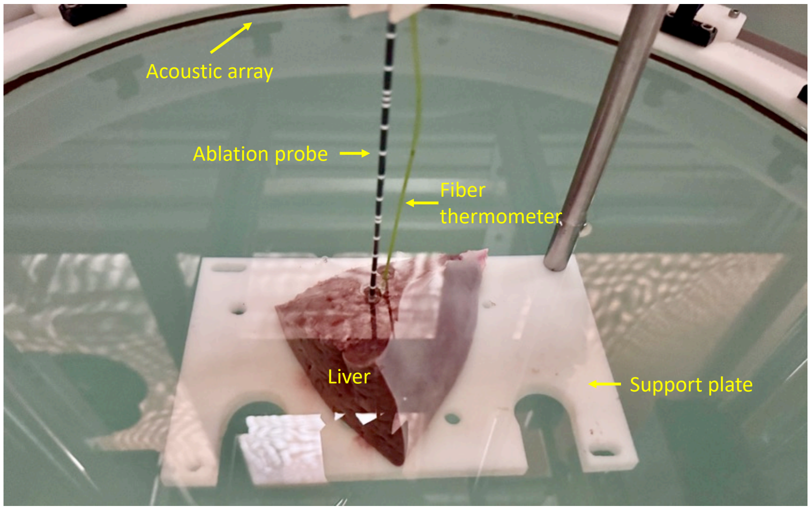

Figure 3.7. Photograph of an *ex vivo* bovine liver sample before ablation.

TA amplitude variation during the ablation procedure

Figure 3.8 presents the mean TA image amplitude in the tissue immediately surrounding the microwave probe during a 60 s ablation. The initial ~25 % rise over the first ~8–10 s is attributed to the temperature-dependent coefficient of thermal expansion, which we use to scale the TA images to the heating function in eq. (11). The sharp drop in amplitude at ~9 – 15 s is likely due to this region ablating, which agrees with the onset of ablation in our thermal model. After ablation, the microwave absorption drops due to lower water content, resulting in weaker thermoacoustic signals. This is consistent with the rapid drop in the conductivity reported in [102]. The slight increase in amplitude around 35 s could be due to the perfusion of surrounding blood or water perfusing back to the probe, but this would need to be confirmed with further experiments.

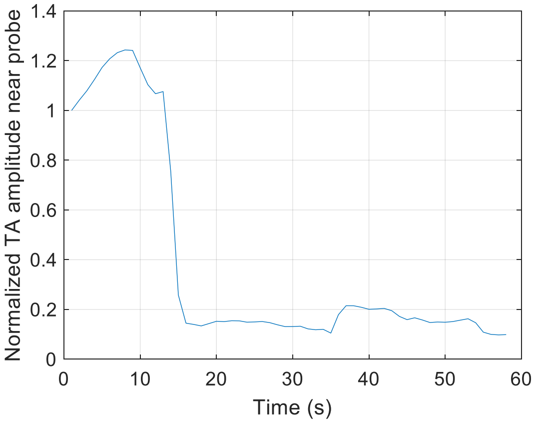

Figure 3.8. Example mean TA image amplitude near the probe during a 1-minute ablation.

Scaling TA images to heating functions

Since our TA images are dimensionless (normalized to the peak amplitude over the ablation time series), we scale them to a heating function through a parameter K. We do this by comparing the amplitude rise in the TA images over the first ~5 seconds with the estimated rise in the coefficient of thermal expansion (Figure 3.9a) found from the modelled temperature using eq. (9). We choose the scaling factor that minimizes the difference of the normalized TA amplitude and β (Figure 3.9b).

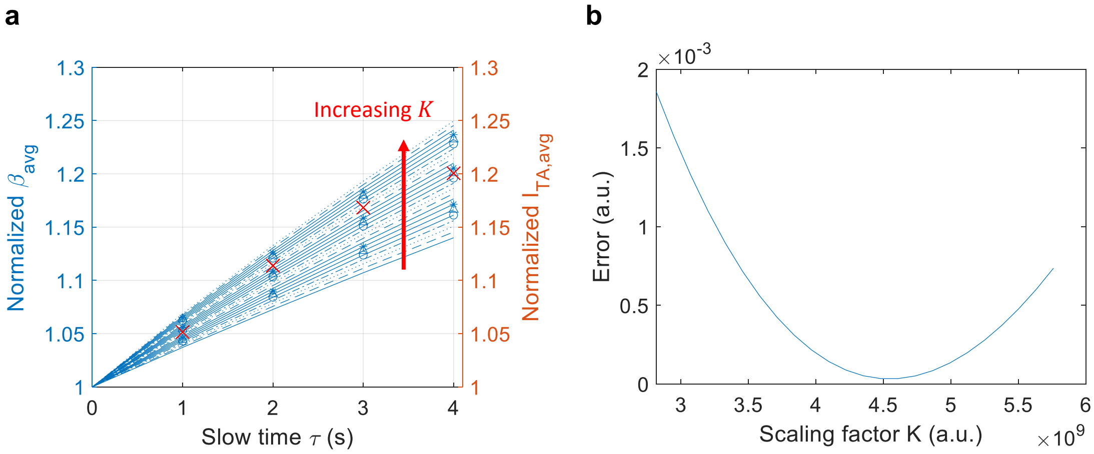

Figure 3.9. Determining the scaling factor K between TA images and heating function. **a**, Example of the normalized TA amplitude rise (red crosses) and normalized β from the thermal model (blue curves) for a given scaling factor K. **b**, Error between normalized TA amplitude and β for a range of K. The optimal K is chosen to minimize this error.

Comparison with thermometer

We recorded the temperature at 1-second intervals throughout the ablation using a non-conductive fiber thermometer. We extract the location of the thermometer relative to the probe using the UST image before ablation (Figure 3.10a). A comparison between the thermometer and TA models is shown in Figure 3.10b for a 5-minute ablation. The TA model tracks the initial rise in temperature and the steady high temperature (~100 °C) until the last ~60 seconds, where the thermometer shows a discrete drop then rise in temperature. This may be due to porous regions in the liver sample vaporizing between different compartments, but this phenomenon will require further research. Note that this sample was used for model validation, and it is not included in the six samples we used for ablation width comparison.

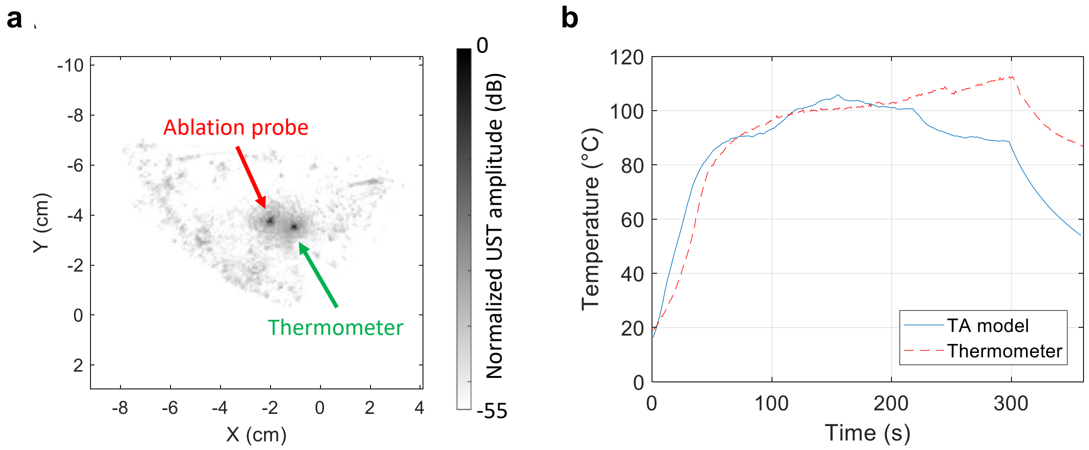

Figure 3.10. Extracting fiber thermometer location from UST and comparing estimated temperature against UST model. **a**, UST image of a liver sample before ablation, showing the location of the ablation probe and fiber thermometer. **b**, Comparison of the estimated temperature at the thermometer location from the TA model and fiber thermometer.

Thermal solver

We solve the transient 3D heat equation on a uniform Cartesian grid with uniform spacing of 0.25 mm by an explicit forward-time central-space (FTCS) solver on the GPU (MATLAB gpuArray, single precision). At every time step (10 ms), the specific heat and thermal conductivity of *ex vivo* liver are updated with the empirical fits in eq. (8). The volumetric source term comes from a time-ordered stack of 2D scaled TA images that are axially weighted in the z dimension. The heating function is normalized by the temperature-dependent thermal expansion coefficient ratio to preserve TA calibration to heating function. Cumulative thermal damage is tracked throughout the simulation using the Arrhenius integral. Once $\Omega > 1$, the modeled β is switched to a permanently reduced value ($3 \times 10^{-4}\ {}^{\circ}\mathrm{C}^{-1}$) to emulate ablated tissue. During the simulation, we ensure that the FTCS stability condition is met: $dt \leq (\min(\rho C_p))\, dx^2/(6\max(k))$.

We validate our thermal solver using a 3D instantaneous heat source at $\tau = 0$ s with spatial Gaussian variance $2\gamma = 2(1\ \mathrm{mm})^2$, total source energy $E_h = 10$ J, and initial background temperature $T_0 = 20\ {}^{\circ}\mathrm{C}$. We consider a medium with uniform, temperature-invariant properties: $C_p = 3600\ [\mathrm{J} \cdot \mathrm{kg}^{-1} \cdot \mathrm{K}^{-1}]; \rho = 1000\ [\mathrm{kg} \cdot \mathrm{m}^{-3}]; k = 0.52\ [\mathrm{W} \cdot \mathrm{m}^{-1} \cdot \mathrm{K}^{-1}];\ \alpha = k/\rho C_p$.

This results in an initial temperature distribution of:

$$T(\boldsymbol{r}, 0) = T_0 + \frac{E_h}{\rho C_p (4\pi\gamma)^{3/2}} \exp\left[-\frac{|\boldsymbol{r}|^2}{4\gamma}\right]. \tag{3.14}$$

We insert this distribution in our solver as an initial condition. The theoretical solution is found as [103]:

$$T(\boldsymbol{r}, \tau) = T_0 + \frac{E_h}{\rho C_p [4\pi(\gamma + \alpha\tau)]^{3/2}} \exp\left[-\frac{|\boldsymbol{r}|^2}{4(\gamma + \alpha\tau)}\right], \qquad \tau > 0. \tag{3.15}$$

We compare the theoretical and numerical results in Figure 3.11, where we find close agreement. The temperature ranges from $\sim 20 - 80\ {}^{\circ}\mathrm{C}$, but the maximum error over the entire volume and simulation duration is 0.07 °C.

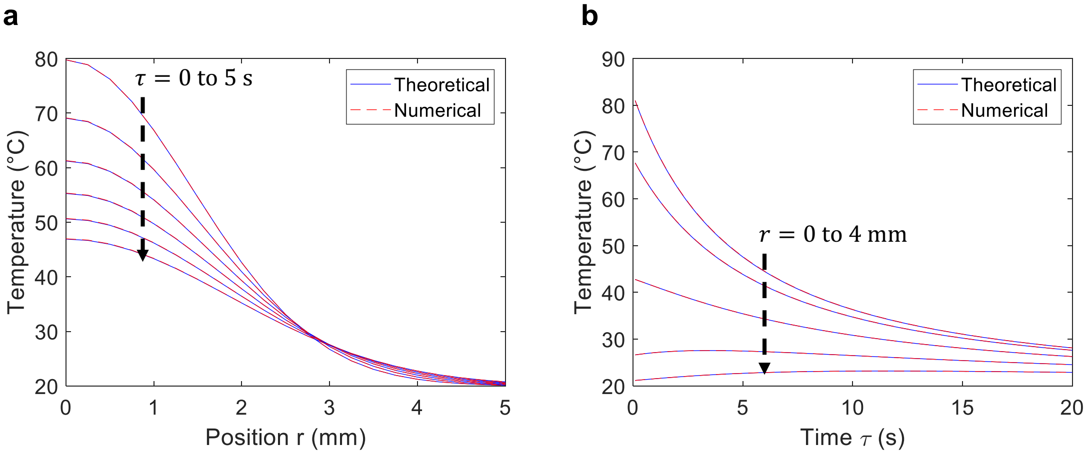

Figure 3.11. Validating our thermal solver against a theoretical solution for an instantaneous 3D Gaussian thermal source. **a**, Theoretical and numerical solutions as a function of position r. The six curves are shown for τ of 0, 1, 2, 3, 4, and 5 s. **b**, Theoretical and numerical solutions as a function of time τ. The five curves are shown for r of 0, 1, 2, 3, and 4 mm from the source center. The maximum error for the entire simulation volume and duration is 0.07 °C.

Ablation widths for all samples

The estimated ablation zones are shown for all samples using UST in Figure 3.12 and from photographs in Figure 3.13. We first segment the estimated ablation zone boundary using a graph cut in the MATLAB Image Segmentation toolbox. We then fit an ellipse to the segmented boundary and extract the major and minor axis diameters, where the mean ablation width is found as their geometric mean.

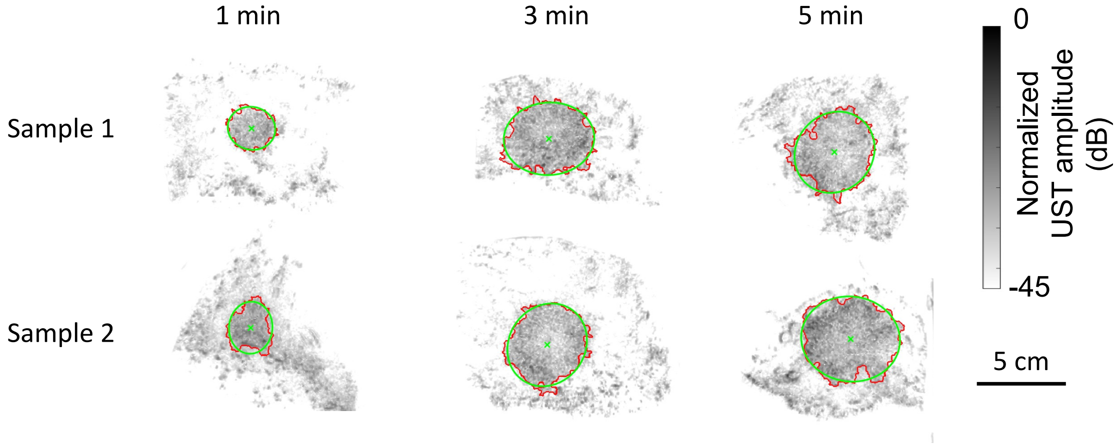

Figure 3.12. Estimated ablation zones in the plane normal to the ablation probe from UST. Red contours show the segmented boundaries. Green curves show the fit ellipses to the segmented boundaries.

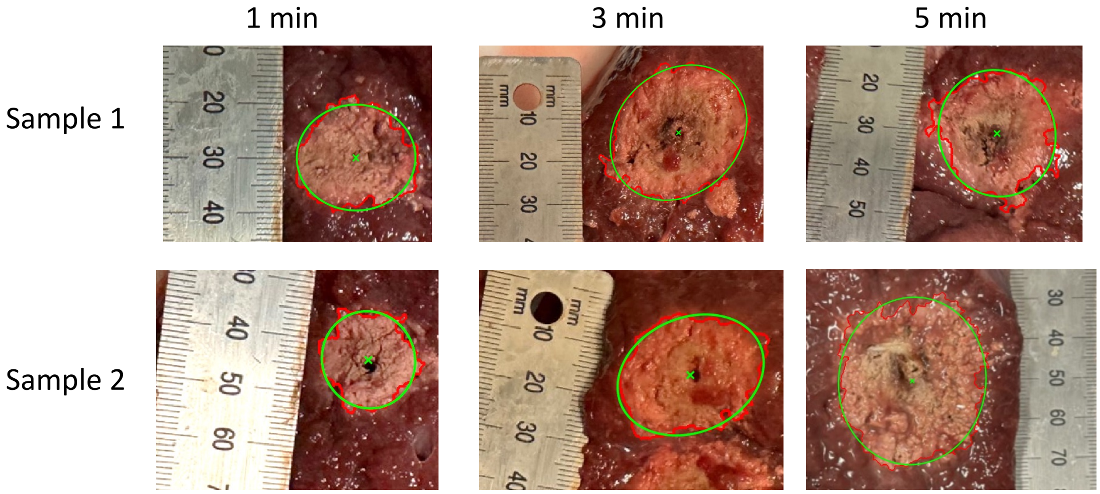

Figure 3.13. Estimated ablation zones in the plane normal to the ablation probe from photographs of dissected samples. Red contours show the segmented boundaries. Green curves show the fit ellipses to the segmented boundaries.

Chapter 4

AN INGESTIBLE LIGHT SOURCE FOR DEEP PHOTOACOUSTIC IMAGING

Garrett, David C. and Lihong V. Wang. "An Ingestible Light Source for Deep Photoacoustic Imaging." In: *arXiv preprint* arXiv:2601.01667 (2026).

Abstract

Photoacoustic tomography leverages ultrasound's deep tissue penetration to retrieve optical absorption contrast well beyond the optical diffusion limit. Conventional photoacoustic systems rely on externally delivered light and are therefore constrained by optical attenuation, limiting imaging depths to several centimeters. Here, we overcome this constraint using a compact, acoustically powered device that provides optical excitation directly from within the target medium. By exploiting the weak attenuation of low-MHz ultrasound, acoustic energy is transmitted through tissue to wirelessly power a pulsed laser diode. The emitted light pulses generate photoacoustic signals that encode local optical absorption at clinically relevant depths, which could enable imaging in regions such as the gastrointestinal tract that are inaccessible to surface-based illumination. We demonstrate this approach by imaging through a 12 cm thick phantom, establishing a pathway toward deep-tissue photoacoustic imaging.

Introduction

Since the early 2000s, capsule endoscopy (CE) has provided a minimally invasive means of imaging the gastrointestinal (GI) tract [104], [105], offering direct views of small intestine segments that upper or lower endoscopy cannot reach [106]. Compared with conventional endoscopy, CE is less invasive, does not require sedation, and enables prolonged monitoring as the capsule transits the GI tract [107], [108]. Ingestible CE devices contain a battery-powered camera and light source, and the images are transmitted wirelessly using radiofrequency signals to receivers positioned outside the body. However, since CE relies on conventional white-light photography, it reveals only the mucosal tissue surface [109]. Pathologies that reside within or beyond the bowel wall, such as transmural inflammation, angiodysplasia, or submucosal tumors, may not be detected [110]. An imaging modality capable of probing through the GI tract wall is therefore needed to improve the diagnosis and management of conditions like Crohn's disease, vascular malformations, and abdominal cancers [111].

MRI and CT provide excellent structural images of the abdomen, and endoscopic [112] and capsule-based [113] ultrasound systems can image beyond the mucosal wall. However, none of these modalities offer the functional and molecular contrast provided by optical imaging, such as visualization of blood vessel density. Photoacoustic tomography (PAT) is advantageous in imaging optical contrast at cm-scale depths beyond the tissue surface. Using high pulse-energy laser sources (~1 J), imaging depths of several centimeters have been obtained in regions like the breast [16], [17], [114]. These images reveal rich optical contrast relating to, for instance, blood oxygenation. However, to image regions deeper in the body like the GI tract using external illumination, PAT is limited by the effective attenuation coefficient $\mu_{\text{eff}} \sim 0.9 - 1.74\ \text{cm}^{-1}$ [16], [88]. At depths of several centimeters, the optical fluence is highly attenuated and results in prohibitively weak photoacoustic signals.

To perform PAT deeper in the body, photoacoustic endoscopy has been developed, where optical excitation is guided into the GI tract using optical fibers [115], [116]. The resulting acoustic signals are detected on the same endoscopic tether and are used for image reconstruction. However, tethered photoacoustic endoscopes are similarly constrained by the anatomical reach of conventional upper or lower endoscopes. Furthermore, these systems would require patient intubation and sedation, limiting their suitability for routine screening or longitudinal monitoring. There is therefore a gap in minimally-invasive technologies for imaging beyond the mucosal surface through the entire GI tract.

Here, we introduce an approach that enables wireless PAT (WPAT) at acoustically scalable depths well beyond the optical diffusion length. This device housing has a form factor comparable to existing CE devices (26 mm length, 11 mm diameter). PAT typically employs high-energy tabletop lasers, but here we perform PAT using a compact laser diode. Since MHz-scale acoustic waves propagate much deeper into the body, we use an external ultrasound transmitter to power the device and record the generated photoacoustic signals with a human-scale receiver array (60 cm in diameter). To synchronize optical excitation with ultrasound detection, electromagnetic pulses are received by the device and are used to trigger a pulsed 905 nm laser diode. We demonstrate WPAT by imaging a target through a 12 cm thick agar phantom.

Methods

The WPAT device consists of three modules (Figure 4.1): optical excitation, acoustic power rectification, and electromagnetic triggering. Optical excitation is performed using a 905 nm laser diode, where ~0.6 μs, ~130 μJ pulses are discharged using a capacitor bank and a high-current field-effect transistor (FET). We choose this wavelength based on its deep tissue penetration and laser diode availability for LiDAR applications. Wireless power transfer is done acoustically using a 500 kHz receiving transducer, followed by a Cockcroft-Walton voltage multiplier circuit to maintain uniform input impedance while charging the capacitor bank. We trigger the laser firing using electromagnetic pulses, where a conformal helical antenna receives signals which are then rectified and fed to a monostable multivibrator circuit to generate consistent pulse durations. The resulting photoacoustic signals propagate through ~30 cm of water and are detected by a 60 cm diameter, 512-element ultrasound receiver array, which we have used for *in vivo* whole cross-sectional human imaging [117].

Each module is fabricated on a separate 0.4 mm thick printed circuit board (PCB), and they are interconnected using board-to-board wiring. We model the device dimensions from commercial CE devices like the Medtronic Pillcam, CapsoVision CapsoCam, and Olympus EndoCapsule [118], [119]. This small size severely constrains the available components and requires several design choices to maximize performance despite the small device volume. Furthermore, the power budget for the design is strongly constrained by acoustic power transfer. We seal the enclosure using polydimethylsiloxane (PDMS) due to its transparency at 905 nm [120], similar acoustic impedance to water and tissue [121], and durability and biocompatibility in ingestible applications [122].

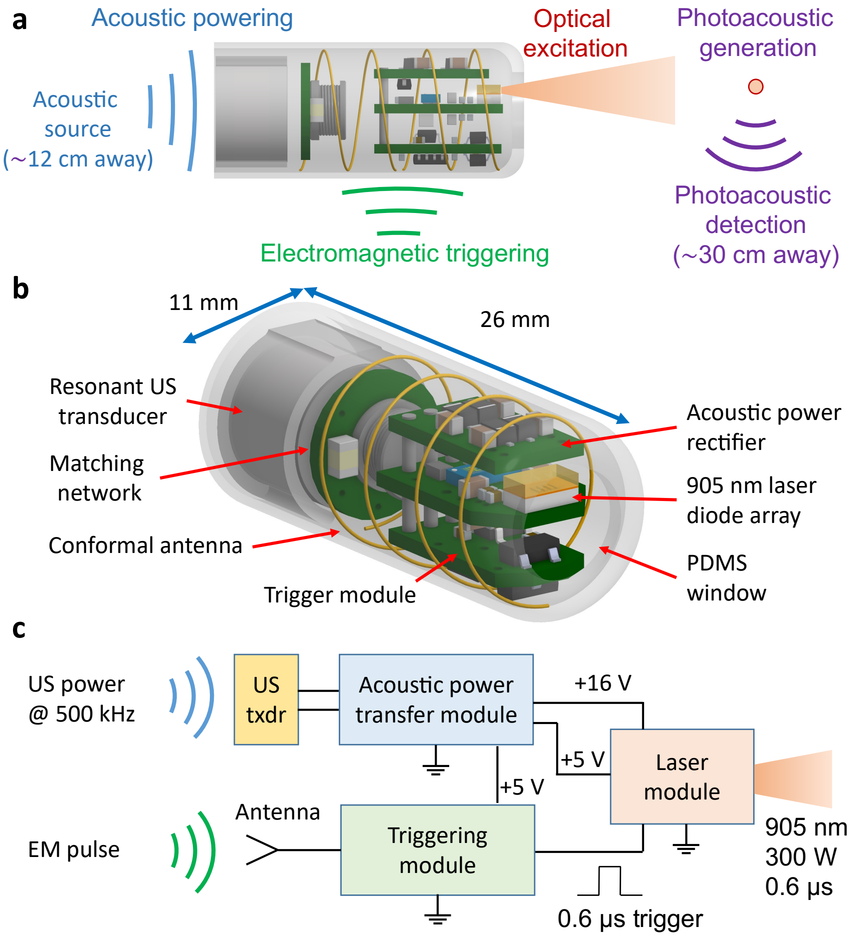

Figure 4.1. Wireless photoacoustic tomography device. **a**, Overview of the energy sources used for powering, triggering, and exciting photoacoustic signals deep in tissue. **b**, Model of the assembled device. **c**, Block diagram of the device modules.

Optical excitation

The laser excitation module (Figure 4.2) consists of a pulsed 905 nm surface-mount laser diode array (Excelitas TPGAD1S11A-4A) driven for high peak-power operation. All four emitters are fired simultaneously to achieve ~300 W peak optical output during ~0.6 μs pulses. The diode is switched using a low-inductance gallium nitride FET (EPC2015), controlled by a gate driver (LMG1020), while a capacitor bank pre-charged to 15 V supplies the required current (~30 A peak). To achieve sharp optical pulses, we position the laser diode between two rows of capacitors totaling 4.5 μF where lines of vias are used to reduce the inductance during rapid high-current discharging. These capacitors are charged during the acoustic power transfer phase and are partially discharged during excitation.

We recorded the average optical pulse energy as 130 μJ using a photodiode power sensor (Thorlabs S120C). We compare this with the electrical energy consumed, which is found by the voltage drop on the charged capacitor bank from 15 V to ~9 V, where the electrical pulse energy is $E_{LD} = \frac{1}{2}C\left(V_i^2 - V_f^2\right) \sim 324$ μJ. This results in an electrical-to-optical efficiency of ~40%.

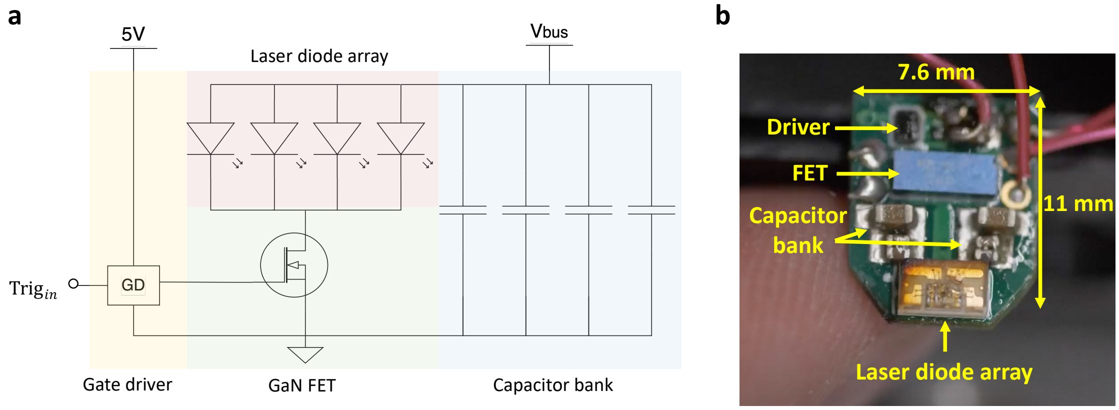

Figure 4.2. Optical excitation module. **a**, Simplified circuit diagram. GD: gate driver. GaN: gallium nitride. **b**, Assembled module.

Acoustic power transfer

With an average per-pulse electrical energy consumption of ~324 μJ, operating the laser at a 50 Hz repetition rate requires ~16 mW average electrical power. The quiescent power consumption of the other device components is < 1 mW. An internal battery could enable short-term operation, but the capsule must remain functional throughout its multi-hour GI transit, so relying on battery power alone would limit imaging duration. The required power is greater than what typical inductive or RF-based wireless power transfer systems report for deep tissue implants [123]. We instead take advantage of the low attenuation and guided energy delivery enabled by MHz-scale ultrasound. Ultrasound-based wireless power transfer has been demonstrated to yield mW-scale power to deeply implanted mm-sized devices [124], [125]. Furthermore, a single external acoustic array may in the future perform both ultrasound power delivery and photoacoustic detection, simplifying the clinical workflow while enabling shared calibration methods like sound speed correction that enhance both powering and imaging performance.

To wirelessly supply the ~16 mW average power required for laser operation, we first consider the acoustic safety limits. The FDA specifies a spatial peak temporal average intensity $I_{SPTA} < 720$ mW/cm^2, which we treat as the maximum acoustic intensity that can occur in tissue or on the capsule surface, and a mechanical index (MI) < $1.9\ \mathrm{MPa}/\sqrt{\mathrm{MHZ}}$. Given our acoustic receiver surface area of 0.28 cm^2, up to ~200 mW of acoustic power can therefore be incident on the receiver. Achieving the required electrical output therefore requires an acoustic-to-electric conversion efficiency > 8%. Note that we optimize here for the total received electrical power when constrained by the safety standards rather than the efficiency of the entire acoustic link.

The chosen operating frequency is a trade-off between energy penetration and device size. Lower frequencies reduce tissue attenuation but require thicker transducers (for thickness-mode resonance) and, for a given peak rarefactional pressure, yield a higher mechanical index. We select 500 kHz as a balanced compromise. To efficiently convert acoustic energy into electrical power, we developed a custom 500 kHz compact resonant receiver. PZT-5A was selected as the piezoelectric material for its high electromechanical coupling factor ($k_{33} = 0.72$). The total acoustic-to-electrical power efficiency at resonance is governed by acoustic and electrical impedance matching and is ultimately limited by internal mechanical loss and dielectric loss, with higher k_{33} generally supporting greater achievable efficiency [126]. The parameter k_{33} characterizes the strength of electromechanical coupling and is related to the separation between resonance and antiresonance, rather than directly specifying acoustic-to-electrical power efficiency. In practice, the delivered electrical power fraction is described by an equivalent-circuit view in which matching determines how much of the converted power reaches the load versus being dissipated internally (see Supplementary Information).

The outward-facing surface of the transducer is bonded to silver epoxy (MG 8330), acting as both a quarter-wave matching layer and an electrical connection. With an acoustic impedance of ~6 – 7 MRayl, silver epoxy is close to the ideal quarter-wave matching impedance $\sqrt{\mathrm{Z_{tiss}\,Z_{tran}}}$ ~ 7.3 MRayl needed to couple energy effectively between tissue ($\mathrm{Z_{tiss}} = 1.5$ MRayl) and PZT-5A ($\mathrm{Z_{tran}} = 36$ MRayl). The inner surface is air-backed to increase mechanical resonance and to prevent unwanted energy leakage into the capsule interior. At resonance, the receiver has an electrical impedance of 3.78 kΩ $\angle -47.8°$ as measured with an LCR meter (Hioki 3532-50).

The received 500 kHz electrical signal must then be rectified and stored for pulsed laser operation. We employ a two-stage Cockcroft-Walton voltage-multiplying circuit (Figure 4.3a), selected for its stable input impedance while charging the capacitor bank. The input impedance of the generator is measured as 186.1 Ω $\angle -12.2°$ during charging. An LC matching network is inserted between the receiver and multiplier circuit to maximize power transfer.

Acoustic power is delivered using a flat 1.5-inch diameter 500 kHz transducer (Olympus V389-SU) driven by an arbitrary waveform generator (Siglent SDG2042X) and power amplifier (E&I 350L). We also electrically match the transmitting transducer (150.3 Ω $\angle -78.2°$) to the 50 Ω power amplifier using an LC matching network. The flat transmitting aperture produces a broad axial region of near-uniform intensity near the Rayleigh length $\mathrm{D_{ray}} \sim D^2/4\lambda \sim 12$ cm, reducing sensitivity to capsule positioning. Given the uncontrolled motion and in the GI tract, this could improve the reliability of received power delivery compared with a sharply focused transmitter. Here, we maximize the safety-limited acoustic intensity that is converted into electrical energy at the capsule rather than the efficiency of the entire acoustic power transfer link.

We then used this system to wirelessly charge the capacitor bank used for laser firing, where a linear increase in voltage is found during the charging period (Figure 4.3b). A Zener diode is also used to limit the rectified DC voltage to 15 V, where additional acoustic power received after the capacitor bank is charged to 15 V is dissipated through the Zener diode. Using a calibrated hydrophone (Onda HGL-0085), we measured the peak acoustic pressure as $p_{\text{pk}} = 210$ kPa, corresponding to a mechanical index of ~0.3. This results in a peak acoustic intensity of $p_{\text{pk}}^2/2Z_a \sim 1.47\ \text{W}/\text{cm}^2$, so a maximum duty cycle of ~49% can be used while remaining within the safety standards.

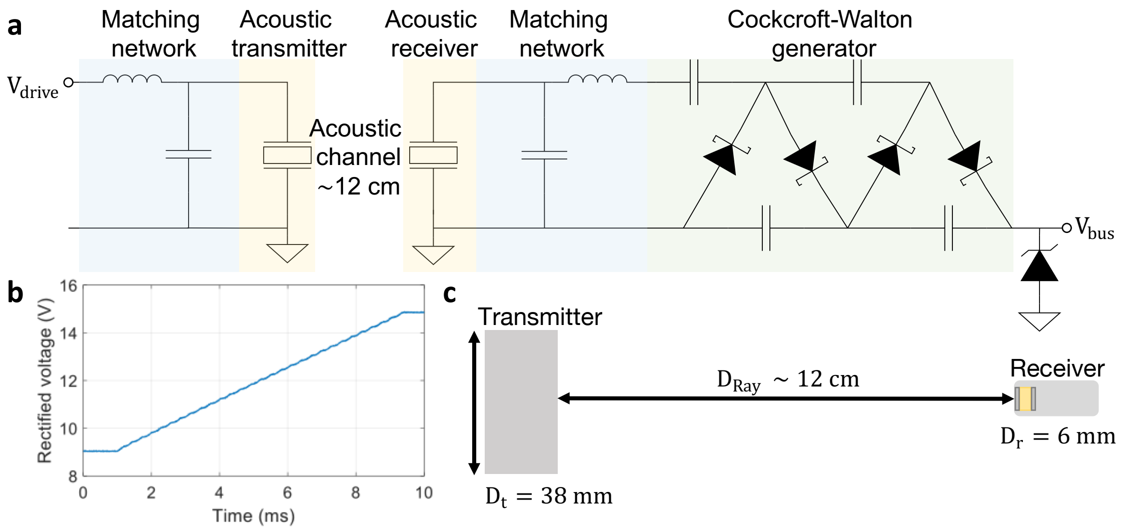

Figure 4.3. Acoustic power transfer for wireless photoacoustic tomography. **a**, Simplified circuit diagram. V_{drive} connects to a power amplifier driving the transmitter. V_{bus} connects to the capacitor bank used to power the laser diode array. **b**, Rectified voltage V_{bus} from acoustic power transfer on the capacitor bank. **c**, Schematic of the transmitter and receiver geometry.

Wireless triggering

To control laser firing and to synchronize with photoacoustic detection, we use low-latency wireless triggering. Alternatively, an independent trigger source could be included inside the device, which is synchronized to the external detection circuitry. However, this may lead to drift over time and would not provide flexibility in the repetition rate used during acquisition. For low-latency triggering, an energy source with high propagation speeds and low loss in tissues is desirable.

We transmit a broadband electromagnetic pulse using a fast-rise-time electrical pulse (Olympus 5073PR) connected to a water-immersed dipole antenna. The rise time is approximately 2 ns, corresponding to pulse frequency content up to several hundred MHz. In this frequency range, electromagnetic waves exhibit moderate attenuation in aqueous and biological media, enabling penetration that is sufficient for the dimensions relevant to the gastrointestinal tract. The transmitted signals are detected using a conformal helical antenna surrounding the device operating in broadside mode. While a resonant antenna could be more efficient, the varying dielectric properties throughout the GI tract may unexpectedly alter the antenna behavior due to dielectric loading.

Since the trigger input is high impedance, the received energy can be small while generating reasonable voltages. The antenna is connected to a full-wave rectifier constructed using ultrafast diodes (SMS7621). A 10 kΩ pull-down resistor is placed at the output terminal to shorten the rise times associated with the internal capacitance of the diodes. The rectifier output then connects to a monostable multivibrator circuit to generate pulses of consistent duration. The resistor and capacitor values are chosen to generate ~0.6 μs pulses for triggering the laser diodes through the gate driver. An example wirelessly-generated pulse is shown in Figure 4.4. This module also contains a low-dropout voltage regulator to obtain a 5 V source from the 15 V obtained from acoustic power transfer.

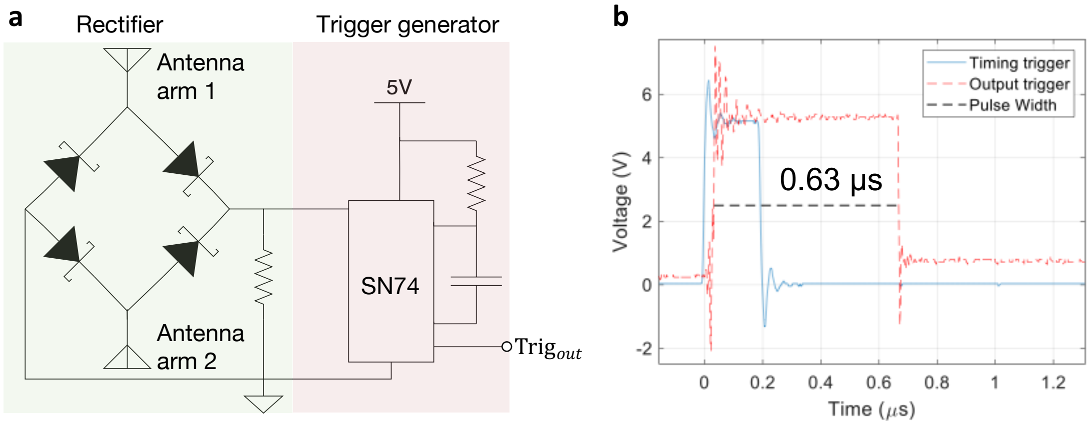

Figure 4.4. Wireless triggering circuit. **a**, Simplified circuit diagram. SN74: monostable multivibrator integrated circuit. The pulse duration is fixed by the RC values used in the trigger generator circuit. **b**, Recorded wirelessly triggered pulse.

Results

The device is housed in a 3D-printed capsule with a PDMS window on the front and rear surfaces. PDMS is used to provide a protective barrier that could survive the GI tract without substantially attenuating acoustic or optical energy. The receiving ultrasonic transducer is wired to the matching network, which then connects to the acoustic rectifier PCB. The two arms of the helical antenna are connected to the triggering PCB. Prior to encapsulation, each circuit is mounted using a 3D-printed holder. The three PCBs are connected mechanically and electrically using four lines: ground, 5 V, 15 V, and trigger.

The acoustically powered and electromagnetically triggered WPAT device is shown in Figure 4.5, and the device operation with varying position is shown in Supplementary Video 4.1. The device is mounted on an acoustic absorber to reduce reverberation in the water tank. These images were recorded using a scientific camera (FLIR GS3-U3-23S6M). Note that the camera’s sensitivity at 905 nm is ~10 times weaker than at visible wavelengths.

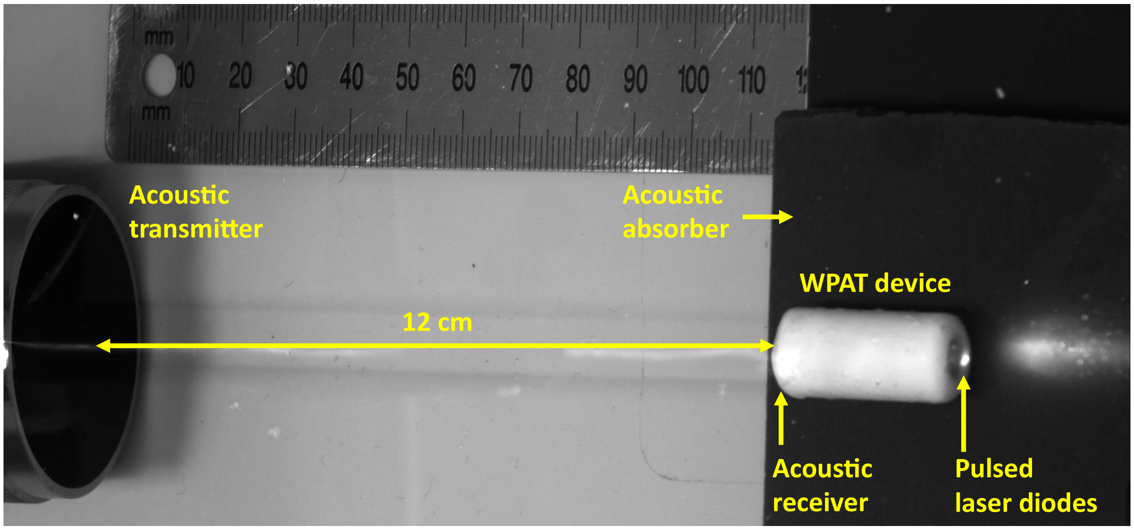

Figure 4.5. WPAT device operation with acoustic power transfer through 12 cm of water.

The system timing diagram for imaging is shown in Figure 4.6a. First, acoustic power transfer is performed over 8 milliseconds, charging the laser module capacitor banks. Due to the high acoustic intensity used for device powering and the low acoustic attenuation at 500 kHz, we use a 10 ms gap to allow the acoustic powering signals to decay so that they do not dominate the weak photoacoustic signals. Note that this time could likely be reduced in human tissue due to greater attenuation and scattering. The resulting photoacoustic signals are recorded using the custom 512-element, 60 cm diameter array described in [117]. Following detection, the next acoustic charging cycle begins. This results in an acoustic powering duty cycle of 40%, corresponding to an $I_{SPTA} \sim 590$ mW/cm^2.

We demonstrate this approach by imaging a target while performing acoustic power transfer through a 12 cm thick 4% agar phantom, which we use as a test scenario for human GI imaging applications. We scan the transmitter and WPAT device laterally in two dimensions (Figure 4.6b) in 4 mm steps. At each position, we average the photoacoustic response from 2000 laser shots. We then apply a notch filter at 500 kHz on the recorded signals to reduce remaining reverberation from acoustic powering. The PAT images from each device position are reconstructed, and a 6 mm Gaussian window is used to isolate photoacoustic signals from the local optical excitation. We scan 45 positions to construct a cm-scale target image (Figure 4.6d). We emphasize that despite the very weak optical pulse energy (130 μJ) and human-scale distances from the acoustic transmitter and photoacoustic receivers we can generate PAT images using an entirely wireless device in a small form factor.

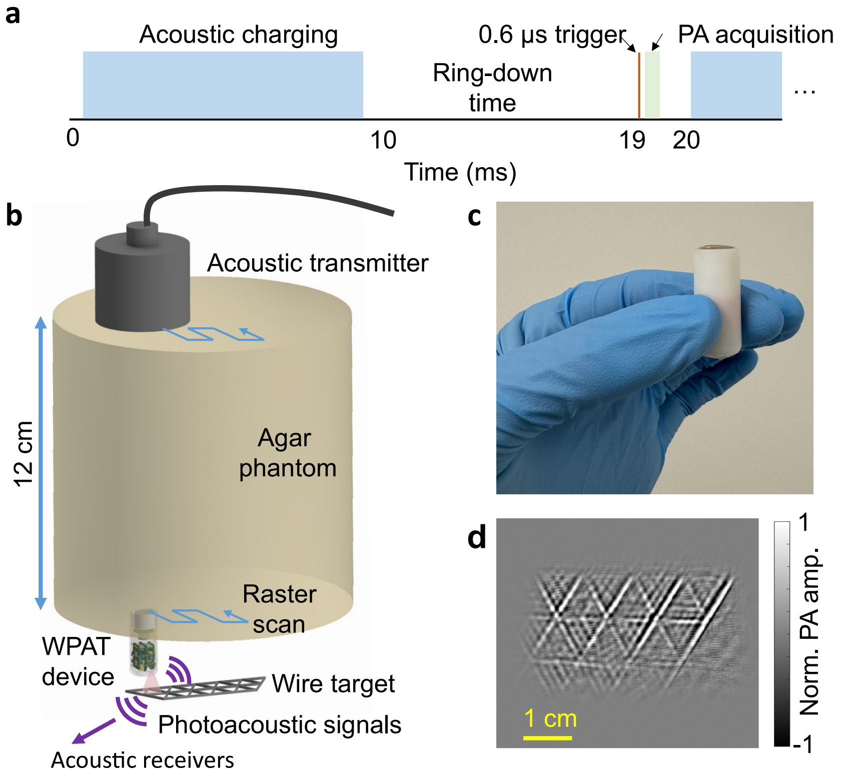

Figure 4.6. Experimental configuration and results for WPAT phantom imaging. **a**, Timing diagram for acoustically powering the device and recording PA signals. **b**, Experimental configuration for imaging through a 12 cm phantom. **c**, Assembled device. **d**, Example generated PAT image.

Discussion

We have demonstrated wireless PAT at clinically relevant depths using a wirelessly powered and triggered device in an ingestible form factor. This technology may enable imaging through mucosal layers in the entire GI tract, which is not possible with any existing approach. Acoustic power transfer eliminates the need for onboard batteries, which could enable prolonged continuous imaging during natural transit through the GI tract. In the future, large animal studies will be important to evaluate WPAT's clinical utility, including the detection of inflammatory lesions in Crohn's disease or the characterization of submucosal tumors.

A remaining challenge for clinical translation is the potential presence of air pockets in parts of the GI tract, which could impede both acoustic power transfer and photoacoustic signal detection. While the small intestine is generally filled with fluid [127], the stomach and large intestine often contain larger volumes of air. Patient preparation protocols may therefore be necessary to reduce acoustic shadowing. Additionally, although we employed a single-element transmitter for wireless powering, heterogeneous abdominal tissue may require adaptive beamforming to efficiently deliver acoustic energy to the device. Our experiment also assumes a known device location, but in the realistic GI tract the device will change position and orientation during transit. Robust localization strategies using, for instance, magnetic fields [128], [129], electromagnetic waves [130], or ultrasound imaging could enable real-time device tracking for optimal acoustic beam steering to power the device.

Since image acquisition is performed over several seconds, motion artifacts *in vivo* will need to be accounted for. Conformal ultrasound arrays [131], which may become commercially available in the future, could be wrapped around the waist to enable continuous imaging and device powering throughout the GI tract. While these could compensate for bulk patient motion, differential movement between the skin and abdominal organs must also be considered. Several additional features of this device could be optimized for GI imaging. For example, in conventional CE, side-viewing optics from the device may provide more clinically useful images than forward-looking views [132]. Future WPAT designs could therefore incorporate lateral optical illumination to better image structures perpendicular to the axis of transit.

Other mechanisms, such as sonoluminescence [133], [134] or microwave-driven plasma, can also convert other forms of energy into optical emission, but they face key limitations for biomedical use. The acoustic pressures required to generate sonoluminescence far exceed human safety thresholds, and the resulting optical source would be accompanied by strong nonlinear acoustic responses that could mask the weak photoacoustic signals. Similarly, generating microwave-induced plasma would require high electric field amplitudes and specialized gas environments that are likely infeasible for human use.

Future WPAT implementations could incorporate an onboard acoustic receiver to detect photoacoustic signals closer to the source. Local detection would allow the use of higher frequency ultrasound, improving spatial resolution with reduced attenuation and aberration through tissue. However, integrating front-end amplification and digitization would substantially increase the device's power requirements compared with the external photoacoustic detection demonstrated here. As an alternative, passive readout methods such as radiofrequency [135] or magnetoelectric [136] backscatter links may enable the transmission of encoded acoustic information without requiring high-power electronics in the capsule.

Supplementary Information

Sensitivity analysis

The optical energy of $\sim 130\ \mu\mathrm{J}$ used here is far lower than that in typical PAT systems, but we illuminate a narrower region near the laser. Here, we theoretically estimate the SNR of this system. While the fluence in this system depends on the target distance from the laser surface, we approximate it here as $F \sim 130\ \mu\mathrm{J/cm}^2$. For our pulse width of $\Delta t = 0.6\ \mu\mathrm{s}$, photoacoustic stress confinement is valid for imaging absorbers with characteristic size $d > \Delta t c_s \sim 0.9\ \mathrm{mm}$, where $c_s \sim 1540\ \mathrm{m/s}$ is the speed of sound in tissue. The resulting initial photoacoustic pressure is $p_0 = \Gamma \mu_a F$ [88]. For tissue, we consider $\mu_a \sim 0.1\ \mathrm{cm}^{-1}$, and for the wire target we approximate $\mu_a \sim 2.0\ \mathrm{cm}^{-1}$. The Grüneisen coefficient Γ is ~ 0.2 (dimensionless). This results in an initial pressure $p_{0,\mathrm{tissue}} \sim 2.6\ \mathrm{Pa}$ and $p_{0,\mathrm{wire}} \sim 52\ \mathrm{Pa}$.

We then compare this pressure with the noise-equivalent pressure (NEP) of our system [137]. We consider an NEP spectral density of $0.5\ \mathrm{mPa\ Hz}^{-1/2}$ of each acoustic receiver element [138], corresponding to NEP_0 as 0.5 Pa over a 1 MHz bandwidth. The NEP of a single recorded receiver channel $\mathrm{NEP}_{\mathrm{sig}}$ can be estimated by averaging over the number of shots N_{avg} and by scaling the NEP from the receiver surface to the target location r. In our human-scale system, $r \sim$ 30 cm. We consider the acoustic wavelength at 1 MHz, and our experiments used $N_{\mathrm{avg}} = 2000$.

$$\mathrm{NEP}_{\mathrm{sig}} = \mathrm{NEP}_0 \frac{r/\lambda}{\sqrt{\mathrm{N}_{\mathrm{avg}}}} \sim 2.2\ \mathrm{Pa} \tag{4.1}$$

This would result in a signal-to-noise ratio (SNR) of $p_{0,\mathrm{wire}}/\mathrm{NEP}_{\mathrm{sig}} {\sim} 24$. In the recorded signals shown in Figure 4.7, we observe an SNR of approximately 27. Note that these signals were notch filtered at 500 kHz to remove residual signals from acoustic power transfer, but some ringing remains.

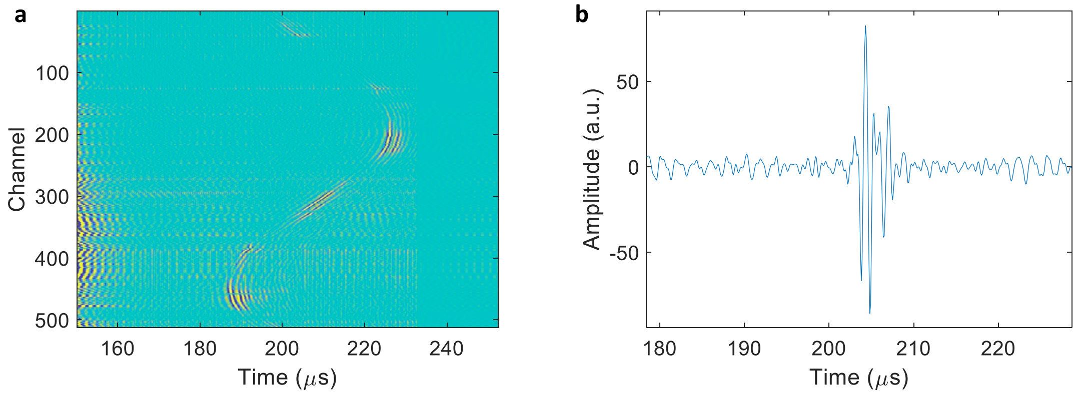

Figure 4.7. Example recorded signals using WPAT excitation. **a**, Recorded sinogram across all 512 channels after notch filtering the 500 kHz acoustic power transfer signal. **b**, Example signal on channel 310.

The resulting NEP of the entire imaging system can be estimated [138] by also averaging over the receiver element count $N_{\mathrm{ele}} = 512$. The resulting imaging $\mathrm{NEP}_{\mathrm{img}}$ is estimated as

$$\mathrm{NEP_{img}} = \mathrm{NEP_0}\frac{r/\lambda}{\sqrt{N_{\mathrm{avg}}}\sqrt{N_{\mathrm{ele}}}} \sim 0.1\ \mathrm{Pa} \tag{4.2}$$

In realistic tissues with $\mu_a \sim 0.1\ \mathrm{cm^{-1}}$, we expect the resulting image SNR to be approximately:

$$\mathrm{SNR_{img}} = \frac{p_{0,\mathrm{tissue}}}{\mathrm{NEP_{img}}} \sim 26 \tag{4.3}$$

Image generation

We raster-scanned the WPAT device to generate a cm-scale image of a wire target. For each position, we reconstruct the photoacoustic image. We apply a Gaussian window with $\sigma = 6$ mm centered at the device position to isolate the illuminated imaging region while minimizing the inclusion of image noise. An example window and image for a single position is shown in Figure 4.8. The final image is the sum of the images from all 50 positions, shown in Supplementary Video 4.2.

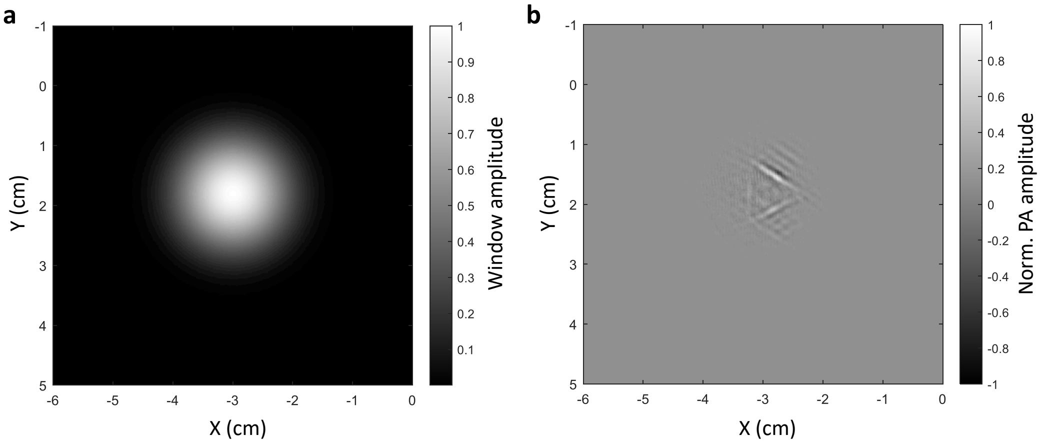

Figure 4.8. Example image from a single device location during raster-scanning. **a**, Gaussian window used to isolate the illuminated region. **b**, Photoacoustic image after applying the Gaussian window. The final image is generated by summing the windowed images from all device positions.

Acoustic power transfer

We use a flat 1.5-inch diameter transmitter to power the WPAT device. This geometry corresponds to a Rayleigh length of ~12 cm. Compared with focused transmitters, flat ones provide a more uniform focal region with reduced positioning precision requirements. The simulated beam profile of this transducer is shown in Figure 4.9.

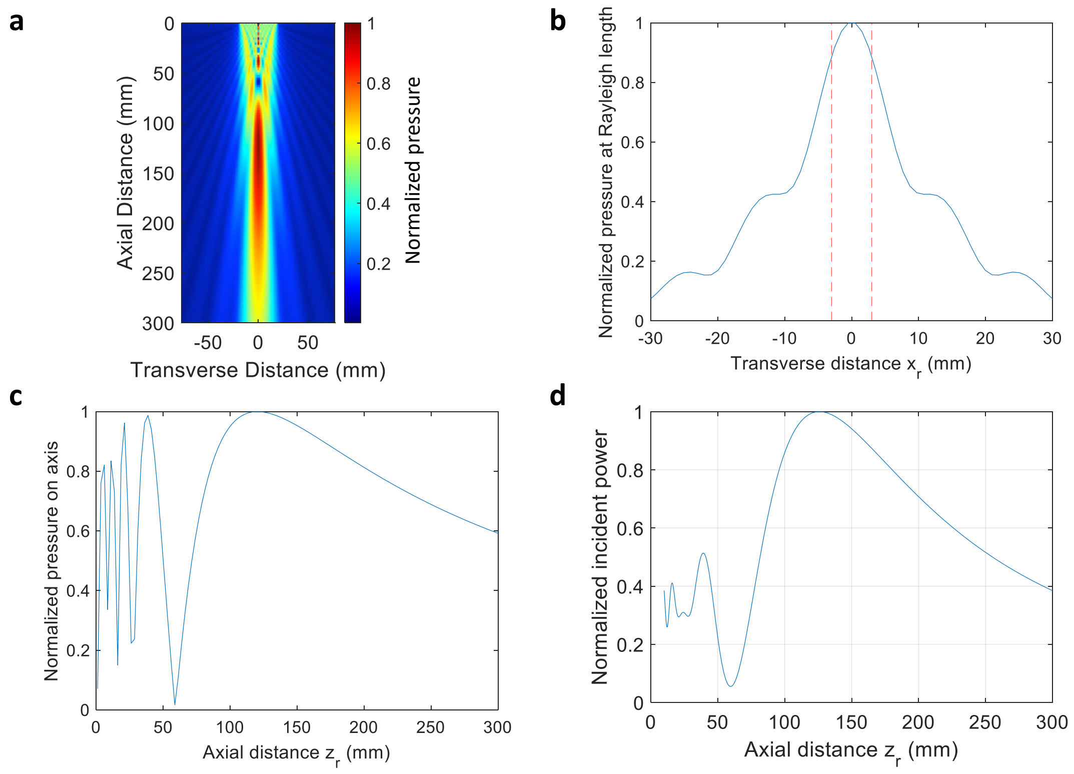

Figure 4.9. Simulated acoustic beam profile for acoustic power transfer. **a**, Simulated beam profile for the transmitter. **b**, Transverse profile of the normalized pressure at the Rayleigh length of 12 cm. The red-dashed lines indicate the diameter of the receiving transducer. **c**, Simulated on-axis normalized pressure. **d**, Simulated on-axis power transferred to a receiving 6 mm diameter element.

Figure 4.9d also shows the simulated on-axis normalized power transfer between the transmitting element and the 6 mm diameter receiver. Note that 80% of peak power transfer is maintained over a ~8 cm axial distance, which relaxes positioning accuracy requirements in our experiments.

We show the rectified DC voltage from acoustic power transfer to the capacitor bank in Figure 4.10. Laser firing causes a sharp drop in voltage from ~15 V to 9 V, corresponding to an energy of $E_{LD} = \frac{1}{2}C\left(V_i^2 - V_f^2\right) \sim 324$ μJ. Note that this example is shown for 100 Hz laser repetition rate.

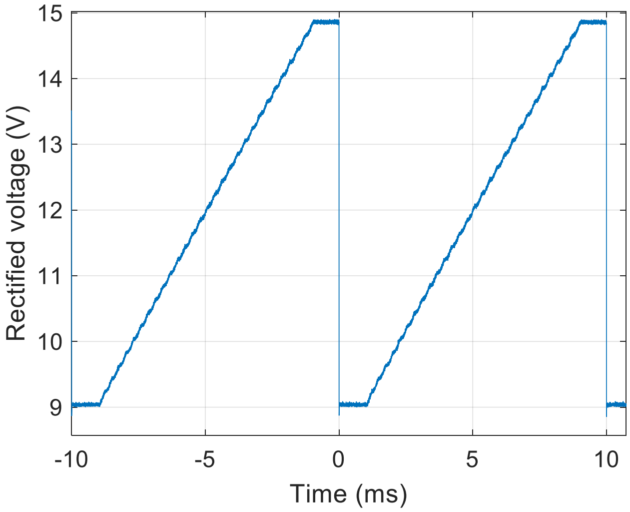

Figure 4.10. Example rectified voltage from the acoustic receiver to the capacitor bank used to energize the pulsed laser diode array. The laser is fired here every 10 ms.

We estimate the efficiency of the receiver transducer based on the open-circuit recorded voltage and the incident pressure on the receiver surface. We used a hydrophone to record the incident peak pressure as $p_{\mathrm{pk}} \sim 145\ \mathrm{kPa}$ using a representative continuous-wave transmitter power. The available power at the receiver, assuming a uniform pressure distribution over the small receiver area A, is therefore

$$P_{\mathrm{avail}} = \frac{\left(p_{\mathrm{pk}}\right)^2}{2Z_a} A \approx 198\ \mathrm{mW}. \tag{4.4}$$

We then recorded the open-circuit voltage from the receiver as $V_{\mathrm{oc}} \sim 30$ V, resulting in an estimated received power of

$$P_{\mathrm{rx}} = \frac{(V_{\mathrm{oc}})^2}{8\mathrm{Re}\{Z_{\mathrm{out}}\}} \approx 50\ \mathrm{mW}, \tag{4.5}$$

where $\mathrm{Re}\{Z_{\mathrm{out}}\} \sim 2.54\ \mathrm{k\Omega}$ is the real part of the receiver output impedance. This results in an estimated transducer efficiency of

$$\eta = \frac{P_{rx}}{P_{avail}} \approx 26\ \% \tag{4.6}$$

We compare this with the KLM model [139] for PZT-5A, using $g_{33} \sim 0.025\ \mathrm{V \cdot m/N}$ and thickness $d = 4$ mm. The open-circuit voltage is estimated as:

$$V_{\mathrm{oc}}(\omega) = g_{33} d T_{33,\mathrm{eff}}(\omega) \tag{4.7}$$

where $T_{33,\mathrm{eff}}$ is the effective normal stress in the piezoelectric, found from the incident acoustic pressure as $T_{33,\mathrm{eff}}(\omega) = p_{\mathrm{inc}} G_{\mathrm{ac}}(\omega)$. The stress gain $G_{\mathrm{ac}}(\omega)$ accounts for the quarter-wave matching layer and mechanical resonance from the air backing. Here, the measured $V_{\mathrm{oc}} \sim 30\ \mathrm{V}$ is achieved for $G_{\mathrm{ac}}(\omega) \sim 2$, which is a modest value for an air-backed resonant transducer.

Note that after the matching circuit into the Cockcroft-Walton generator, the input voltage is lower due to the lower input impedance. Given the acoustic-to-electric efficiency from the transducer of ~26%, the required efficiency of the matching circuit and generator is ~31% to achieve a total required efficiency of 8% to meet our power requirements given the acoustic safety standards.

Device construction

Steps of the device construction are shown in Figure 4.11. The front surface of the 3D printed capsule is first coated with PDMS. The wired device, including the receiving transducer, matching network, and the three PCB modules, are then positioned into the capsule. The two arms of the antenna are connected to one of the PCBs. After insertion into the device, the rear face of the receiving transducer is also coated in a thin layer of PDMS.

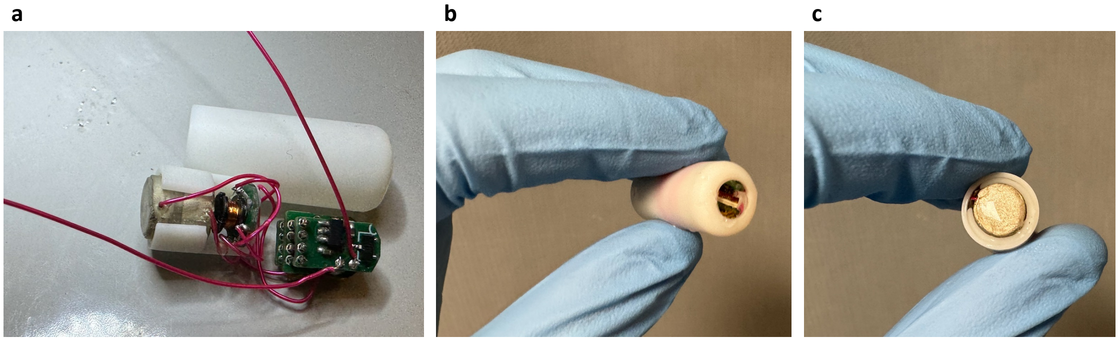

Figure 4.11. Wireless photoacoustic device construction. **a**, Wired device before inserting into the 3D-printed enclosure. **b**, Front face of the device with the laser diode array. **c**, Rear face of the device with the receiving transducer. Both faces are coated with PDMS.

CONCLUSION

Summary of Contributions

This thesis demonstrates three modalities toward human-scale medical imaging and treatment guidance: ultrasound tomography, thermoacoustic-guided microwave ablation monitoring, and ingestible-based photoacoustic tomography.

In ultrasound tomography, we achieved the first full cross-sectional imaging of human anatomy in regions like the abdomen and lower extremities. In addition to conventional backscatter imaging, we obtain quantitative maps of the speed of sound and attenuation coefficient using signals transmitted through the entire cross-section. We also developed an approach for video-rate biopsy needle guidance across a wide field-of-view. These results demonstrate that ultrasound can be used to capture clinically relevant anatomical information across the entire human cross-section.

We developed an approach for thermoacoustic-based monitoring of microwave ablation procedures, where we show that using a modulated microwave source generates detectable thermoacoustic signals with modest modification to clinical systems. Since these signals relate to the deposited thermal energy, we show that they can be used for more accurate prediction of ablation zones compared to standard look-up tables. These results suggest a pathway toward real-time guidance which could allow for more precise treatment.

We demonstrated a method to extend the imaging depth of photoacoustic tomography to 12 cm using a wireless, ingestible capsule-scale optical source. This illumination strategy overcomes the fundamental depth limitations of external photoacoustic illumination, which could enable imaging access to deep anatomical regions like the gastrointestinal tract.

Each contribution required substantial custom hardware design and construction, including a human-scale ultrasound receiver array. These modalities were experimentally demonstrated either in humans *in vivo*, in *ex vivo* tissue, or in phantoms, establishing technical feasibility and informing future efforts to clinical translation.

Limitations

While these initial efforts are promising, several limitations will need to be addressed prior to wider clinical adoption.

Water immersion coupling

All three approaches developed in this thesis rely on water immersion to achieve acoustic coupling between the transducers and tissue. While water tanks may be acceptable in some settings such as research facilities or wellness centers, clinical translation would benefit from dry-coupling or gel-based methods, particularly for intraoperative or bedside applications where water immersion is impractical.

Acoustic heterogeneity and shadowing

Clinical ultrasonography typically assumes uniform acoustic tissue properties, but this assumption breaks down at human scales where bone and air create regions of near-zero acoustic transmission. Specific patient preparation protocols may help in reducing gastrointestinal air, but this limitation will need to be addressed in all three modalities. Additionally, speed of sound variation between tissues introduces reconstruction artifacts. Advanced methods like eikonal solvers of full-waveform inversion could overcome these errors by explicitly accounting for acoustic heterogeneity during image reconstruction.

Two-dimensional imaging

Our current acoustic detection system allows for 2D images with mm-scale in-plane resolution but coarse elevational resolution. While sufficient to visualize broad anatomical structures, this could limit detection of small features such as early-stage tumors which would benefit from isotropic 3D imaging. TA-guided microwave ablation would also benefit from capturing 3D distributions of the thermal deposition to improve modelling accuracy. Full 3D imaging could be achieved using vertical scanning of high-NA focused detectors or using large 2D detector arrays. However, such arrays remain prohibitively costly, and their implementation would require advances in both hardware and computational methods.

Future Outlook

Translating these techniques into clinical practice will require further technical development, validation through experimental trials, regulatory approval pathways, and clinical studies to identify optimal applications within existing healthcare workflows. Here, we explore future trajectories for these technologies and how they may fit within broader healthcare systems.

Enabling technologies

Several current technological trends could accelerate the performance and adoption of these modalities. Advances in computational hardware, particularly GPU architectures and emerging chips combined with improved algorithms, could enable practical reconstruction techniques like full-waveform inversion for whole-body ultrasound tomography, which currently requires prohibitive numbers of forward simulations over large imaging domains. These advances could also allow for automated image analysis, particularly if a large dataset over wide populations is obtained. On-chip [140] and skin-conformal [141] ultrasound array technologies could enable lower-cost and more convenient imaging systems suitable for point-of-care settings or guidance during clinical procedures. In photoacoustic imaging, high-power laser diodes under development for automotive LiDAR applications could allow for compact, affordable excitation sources for ingestible photoacoustic probes.

Toward longitudinal diagnostic imaging

The recent advent of direct-to-consumer "commodity care" services [11] like on-demand whole-body MRI screening have generated controversy within the medical community. Critics emphasize the risks of false-positive findings and clinically insignificant incidental discoveries, which can cascade into unnecessary procedures, patient anxiety, and healthcare costs without commensurate health benefits. However, this debate largely assumes the conventional model of single-timepoint diagnostic imaging, which provides only a static snapshot of anatomical state.

The modalities presented in this thesis, if deployed at sufficient convenience and cost-effectiveness, could enable a different approach: longitudinal monitoring at frequent intervals (daily to monthly). Time-resolved imaging could transform the clinical significance of incidental findings. For example, a small nodule or lesion carries different implications depending on whether it remains stable, grows linearly, or shows accelerating expansion. Current practice often defaults to invasive biopsy or prolonged waiting with infrequent follow-up imaging due to cost, radiation exposure, or availability. Frequent, non-invasive monitoring could allow growth kinetics to be observed rather than inferred from sparse timepoints. This shift from occasional snapshots to regular imaging could improve early detection of malignant transformation, reduce unnecessary biopsies of stable lesions, and enable personalized screening intervals based on individual risk trajectories.

A more accessible entry point for longitudinal imaging could be in wellness monitoring rather than disease detection. Frequent imaging of muscle and adipose tissue distribution could provide objective feedback for fitness interventions, nutritional programs, or sarcopenia screening in aging populations, enabled by the absence of ionizing radiation and low per-scan cost. Such wellness-focused use cases could establish the infrastructure and user acceptance needed for eventual expansion into clinical workflows.

APPENDIX A: CUSTOM SYSTEM HARDWARE

Ultrasonic receiver array

Like early ultrasound systems, we use water immersion for acoustic coupling between the transducers and tissue. We developed a custom 512-element, 60 cm diameter acoustic receiver array with a 1 MHz center frequency. This geometry is scaled from similar systems for small animal or human breast photoacoustic imaging [142], [143]. We use lower acoustic frequencies than typical handheld probes or breast UST systems to enable whole cross-sectional imaging. For instance, the typical acoustic attenuation of ~1 $\mathrm{dB \cdot cm^{-1} \cdot MHz^{-1}}$ results in ~30 dB attenuation across a typical 30 cm diameter human cross-section at 1 MHz [36]. Each channel connects to a preamplifier on annular printed circuit boards (PCBs). We also considered using light-based acoustic sensors (see Appendix B), but these remain impractical for large channel counts and do not necessarily provide sensitivity improvements over larger-sized piezoelectric sensors. We show the steps of the receiver array construction in Figure A.1.

All 512 receiver array elements are 1 mm thick, 3 mm × 10 mm gold-coated piezoelectric polymer (PVDF-TrFE, PolyK Technologies LLC). We selected PVDF-TrFE for its broad bandwidth and ease of manufacturing. Its acoustic impedance (~4.2 MRayl) is also more closely matched to casting epoxy backings (~3.5 MRayl) and water (~1.5 MRayl) than other piezoelectric materials. Each element is capacitively coupled to copper-clad polyimide electrodes by bonding with high-strength epoxy. A continuous copper-clad polyimide electrode is used for ground reference. The electrodes are then directly connected to parallel preamplifiers implemented on custom annular printed circuit boards. The preamplifiers provide 15 dB voltage gain with 100 kΩ input impedance. Further construction details are shown in Figure A.1 and Figure A.2.

We machined a 60 cm diameter plastic disc and used it as a mold for the inner surface of the array. The elements and preamplifiers are housed in a stainless-steel shielded enclosure, with coaxial cables for each element connected through stainless steel holding tubes.

Casting epoxy serves as the backing material for each element, and we incorporate an angled back panel to reduce acoustic reverberation. All channels are low-pass filtered ($f_c =$ 2 MHz) and digitized (Photosound Legion) in parallel at 5 MSPS using 20 dB additional gain. The digitizers are controlled and transfer data through USB over optical fiber to reduce interference. The preamplifiers are powered by rechargeable lithium-polymer batteries, which feature a DC voltage regulator to minimize electrical noise. To account for geometrical error during manufacturing, the technique described in [144] are used to calibrate each element's position.

Strips of 128 channels were then mounted into the plastic supports and positioned around a 60 cm diameter lathed disc of high-density polyethylene to provide a precise template surface geometry. The backing was then filled with casting epoxy. Next, the preamplifier PCBs were mounted, and each electrode trace was soldered to its amplifier channel. Every ~10 channels, a short wire was also soldered to the reference (front) electrode. Signal coaxial cables for each channel and DC power cables extend down the supporting tubes and connect to the PCBs. The other sides of the cables connect to the DAQs using Acuson-style connectors mounted to custom low-pass filter PCBs. We then lowered the top stainless-steel plate and trimmed the front electrode to the plate height. Finally, we glued a stainless-steel shim with silver epoxy to the exterior surface of the array to provide electrical shielding.

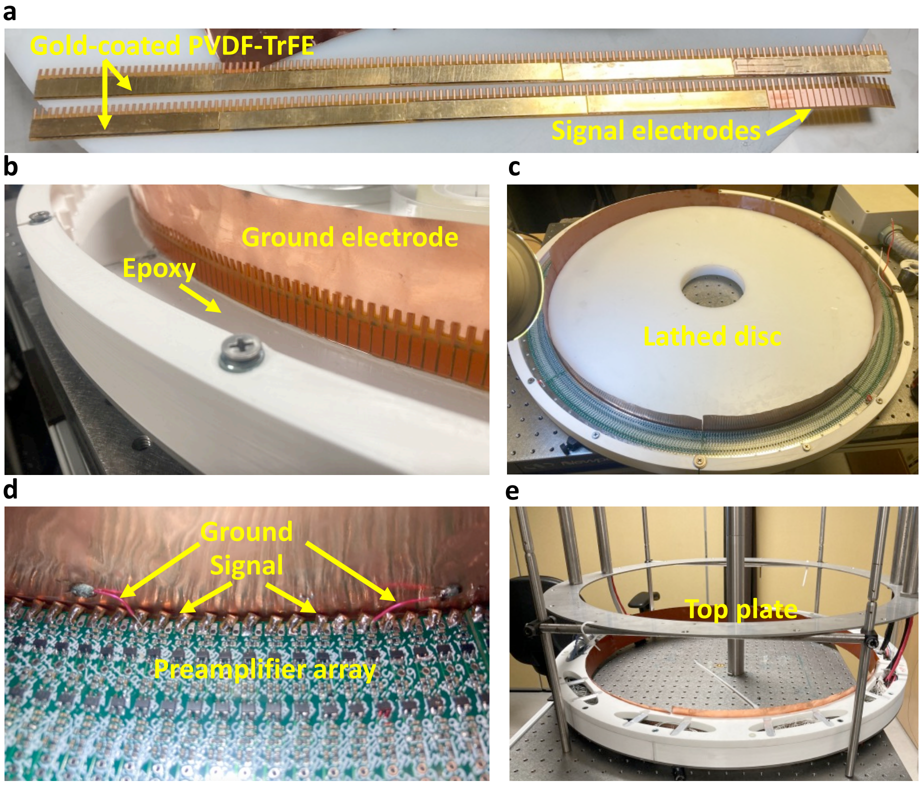

Figure A.1. Steps of the acoustic receiver array construction. **a**, Diced PVDF-TrFE is glued to polyimide electrodes and a continuous common electrode. **b**, Sections of channels are mounted to a circular template. A casting epoxy backing is poured. **c**, Annular preamplifier PCBs are mounted on top of each section, and the electrodes are soldered to them. **d**, A grounding wire is soldered every ~10 channels. **e**, The outer electrode is trimmed, the array is filled with casting epoxy, and the top stainless steel plate is screwed in.

The constructed array is shown in Figure A.2a positioned in the water immersion tank. For ultrasound imaging (Chapters 2 and 3), we use a separate single-element transmitter which rotates around the target using a gear attached to the array. For thermoacoustic (Chapter 3) and photoacoustic (Chapter 4) imaging, a separate microwave or optical source is used. Figure A.2b shows a cross-section of the array interior. An angled plastic support is positioned in the transducer backing to reduce acoustic reverberation. The gear rotation is driven by a stepper motor. An optical homing switch is used to ensure a consistent initial rotation angle. Plastic hooks are mounted on the gear to hold the transmitter cable on the gear surface during rotation (Supplementary Video A.1).

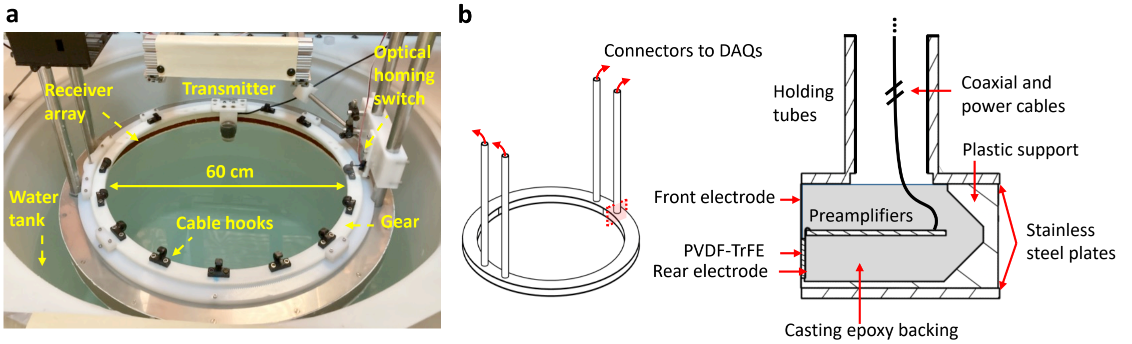

Figure A.2. Human-scale, ultrasound-based imaging hardware. **a**, System photograph. **b**, Acoustic receiver array design, showing a cross-section of the array. DAQs: data acquisition modules.

<u>Acoustic receiver characterization</u>

The bandwidth of the array elements was evaluated using a photoacoustic point source made from carbon powder-epoxy mixture on the tip of an optical fiber (Thorlabs FT600EMT) of 600 µm core size. We used a sampling rate of 20 Msamples per second to record the bandwidth up to 10 MHz. We show the frequency response of the array elements in Figure A.3. The average –3 dB bandwidth across the array is approximately 0.81 MHz (corresponding to 81% fractional bandwidth).

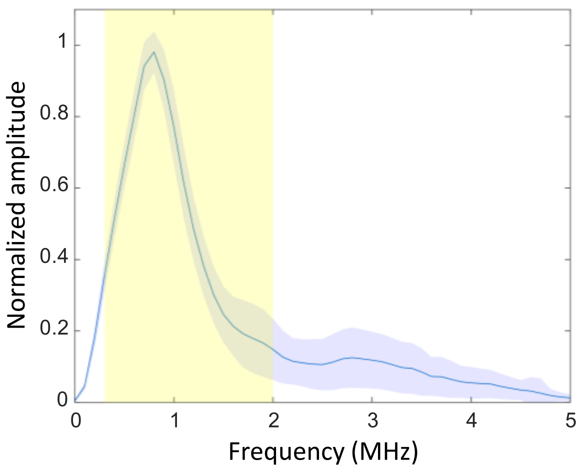

Figure A.3. Normalized frequency response the receiver array. The solid curve indicates the mean response across 512 elements. The blue shaded area indicates one standard deviation from the mean response. The yellow shaded area indicates the frequency range of 0.3 – 2 MHz of the imaging chirp signal.

Imaging system construction

We constructed the primary structure of our system using 1.5-inch aluminum T-slots. A high-density polyethylene plate was water jet cut with openings for the water tank and linear stages. An aluminum plate was water jet cut and mounted on the entry side of the tank, and an anti-slip polyurethane mat was adhered on its surface. A dock ladder is mounted to the aluminum plate with handrails and anti-slip steps for safe entry into the immersion tank.

The larger gear was water jet cut from acetal with 23.5-inch outer diameter and 564 gear teeth. This gear was positioned in an ultra-high molecular weight polyethylene mount with a lathed rotational surface. The mount was screwed to the top plate of the acoustic receiver array. We used an 18-tooth brass pinion gear to drive the larger gear's rotation, coupled using a rotary shaft to a stepper motor. The resulting gear ratio is ~31.3. The gear is held into the mount using plastic pieces screwed into the gear mount. The transmitter is held to the gear using a magnetic mount for free release in case of obstruction by the volunteer.

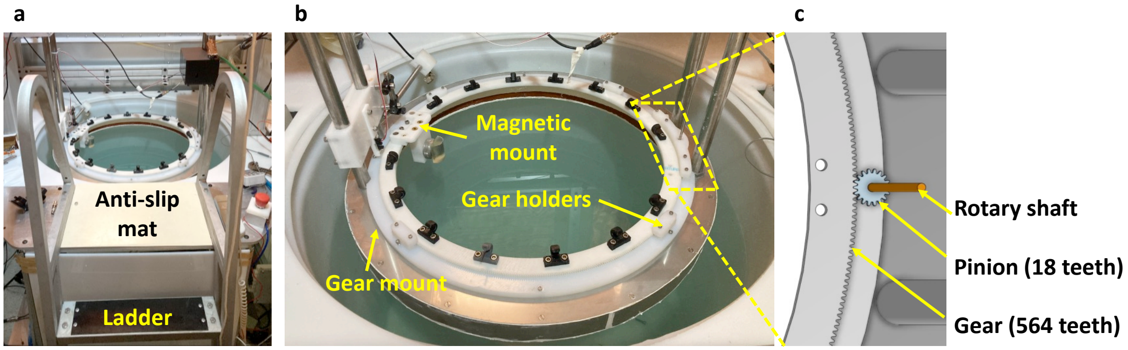

Figure A.4. Additional details of the human-scale imaging system construction. **a**, Immersion tank entry using a ladder with handrails and an anti-slip mat. **b**, Top side of the receiver array, showing the gear and its mount and holding pieces. **c**, Model of the gear driver, with the rotary shaft connected to a stepper motor.

To avoid water immersion in the future, we plan to adapt our system using filled water membranes that couple acoustic signals between the array elements and the skin. We show an example configuration in Figure A.5. Elastic membranes could accommodate a variety of body sizes using different amounts of filled water. Ultrasound gel on the skin surface may further improve acoustic coupling.

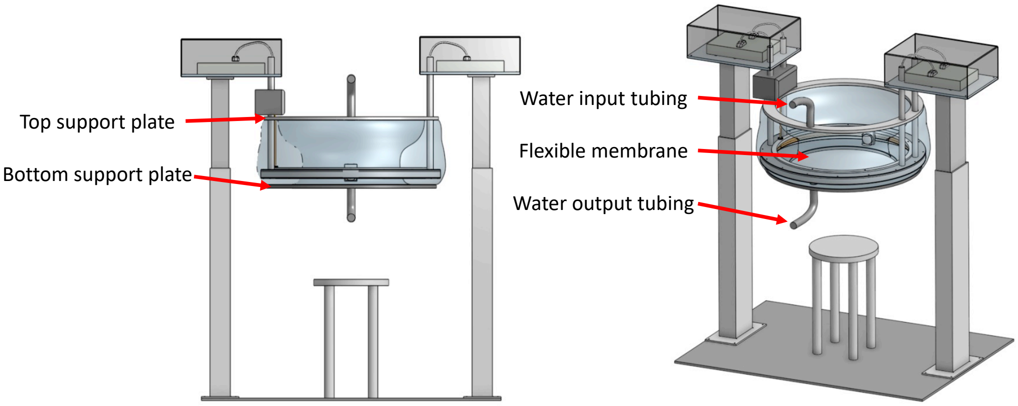

Figure A.5. Potential adaptation of our system to enable immersion-free abdominal imaging.

APPENDIX B: ACOUSTIC SENSING WITH LIGHT

Garrett, David C., and Lihong V. Wang. "Acoustic sensing with light." In: *Nature Photonics News & Views* 15, no. 5 (2021): 324-326.

Optical acoustic sensors have gained interest for use in photoacoustic imaging systems, but can they dethrone conventional piezoelectric sensors altogether?

Photoacoustic tomography (PAT) is a hybrid biomedical imaging modality which provides the molecular contrast of light at depths enabled by acoustic sensing. As PAT pushes the frontier to deeper and higher-resolution imaging, there is a growing demand for a new generation of sensitive and scalable broadband acoustic sensors. Optical acoustic sensors have been considered for decades [145] owing to their broad bandwidths and nearly area-independent sensitivity. Despite these desirable traits, they have not yet superseded conventional piezoelectric transducers in PAT due to practical challenges such as scalability, integration, availability, and unclear sensitivity advantages in typical use-cases.

Writing in *Nature Photonics*, Wouter Westerveld and co-authors demonstrate an acoustic sensor [146] which overcomes many of these limitations. Their acoustically point-like (15-20 μm) sensor employs an optomechanical waveguide to enable high sensitivity and bandwidth. Benefitting from existing semiconductor infrastructure, the sensor is conveniently compatible with complimentary metal–oxide semiconductor (CMOS) processing where fine pitch arrays with parallel readout were demonstrated. With these milestones, optical acoustic sensors are expected to become more widely adopted in PAT. Nevertheless, practitioners should consider the sensitivity advantages over the piezoelectric transducers for a given application.

Piezoelectric transducers remain the most used acoustic sensors in PAT systems. While PAT involves only acoustic sensing, piezoelectric transducers are reciprocal devices capable of transmission, which is required when concurrent ultrasonography is desired. Combined with inherent mechanical and electrical losses, transducer sensitivity can be shown to degrade proportionally to the square root of sensing area [147], limiting the use of very small sensors. Conversely, optical acoustic sensors are receive-only devices and can achieve nearly area-independent sensitivity in sensor dimensions comparable with optical wavelengths.

In optical acoustic sensors, acoustic displacement modulates the optical path length in the interaction region of a device by altering either its geometric length or refractive index [148]. Changes in the optical path length can be sensed using interferometry with respect to a reference arm (e.g. Michelson or Mach-Zehnder [145]), or by detecting changes in the optical transmission through a resonant structure (e.g. micro-ring [149] or membrane resonators [150]) at a given optical wavelength. High optical quality factor on the order of 10,000 and coherent light sources are generally needed to sense acoustic displacements which are much smaller than the optical wavelength [145]. For instance, a representative incident pressure of 10 Pa at 10 MHz leads to only 100 fm of acoustic displacement in water. The device by Westerveld et al. employs an optomechanical waveguide ring resonator with a tiny 15 nm air gap, whereby slight displacement in the top membrane induces refractive index changes which alter the resonant wavelength [146]. Using light at the flank of resonance, incident acoustic signals thereby translate to optical intensity modulation detectable with high sensitivity and bandwidth.

Despite their advantages, optical sensors have not yet been widely adopted in PAT systems. One challenge is multiplexing sensor arrays, where manufacturing tolerances can lead to different optical properties in the interaction region [151], and dedicated lasers and optical detectors are often impractical. Westerveld and colleagues address this issue by fabricating arrays of slightly different sized optical resonators, allowing parallel optical readout of several sensors on a single fiber using wavelength-division multiplexing. Prohibitive costs, set-up time, and stability have also generally restricted optical sensors to the laboratories of their developers. The developments by Westerveld et al. provide a step towards more widespread adoption of optical acoustic sensors aided by the scalability of CMOS processing. On-chip laser integration remains an ongoing challenge in silicon photonics more broadly [152], but if solved would further improve the scalability of such sensors.

When evaluating sensors, one key metric for characterizing acoustic sensitivity is the noise-equivalent pressure density (NEPD), defined in amplitude spectral density $[\mathrm{Pa} \cdot \mathrm{Hz}^{-1/2}]$. For a given bandwidth, NEPD can be converted to noise-equivalent pressure (NEP) [Pa]. NEP calibrates the system noise into an effective pressure incident on the sensor surface which can be compared with incident photoacoustic signal pressure. NEPD therefore provides a convenient benchmark of noise-limited detection across sensor architectures.

Acoustic thermal noise of the medium presents a baseline noise in all sensor types. In piezoelectric sensors, additional contributions come from thermal noise in the transducer and amplifier noise. The resulting NEPD can be found for broadband transducers as [147]

$$\mathrm{NEPD} = \sqrt{kTZ_aF_n/[A\eta]} \tag{B.1}$$

where k is Boltzmann's constant, T is absolute temperature, Z_a is the acoustic impedance of the medium, F_n is the noise figure of the amplifier, A is the active area of the transducer, and η is defined as the ratio of generated electric power to incident acoustic power.

In optical sensors, additional contributions consist of displacement and sensing noise. Displacement (or acousto-mechanical) noise causes fluctuations in the acoustic interaction region. If mechanical losses are exhibited in the interaction region, displacement noise is inherently generated according to the fluctuation-dissipation theorem. Sensing noise, limiting the detection of displacement, includes laser amplitude noise, shot noise and optical readout noise. Westerveld et al.'s recent benchmark in sensitivity (1.3 $[\mathrm{mPa} \cdot \mathrm{Hz}^{-1/2}]$) is dominated by displacement noise in 20 μm devices, where a comparably-sized piezoelectric sensor would have two orders of magnitude higher NEPD [146].

While optical acoustic sensors have far greater sensitivity than piezoelectrics per unit active area, the advantage of miniaturization should be considered from an acoustic perspective in the two variants of PAT: microscopy (PAM) and computed tomography (PACT). In PAM, larger focused piezoelectric transducers detect acoustic responses within a tight focus inside biological tissues. As an example, a transducer [147] with numerical aperture $\mathrm{NA} = 0.5; A = 30$ mm2; $T = 300$ K; $Z_a = 1.5$ MRayl; $F_n = 2; \eta = 0.001 - 0.1$ can achieve NEPD of $0.06 - 0.6$ [mPa · $\mathrm{Hz}^{-1/2}$]. Note that η is typically cited between 0.001 and 0.01 in broadband transducers [147], but values in excess of 0.1 have been reported even for fractional bandwidth of >50% [153]. As a virtual point detector with a focal radius of $0.7\ \lambda$ inside the tissue, where λ is the acoustic wavelength, NEPD scales up to $18 - 180$ [mPa · $\mathrm{Hz}^{-1/2}$] at 100 MHz, which is far greater than that of Westerveld et al.'s ptical sensor. Therefore, if invasively embedded in the focal region of interest inside the tissue, the optical sensor would achieve far greater sensitivity. A point-like sensor's effective NEPD at distance r from the point of interest scales with r/λ. Thus, at approximately 0.2 - 2 mm, the optical NEPD becomes greater than the focused piezoelectric transducer's (Figure B.1a). Focused optical sensors could therefore be promising in PAM using either lenses or reflectors but have not yet been demonstrated.

In PACT, arrays of tens to thousands of sensors typically surround the object and record acoustic responses in parallel. Image reconstruction over some field of view (FOV) is subject to the spatial Nyquist sampling criterion, whereby optimal sensor spacing and size are equivalent to a half-wavelength on the tissue surface. Sensors can be either positioned directly on the FOV boundary or extended by some distance with scaled sensor dimensions. While piezoelectric NEPD relates to the sensor area as in eq. (1), spherical acoustic waves from an object have pressure p which relates to distance r as $p \propto r^{-1}$. If the sensor area A scales with r^2, these two effects cancel and NEPD remains fixed at the value of half-wavelength sensors on the FOV boundary. Since further size and spacing reduction provides no appreciable benefit in spatial sampling [154] or element directivity, we suggest that half-wavelength sized piezoelectric transducers provide a point of comparison unless the application is inherently space-constrained (e.g. in near-field [151] or endoscopic [155] imaging).

As a simple comparison of PACT sensitivity, we again consider Westerveld et al.'s optical sensor NEPD benchmark of 1.3 [mPa · $\mathrm{Hz}^{-1/2}$] approximated as uniform across frequency [146]. While different optical sensor architectures may exhibit non-uniform NEPD, Westerveld et al.'s is one of the lowest reported regardless of size or frequency. This sensor is compared with conventional piezoelectric sensors according to eq. (1), using typical values of $T = 300$ K; $Z_a = 1.5$ MRayl; $F_n = 2; \eta = 0.001 - 0.1$. Square piezoelectric sensor dimensions are fixed to a half-wavelength at a given upper cutoff frequency. It is evident in Figure B.1b that above ~ 2.5 MHz, optical sensors generally outperform piezoelectrics in PACT sensitivity. However, piezoelectric transducers may remain appealing for lower frequencies used in human-scale imaging, where the current complexity of optical sensors may not be justified.

Westerveld et al.'s optical acoustic sensor presents a new benchmark in sensor size, sensitivity and integration. Nevertheless, when considering optical sensors for use in PACT, we suggest comparing against half-wavelength sized piezoelectric sensors since there is no acoustic benefit to them being smaller. Optical sensors have a clear benefit at higher frequencies and in space-constrained applications, but piezoelectric transducers may remain advantageous in lower frequency applications, such as human-scale imaging. Similarly, unless optical sensors can be placed directly in the imaging region, microscopy imaging will likely continue to benefit from larger focused piezoelectric transducers. Nevertheless, optical acoustic sensors like Westerveld et al.'s present great promise in advancing PAT to deeper and higher-resolution imaging, and in opening new applications as performance and integration continue to improve.

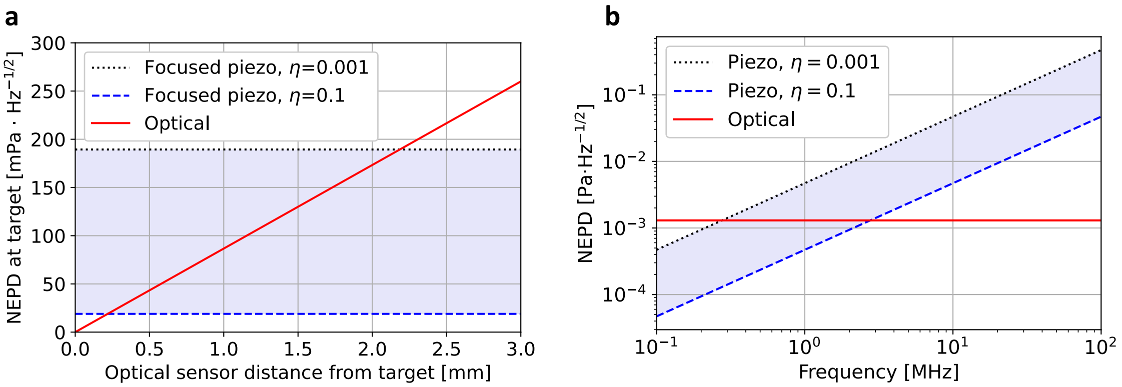

Figure B.1. Comparison of NEPD between an example optical sensor [146] and typical piezoelectric transducers in the two variants of PAT. **a**, PAM: NEPD at the target region for a point-like optical sensor at varying distance and focused piezoelectric transducers. **b**, PACT: NEPD at the surface of point-like optical and piezoelectric detectors with dimension $\lambda/2 \times \lambda/2$ at varying upper cutoff frequencies.

BIBLIOGRAPHY

[1] W. C. Röntgen, “On a New Kind of Rays (Über eine neue Art von Strahlen),” *Nature*, vol. 53, no. 1369, pp. 274–276, Jan. 1896, doi: 10.1038/053274b0.

[2] G. N. Hounsfield, “Computerized transverse axial scanning (tomography): Part 1. Description of system,” *Br. J. Radiol.*, vol. 46, no. 552, pp. 1016–1022, Dec. 1973, doi: 10.1259/0007-1285-46-552-1016.

[3] M. J. Willemink, M. Persson, A. Pourmorteza, N. J. Pelc, and D. Fleischmann, “Photon-counting CT: Technical Principles and Clinical Prospects,” *Radiology*, vol. 289, no. 2, pp. 293–312, Nov. 2018, doi: 10.1148/radiol.2018172656.

[4] K. K. Nishiyama and E. Shane, “Clinical Imaging of Bone Microarchitecture with HR-pQCT,” *Curr. Osteoporos. Rep.*, vol. 11, no. 2, pp. 147–155, Jun. 2013, doi: 10.1007/s11914-013-0142-7.

[5] R. Damadian, “Tumor Detection by Nuclear Magnetic Resonance,” *Science*, vol. 171, no. 3976, pp. 1151–1153, Mar. 1971, doi: 10.1126/science.171.3976.1151.

[6] P. C. Lauterbur, “Image Formation by Induced Local Interactions: Examples Employing Nuclear Magnetic Resonance,” *Nature*, vol. 242, no. 5394, pp. 190–191, Mar. 1973, doi: 10.1038/242190a0.

[7] P. Mansfield, “Multi-planar image formation using NMR spin echoes,” *J. Phys. C Solid State Phys.*, vol. 10, no. 3, p. L55, Feb. 1977, doi: 10.1088/0022-3719/10/3/004.

[8] M. Sarracanie, C. D. LaPierre, N. Salameh, D. E. J. Waddington, T. Witzel, and M. S. Rosen, “Low-Cost High-Performance MRI,” *Sci. Rep.*, vol. 5, no. 1, p. 15177, Oct. 2015, doi: 10.1038/srep15177.

[9] F. Reyes-Santias *et al.*, “Cost Analysis of Magnetic Resonance Imaging and Computed Tomography in Cardiology: A Case Study of a University Hospital Complex in the Euro Region,” *Healthcare*, vol. 11, no. 14, Jul. 2023, doi: 10.3390/healthcare11142084.

[10] M. Martella, J. Lenzi, and M. M. Gianino, “Diagnostic Technology: Trends of Use and Availability in a 10-Year Period (2011–2020) among Sixteen OECD Countries,” *Healthcare*, vol. 11, no. 14, p. 2078, Jul. 2023, doi: 10.3390/healthcare11142078.

[11] J. E. Neczypor, “The rise of commodity care,” *Front. Health Serv.*, vol. 5, Jul. 2025, doi: 10.3389/frhs.2025.1611746.

[12] J. H. Holmes and D. H. Howry, “Ultrasonic diagnosis of abdominal disease,” *Am. J. Dig. Dis.*, vol. 8, no. 1, pp. 12–32, Jan. 1963, doi: 10.1007/BF02233558.

[13] H. H. Holm and T. Mortensen, “Ultrasonic scanning in diagnosis of abdominal disease,” *Acta Chir. Scand.*, vol. 134, no. 5, pp. 333–341, 1968.

[14] S. H. Kim, B. I. Choi, K. W. Kim, K. H. Lee, and J. K. Han, “Extended Field-of-View Sonography,” *J. Ultrasound Med.*, vol. 22, no. 4, pp. 385–394, 2003, doi: 10.7863/jum.2003.22.4.385.

[15] D. H. Howry, “Technique used in ultrasonic visualization of soft tissues.,” in *Ultrasound in Biology and Medicine*, Washington, D.C.: American Institute of Biological Sciences, 1957, pp. 49–65.

[16] L. Lin *et al.*, “High-speed three-dimensional photoacoustic computed tomography for preclinical research and clinical translation,” *Nat. Commun.*, vol. 12, no. 1, Art. no. 1, 2021.

[17] S. Na *et al.*, “Massively parallel functional photoacoustic computed tomography of the human brain,” *Nat. Biomed. Eng.*, vol. 6, no. 5, pp. 584–592, May 2022, doi: 10.1038/s41551-021-00735-8.

[18] P. Wray, L. Lin, P. Hu, and L. V. Wang, “Photoacoustic computed tomography of human extremities,” *J. Biomed. Opt.*, vol. 24, no. 2, p. 026003, Feb. 2019, doi: 10.1117/1.JBO.24.2.026003.

[19] D. H. Howry and W. R. Bliss, “Ultrasonic visualization of soft tissue structures of the body,” *J. Lab. Clin. Med.*, vol. 40, no. 4, pp. 579–592, 1952.

[20] B. B. Goldberg, R. Gramiak, and A. K. Freimanis, “Early history of diagnostic ultrasound: the role of American radiologists,” *AJR Am J Roentgenol*, vol. 160, no. 1, pp. 189–194, 1993.

[21] D. H. Howry, J. H. Holmes, C. R. Cushman, and G. J. Posakony, “Ultrasonic visualization of living organs and tissues; with observations on some disease processes,” *Geriatrics*, vol. 10, no. 3, pp. 123–128, Mar. 1955.

[22] H. H. Holm, “Ultrasonic scanning in the diagnosis of space-occupying lesions of the upper abdomen,” *Br. J. Radiol.*, vol. 44, no. 517, pp. 24–36, Jan. 1971, doi: 10.1259/0007-1285-44-517-24.

[23] I. Donald, J. Macvicar, and T. G. Brown, “Investigation of abdominal masses by pulsed ultrasound,” *Lancet Lond. Engl.*, vol. 1, no. 7032, pp. 1188–1195, Jun. 1958, doi: 10.1016/s0140-6736(58)91905-6.

[24] J. Pinto, R. Azevedo, E. Pereira, and A. Caldeira, “Ultrasonography in Gastroenterology: The Need for Training,” *GE Port. J. Gastroenterol.*, vol. 25, no. 6, pp. 308–316, Nov. 2018, doi: 10.1159/000487156.

[25] M. Noorkoiv, K. Nosaka, and A. J. Blazevich, “Assessment of quadriceps muscle cross-sectional area by ultrasound extended-field-of-view imaging,” *Eur. J. Appl. Physiol.*, vol. 109, no. 4, pp. 631–639, Jul. 2010, doi: 10.1007/s00421-010-1402-1.

[26] L. Weng *et al.*, “US extended-field-of-view imaging technology.,” *Radiology*, vol. 203, no. 3, pp. 877–880, Jun. 1997, doi: 10.1148/radiology.203.3.9169720.

[27] E. E. Sauerbrei, “Extended field-of-view sonography: utility in clinical practice.,” *J. Ultrasound Med.*, vol. 18, no. 5, pp. 335–341, 1999, doi: 10.7863/jum.1999.18.5.335.

[28] J. Wiskin, D. T. Borup, S. A. Johnson, and M. Berggren, “Non-linear inverse scattering: High resolution quantitative breast tissue tomography,” *J. Acoust. Soc. Am.*, vol. 131, no. 5, pp. 3802–3813, May 2012, doi: 10.1121/1.3699240.

[29] L. Huang *et al.*, “Breast ultrasound tomography with two parallel transducer arrays,” in *Medical Imaging 2016: Physics of Medical Imaging*, SPIE, Mar. 2016, pp. 98–109. doi: 10.1117/12.2216531.

[30] Y. Zhang and L. Wang, “Video-Rate Ring-Array Ultrasound and Photoacoustic Tomography,” *IEEE Trans. Med. Imaging*, vol. 39, no. 12, pp. 4369–4375, Dec. 2020, doi: 10.1109/TMI.2020.3017815.

[31] N. Duric *et al.*, “Clinical breast imaging with ultrasound tomography: A description of the SoftVue system,” *J. Acoust. Soc. Am.*, vol. 135, no. 4_Supplement, p. 2155, Apr. 2014, doi: 10.1121/1.4876990.

[32] J. Wiskin *et al.*, “Full Wave 3D Inverse Scattering Transmission Ultrasound Tomography: Breast and Whole Body Imaging,” in *2019 IEEE International Ultrasonics Symposium (IUS)*, Oct. 2019, pp. 951–958. doi: 10.1109/ULTSYM.2019.8925778.

[33] J. Wiskin, B. Malik, C. Ruoff, N. Pirshafiey, M. Lenox, and J. Klock, “Whole-Body Imaging Using Low Frequency Transmission Ultrasound,” *Acad. Radiol.*, Feb. 2023, doi: 10.1016/j.acra.2023.01.018.

[34] E.-Y. Park *et al.*, “Fast volumetric ultrasound facilitates high-resolution 3D mapping of tissue compartments,” *Sci. Adv.*, vol. 9, no. 22, p. eadg8176, May 2023, doi: 10.1126/sciadv.adg8176.

[35] A. Kirillov *et al.*, “Segment Anything,” Apr. 05, 2023, *arXiv*: arXiv:2304.02643. doi: 10.48550/arXiv.2304.02643.

[36] T. L. Szabo, *Diagnostic Ultrasound Imaging: Inside Out*. Academic Press, 2004.

[37] IT’IS Foundation, “Tissue Properties Database V4.2.” IT’IS Foundation, 2024. doi: 10.13099/VIP21000-04-2.

[38] S. Ballestri, D. Romagnoli, F. Nascimbeni, G. Francica, and A. Lonardo, “Role of ultrasound in the diagnosis and treatment of nonalcoholic fatty liver disease and its complications,” *Expert Rev. Gastroenterol. Hepatol.*, vol. 9, no. 5, pp. 603–627, May 2015, doi: 10.1586/17474124.2015.1007955.

[39] M.-J. Lee, Y. Wu, and S. K. Fried, “Adipose tissue heterogeneity: Implication of depot differences in adipose tissue for obesity complications,” *Mol. Aspects Med.*, vol. 34, no. 1, pp. 1–11, Feb. 2013, doi: 10.1016/j.mam.2012.10.001.

[40] R. J. Kuczmarski, M. T. Fanelli, and G. G. Koch, “Ultrasonic assessment of body composition in obese adults: overcoming the limitations of the skinfold caliper,” *Am. J. Clin. Nutr.*, vol. 45, no. 4, pp. 717–724, Apr. 1987, doi: 10.1093/ajcn/45.4.717.

[41] K. H. Liu, Y. L. Chan, W. B. Chan, W. L. Kong, M. O. Kong, and J. C. N. Chan, “Sonographic measurement of mesenteric fat thickness is a good correlate with cardiovascular risk factors: comparison with subcutaneous and preperitoneal fat thickness, magnetic resonance imaging and anthropometric indexes,” *Int. J. Obes.*, vol. 27, no. 10, Art. no. 10, Oct. 2003, doi: 10.1038/sj.ijo.0802398.

[42] N. Anvery *et al.*, “Utility of high-resolution ultrasound in measuring subcutaneous fat thickness,” *Lasers Surg. Med.*, vol. 54, no. 9, pp. 1189–1197, 2022, doi: 10.1002/lsm.23604.

[43] J. Hoffmann *et al.*, “Measurement of subcutaneous fat tissue: reliability and comparison of caliper and ultrasound via systematic body mapping,” *Sci. Rep.*, vol. 12, no. 1, Art. no. 1, Sep. 2022, doi: 10.1038/s41598-022-19937-4.

[44] O. J. H. Harley and M. A. Pickford, “CT analysis of fat distribution superficial and deep to the Scarpa’s fascial layer in the mid and lower abdomen,” *J. Plast. Reconstr. Aesthet. Surg.*, vol. 66, no. 4, pp. 525–530, Apr. 2013, doi: 10.1016/j.bjps.2012.12.003.

[45] M. F. Abu-Hijleh, A. L. Roshier, Q. Al-Shboul, A. S. Dharap, and P. F. Harris, “The membranous layer of superficial fascia: evidence for its widespread distribution in the body,” *Surg. Radiol. Anat.*, vol. 28, no. 6, pp. 606–619, Dec. 2006, doi: 10.1007/s00276-006-0142-8.

[46] L. Lancerotto, C. Stecco, V. Macchi, A. Porzionato, A. Stecco, and R. De Caro, “Layers of the abdominal wall: anatomical investigation of subcutaneous tissue and superficial fascia,” *Surg. Radiol. Anat.*, vol. 33, no. 10, pp. 835–842, Dec. 2011, doi: 10.1007/s00276-010-0772-8.

[47] R. Graf and R. C. C. D. André Auersvald Ronald Rippel,Luiz Roberto Reis de Araújo, Luiz Henrique Camargo Bigarelli, and Claudio Luciano Franck, “Ultrasound-Assisted Liposuction: An Analysis of 348 Cases,” *Aesthetic Plast. Surg.*, vol. 27, no. 2, pp. 146–153, Apr. 2003, doi: 10.1007/s00266-002-1516-x.

[48] N. I. Sainani, R. S. Arellano, P. B. Shyn, D. A. Gervais, P. R. Mueller, and S. G. Silverman, “The challenging image-guided abdominal mass biopsy: established and emerging techniques ‘if you can see it, you can biopsy it,’” *Abdom. Imaging*, vol. 38, no. 4, pp. 672–696, Aug. 2013, doi: 10.1007/s00261-013-9980-0.

[49] W. C. Culp *et al.*, “Relative Ultrasonographic Echogenicity of Standard, Dimpled, and Polymeric-coated Needles,” *J. Vasc. Interv. Radiol.*, vol. 11, no. 3, pp. 351–358, Mar. 2000, doi: 10.1016/S1051-0443(07)61429-8.

[50] W. Li, Y. Wang, V. Nteziyaremye, H. Yamaguchi, and A. J. Shih, "Measurement of the Friction Force Inside the Needle in Biopsy," *J. Manuf. Sci. Eng.*, vol. 138, no. 031003, Oct. 2015, doi: 10.1115/1.4031050.

[51] N. Fulton, J. Buethe, J. Gollamudi, and M. Robbin, "Simulation-Based Training May Improve Resident Skill in Ultrasound-Guided Biopsy," *Am. J. Roentgenol.*, vol. 207, no. 6, pp. 1329–1333, Dec. 2016, doi: 10.2214/AJR.16.16161.

[52] N. Guberina *et al.*, "Radiation exposure during CT-guided biopsies: recent CT machines provide markedly lower doses," *Eur. Radiol.*, vol. 28, no. 9, pp. 3929–3935, Sep. 2018, doi: 10.1007/s00330-018-5350-1.

[53] M. Allocca, T. Kucharzik, and D. T. Rubin, "Intestinal Ultrasound in the Assessment and Management of Inflammatory Bowel Disease: Is It Ready for Standard Practice?," *Gastroenterology*, vol. 164, no. 6, pp. 851–855, May 2023, doi: 10.1053/j.gastro.2023.01.021.

[54] F. Rubino *et al.*, "Definition and diagnostic criteria of clinical obesity," *Lancet Diabetes Endocrinol.*, vol. 0, no. 0, Jan. 2025, doi: 10.1016/S2213-8587(24)00316-4.

[55] M. Barat *et al.*, "CT and MRI of abdominal cancers: current trends and perspectives in the era of radiomics and artificial intelligence," *Jpn. J. Radiol.*, vol. 42, no. 3, pp. 246–260, Mar. 2024, doi: 10.1007/s11604-023-01504-0.

[56] F. J. Siepel, B. Maris, M. K. Welleweerd, V. Groenhuis, P. Fiorini, and S. Stramigioli, "Needle and Biopsy Robots: a Review," *Curr. Robot. Rep.*, vol. 2, no. 1, pp. 73–84, Mar. 2021, doi: 10.1007/s43154-020-00042-1.

[57] R. C. Pfister, N. Papanicolaou, and I. C. Yoder, "Urinary extracorporeal shock wave lithotripsy: Equipment, techniques, and overview," *Urol. Radiol.*, vol. 10, no. 1, pp. 39–45, Dec. 1988, doi: 10.1007/BF02926533.

[58] C. Paverd, A. Martin, M. Rominger, and L. Ruby, "Assessment of ultrasound image quality in a reference phantom using gel and liquid standoff pads," *WFUMB Ultrasound Open*, vol. 2, no. 2, p. 100051, Dec. 2024, doi: 10.1016/j.wfumbo.2024.100051.

[59] C. Wang *et al.*, "Bioadhesive ultrasound for long-term continuous imaging of diverse organs," *Science*, vol. 377, no. 6605, pp. 517–523, Jul. 2022, doi: 10.1126/science.abo2542.

[60] J. A. Shepherd, B. K. Ng, M. J. Sommer, and S. B. Heymsfield, "Body composition by DXA," *Bone*, vol. 104, pp. 101–105, Nov. 2017, doi: 10.1016/j.bone.2017.06.010.

[61] C. Cueto *et al.*, "Stride: A flexible software platform for high-performance ultrasound computed tomography," *Comput. Methods Programs Biomed.*, vol. 221, p. 106855, Jun. 2022, doi: 10.1016/j.cmpb.2022.106855.

[62] M. O'Donnell, "Coded excitation system for improving the penetration of real-time phased-array imaging systems," *IEEE Trans. Ultrason. Ferroelectr. Freq. Control*, vol. 39, no. 3, pp. 341–351, May 1992, doi: 10.1109/58.143168.

[63] A. Kirillov *et al.*, "Segment Anything," presented at the Proceedings of the IEEE/CVF International Conference on Computer Vision, 2023, pp. 4015–4026. Accessed: Jan. 21, 2025. [Online]. Available: https://openaccess.thecvf.com/content/ICCV2023/html/Kirillov_Segment_Anything_ICCV_2023_paper.html

[64] S. B. Barnett, G. R. Ter Haar, M. C. Ziskin, H.-D. Rott, F. A. Duck, and K. Maeda, "International recommendations and guidelines for the safe use of diagnostic ultrasound in medicine," *Ultrasound Med. Biol.*, vol. 26, no. 3, pp. 355–366, Mar. 2000, doi: 10.1016/S0301-5629(00)00204-0.

[65] F. A. Duck, "The Meaning of Thermal Index (TI) and Mechanical Index (MI) Values," *BMUS Bull.*, vol. 5, no. 4, pp. 36–40, Nov. 1997, doi: 10.1177/1742271X9700500411.

[66] "The 2007 Recommendations of the International Commission on Radiological Protection. ICRP publication 103," *Ann. ICRP*, vol. 37, no. 2–4, pp. 1–332, 2007, doi: 10.1016/j.icrp.2007.10.003.

[67] J. I. Sabbione and D. Velis, "Automatic first-breaks picking: New strategies and algorithms," *GEOPHYSICS*, vol. 75, no. 4, pp. V67–V76, Jul. 2010, doi: 10.1190/1.3463703.

[68] D. Zhang, T. W. Fei, S. Han, C. Tsingas, Y. Luo, and H. Liu, "Automatic first-arrival picking workflow by global path tracing," *Geophysics*, Nov. 2021, doi: 10.1190/geo2021-0162.1.

[69] J. Tong, M. J. W. Povey, X. Zou, B. Ward, and C. P. Oates, "Speed of sound and density of ethanol-water mixture across the temperature range 10 to 50 degrees Celsius," *J. Phys. Conf. Ser.*, vol. 279, no. 1, p. 012023, Feb. 2011, doi: 10.1088/1742-6596/279/1/012023.

[70] C. F. Chen, D. E. Robinson, L. S. Wilson, K. A. Griffiths, A. Manoharan, and B. D. Doust, "Clinical sound speed measurement in liver and spleen in vivo<math><mtext>in vivo</mtext></math>," *Ultrason. Imaging*, vol. 9, no. 4, pp. 221–235, Oct. 1987, doi: 10.1016/0161-7346(87)90075-7.

[71] T. Lin, J. Ophir, and G. Potter, "Correlation of ultrasonic attenuation with pathologic fat and fibrosis in liver disease," *Ultrasound Med. Biol.*, vol. 14, no. 8, pp. 729–734, Jan. 1988, doi: 10.1016/0301-5629(88)90028-2.

[72] F. Simonetti, "A guided wave technique for needle biopsy under ultrasound guidance," in *Medical Imaging 2009: Visualization, Image-Guided Procedures, and Modeling*, SPIE, Mar. 2009, pp. 405–412. doi: 10.1117/12.811482.

[73] G. Cuatrecasas *et al.*, "Ultrasound measures of abdominal fat layers correlate with metabolic syndrome features in patients with obesity," *Obes. Sci. Pract.*, vol. 6, no. 6, pp. 660–667, 2020, doi: 10.1002/osp4.453.

[74] J. Shi *et al.*, "Comparison of microwave ablation and surgical resection for treatment of hepatocellular carcinomas conforming to Milan criteria," *J. Gastroenterol. Hepatol.*, vol. 29, no. 7, pp. 1500–1507, 2014, doi: 10.1111/jgh.12572.

[75] J. Dou *et al.*, "Microwave ablation vs. surgical resection for treatment naïve hepatocellular carcinoma within the Milan criteria: a follow-up of at least 5 years," *Cancer Biol. Med.*, vol. 19, no. 7, pp. 1078–1088, Sep. 2021, doi: 10.20892/j.issn.2095-3941.2020.0625.

[76] P. Prakash, "Theoretical Modeling for Hepatic Microwave Ablation," *Open Biomed. Eng. J.*, vol. 4, pp. 27–38, Feb. 2010, doi: 10.2174/1874120701004020027.

[77] C. J. Simon, D. E. Dupuy, and W. W. Mayo-Smith, "Microwave Ablation: Principles and Applications1," *RadioGraphics*, Oct. 2005, doi: 10.1148/rg.25si055501.

[78] M. B. Glassberg *et al.*, "Microwave ablation compared with radiofrequency ablation for treatment of hepatocellular carcinoma and liver metastases: a systematic review and meta-analysis," *OncoTargets Ther.*, vol. 12, pp. 6407–6438, 2019, doi: 10.2147/OTT.S204340.

[79] R. M. Mathy, A. Giannakis, M. Franke, A. Winiger, H.-U. Kauczor, and D.-H. Chang, "Factors Impacting Microwave Ablation Zone Sizes: A Retrospective Analysis," *Cancers*, vol. 16, no. 7, p. 1279, Mar. 2024, doi: 10.3390/cancers16071279.

[80] P. B. Shyn *et al.*, "Hepatic Microwave Ablation Zone Size: Correlation with Total Energy, Net Energy, and Manufacturer-Provided Chart Predictions," *J. Vasc. Interv. Radiol. JVIR*, vol. 27, no. 9, pp. 1389–1396, Sep. 2016, doi: 10.1016/j.jvir.2016.05.009.

[81] R. Geoghegan, G. ter Haar, K. Nightingale, L. Marks, and S. Natarajan, "Methods of monitoring thermal ablation of soft tissue tumors – A comprehensive review," *Med. Phys.*, vol. 49, no. 2, pp. 769–791, 2022, doi: 10.1002/mp.15439.

[82] F. Dong *et al.*, "Advancements in microwave ablation for tumor treatment and future directions," *iScience*, vol. 28, no. 4, Apr. 2025, doi: 10.1016/j.isci.2025.112175.

[83] X. Ying, S. Dong, Y. Zhao, Z. Chen, J. Jiang, and H. Shi, “Research Progress on Contrast-Enhanced Ultrasound (CEUS) Assisted Diagnosis and Treatment in Liver-Related Diseases,” *Int. J. Med. Sci.*, vol. 22, no. 5, pp. 1092–1108, Feb. 2025, doi: 10.7150/ijms.101789.

[84] F. Wang *et al.*, “RPCA-based thermoacoustic imaging for microwave ablation monitoring,” *Photoacoustics*, vol. 38, p. 100622, Aug. 2024, doi: 10.1016/j.pacs.2024.100622.

[85] L. Song *et al.*, “Thermoacoustic Imaging Using Single-Channel Data Acquisition System for Non-Invasive Assessment of Liver Microwave Ablation: A Feasibility Study,” *Photonics*, vol. 11, no. 9, Art. no. 9, Sep. 2024, doi: 10.3390/photonics11090807.

[86] A. L. Evans, R. L. Liu, C. Ma, and S. C. Hagness, “The Evolution of Microwave-Induced Thermoacoustic Signals Generated During Pulsed Microwave Ablation in Bovine Liver,” *IEEE J. Electromagn. RF Microw. Med. Biol.*, vol. 7, no. 3, pp. 273–280, Sep. 2023, doi: 10.1109/JERM.2023.3268553.

[87] A. L. Evans, C. Ma, and S. C. Hagness, “Microwave-induced thermoacoustic signal characteristics in a dynamic temperature environment,” *Biomed. Phys. Eng. Express*, vol. 8, no. 3, p. 035020, Apr. 2022, doi: 10.1088/2057-1976/ac60c6.

[88] L. V. Wang and H. Wu, *Biomedical optics: principles and imaging*. John Wiley & Sons, 2012.

[89] H. Nan and A. Arbabian, “Peak-power-limited frequency-domain microwave-induced thermoacoustic imaging for handheld diagnostic and screening tools,” *IEEE Trans. Microw. Theory Tech.*, vol. 65, no. 7, Art. no. 7, 2017.

[90] C. L. Brace, “Microwave Ablation Technology: What Every User Should Know,” *Curr. Probl. Diagn. Radiol.*, vol. 38, no. 2, pp. 61–67, Mar. 2009, doi: 10.1067/j.cpradiol.2007.08.011.

[91] D. C. Garrett, J. Xu, Y. Aborahama, G. Ku, K. Maslov, and L. V. Wang, “Whole-Body Human Ultrasound Tomography,” Jul. 17, 2024, *Research Square*. doi: 10.21203/rs.3.rs-4714949/v1.

[92] M. Xu and L. V. Wang, “Universal back-projection algorithm for photoacoustic computed tomography,” *Phys. Rev. E*, vol. 71, no. 1, Art. no. 1, 2005.

[93] A. Mohammadi, L. Bianchi, S. Asadi, and P. Saccomandi, “Measurement of Ex Vivo Liver, Brain and Pancreas Thermal Properties as Function of Temperature,” *Sensors*, vol. 21, no. 12, p. 4236, Jun. 2021, doi: 10.3390/s21124236.

[94] N. P. Silva, A. Bottiglieri, R. C. Conceição, M. O’Halloran, and L. Farina, “Characterisation of Ex Vivo Liver Thermal Properties for Electromagnetic-Based Hyperthermic Therapies,” *Sensors*, vol. 20, no. 10, p. 3004, May 2020, doi: 10.3390/s20103004.

[95] V. Lopresto, R. Pinto, G. A. Lovisolo, and M. Cavagnaro, “Changes in the dielectric properties of ex vivo bovine liver during microwave thermal ablation at 2.45 GHz,” *Phys. Med. Biol.*, vol. 57, no. 8, p. 2309, Mar. 2012, doi: 10.1088/0031-9155/57/8/2309.

[96] F. C. Henriques, “Studies of thermal injury; the predictability and the significance of thermally induced rate processes leading to irreversible epidermal injury,” *Arch. Pathol.*, vol. 43, no. 5, pp. 489–502, May 1947.

[97] B.-M. Kim, S. L. Jacques, S. Rastegar, S. Thomsen, and M. Motamedi, “Nonlinear finite-element analysis of the role of dynamic changes in blood perfusion and optical properties in laser coagulation of tissue,” *IEEE J. Sel. Top. Quantum Electron.*, vol. 2, no. 4, pp. 922–933, Dec. 1996, doi: 10.1109/2944.577317.

[98] K. Samimi, J. K. White, C. L. Brace, and T. Varghese, “Monitoring Microwave Ablation of Ex-Vivo Bovine Liver Using Ultrasonic Attenuation Imaging,” *Ultrasound Med. Biol.*, vol. 43, no. 7, pp. 1441–1451, Jul. 2017, doi: 10.1016/j.ultrasmedbio.2017.03.010.

[99] H. H. Pennes, “Analysis of tissue and arterial blood temperatures in the resting human forearm,” *J. Appl. Physiol.*, vol. 1, no. 2, Art. no. 2, 1948.

[100] C. Tucci, M. Trujillo, E. Berjano, M. Iasiello, A. Andreozzi, and G. P. Vanoli, “Pennes’ bioheat equation vs. porous media approach in computer modeling of radiofrequency tumor ablation,” *Sci. Rep.*, vol. 11, no. 1, p. 5272, 2021.

[101] U. Techavipoo, T. Varghese, Q. Chen, T. A. Stiles, J. A. Zagzebski, and G. R. Frank, “Temperature dependence of ultrasonic propagation speed and attenuation in excised canine liver tissue measured using transmitted and reflected pulses,” *J. Acoust. Soc. Am.*, vol. 115, no. 6, pp. 2859–2865, Jun. 2004, doi: 10.1121/1.1738453.

[102] Z. Ji and C. L. Brace, “Expanded modeling of temperature-dependent dielectric properties for microwave thermal ablation,” *Phys. Med. Biol.*, vol. 56, no. 16, pp. 5249–5264, Aug. 2011, doi: 10.1088/0031-9155/56/16/011.

[103] J. Crank, *The Mathematics of Diffusion*. Clarendon Press, 1979.

[104] G. Iddan, G. Meron, A. Glukhovsky, and P. Swain, “Wireless capsule endoscopy,” *Nature*, vol. 405, no. 6785, pp. 417–417, May 2000, doi: 10.1038/35013140.

[105] T. Nakamura and A. Terano, “Capsule endoscopy: past, present, and future,” *J. Gastroenterol.*, vol. 43, no. 2, pp. 93–99, Feb. 2008, doi: 10.1007/s00535-007-2153-6.

[106] B. Akpunonu, J. Hummell, J. D. Akpunonu, and S. Ud Din, “Capsule endoscopy in gastrointestinal disease: Evaluation, diagnosis, and treatment,” *Cleve. Clin. J. Med.*, vol. 89, no. 4, pp. 200–211, Apr. 2022.

[107] Z. Liao, R. Gao, C. Xu, and Z.-S. Li, “Indications and detection, completion, and retention rates of small-bowel capsule endoscopy: a systematic review,” *Gastrointest. Endosc.*, vol. 71, no. 2, pp. 280–286, Feb. 2010, doi: 10.1016/j.gie.2009.09.031.

[108] M. Pennazio *et al.*, “Small-bowel capsule endoscopy and device-assisted enteroscopy for diagnosis and treatment of small-bowel disorders: European Society of Gastrointestinal Endoscopy (ESGE) Clinical Guideline,” *Endoscopy*, vol. 47, no. 4, pp. 352–376, Apr. 2015, doi: 10.1055/s-0034-1391855.

[109] G. Cummins *et al.*, “Gastrointestinal diagnosis using non-white light imaging capsule endoscopy,” *Nat. Rev. Gastroenterol. Hepatol.*, vol. 16, no. 7, pp. 429–447, Jul. 2019, doi: 10.1038/s41575-019-0140-z.

[110] S. H. Kim and H. J. Chun, “Capsule Endoscopy: Pitfalls and Approaches to Overcome,” *Diagnostics*, vol. 11, no. 10, p. 1765, Sep. 2021, doi: 10.3390/diagnostics11101765.

[111] B. Sun, J. Liu, S. Li, J. F. Lovell, and Y. Zhang, “Imaging of Gastrointestinal Tract Ailments,” *J. Imaging*, vol. 9, no. 6, p. 115, Jun. 2023, doi: 10.3390/jimaging9060115.

[112] J. H. Lee, G. Traverso, D. Ibarra-Zarate, D. S. Boning, and B. W. Anthony, “Ex Vivo and In Vivo Imaging Study of Ultrasound Capsule Endoscopy,” *J. Med. Devices*, vol. 14, no. 021005, Mar. 2020, doi: 10.1115/1.4046352.

[113] H. S. Lay *et al.*, “Progress towards a multi-modal capsule endoscopy device featuring microultrasound imaging,” in *2016 IEEE International Ultrasonics Symposium (IUS)*, Sep. 2016, pp. 1–4. doi: 10.1109/ULTSYM.2016.7728692.

[114] K. Huang *et al.*, “High-speed photoacoustic and ultrasonic computed tomography of the breast tumor for early diagnosis with enhanced accuracy,” *Sci. Adv.*, vol. 11, no. 41, p. eadz2046, Oct. 2025, doi: 10.1126/sciadv.adz2046.

[115] R. Ansari, E. Z. Zhang, A. E. Desjardins, and P. C. Beard, “All-optical forward-viewing photoacoustic probe for high-resolution 3D endoscopy,” *Light Sci. Appl.*, vol. 7, no. 1, p. 75, Oct. 2018, doi: 10.1038/s41377-018-0070-5.

[116] H. He *et al.*, “Capsule optoacoustic endoscopy for esophageal imaging,” *J. Biophotonics*, vol. 12, no. 10, p. e201800439, 2019, doi: 10.1002/jbio.201800439.

[117] D. C. Garrett, J. Xu, Y. Aborahama, G. Ku, K. Maslov, and L. V. Wang, “Whole Cross-Sectional Human Ultrasound Tomography,” Jan. 31, 2025, *arXiv*: arXiv:2307.00110. doi: 10.48550/arXiv.2307.00110.

[118] L. L. Zwinger *et al.*, “CapsoCam SV-1 Versus PillCam SB 3 in the Detection of Obscure Gastrointestinal Bleeding: Results of a Prospective Randomized Comparative Multicenter Study,” *J. Clin. Gastroenterol.*, vol. 53, no. 3, p. e101, Mar. 2019, doi: 10.1097/MCG.0000000000000994.

[119] C.-C. Su *et al.*, “Capsule Endoscopy: Current Trends, Technological Advancements, and Future Perspectives in Gastrointestinal Diagnostics,” *Bioengineering*, vol. 12, no. 6, p. 613, Jun. 2025, doi: 10.3390/bioengineering12060613.

[120] D. K. Cai, A. Neyer, R. Kuckuk, and H. M. Heise, “Optical absorption in transparent PDMS materials applied for multimode waveguides fabrication,” *Opt. Mater.*, vol. 30, no. 7, pp. 1157–1161, Mar. 2008, doi: 10.1016/j.optmat.2007.05.041.

[121] G. Xu, “Acoustic Characterization of Polydimethylsiloxane for Microscale Acoustofluidics,” *Phys. Rev. Appl.*, vol. 13, no. 5, 2020, doi: 10.1103/PhysRevApplied.13.054069.

[122] N. K. Mandsberg, J. F. Christfort, K. Kamguyan, A. Boisen, and S. K. Srivastava, “Orally ingestible medical devices for gut engineering,” *Adv. Drug Deliv. Rev.*, vol. 165–166, pp. 142–154, Jan. 2020, doi: 10.1016/j.addr.2020.05.004.

[123] A. Ibrahim, M. Meng, and M. Kiani, “A Comprehensive Comparative Study on Inductive and Ultrasonic Wireless Power Transmission to Biomedical Implants,” *IEEE Sens. J.*, vol. 18, no. 9, pp. 3813–3826, May 2018, doi: 10.1109/JSEN.2018.2812420.

[124] P. Nadeau *et al.*, “Prolonged energy harvesting for ingestible devices,” *Nat. Biomed. Eng.*, vol. 1, no. 3, p. 0022, Feb. 2017, doi: 10.1038/s41551-016-0022.

[125] S.-Y. Yang *et al.*, “Powering Implantable and Ingestible Electronics,” *Adv. Funct. Mater.*, vol. 31, no. 44, p. 2009289, 2021, doi: 10.1002/adfm.202009289.

[126] K. Uchino, *Essentials Of Piezoelectric Energy Harvesting*. World Scientific, 2021.

[127] K. Möller *et al.*, “Gastrointestinal Ultrasound: Measurements and Normal Findings - What Do You Need to Know?,” *Dig. Dis. Basel Switz.*, vol. 43, no. 3, pp. 300–335, 2025, doi: 10.1159/000544043.

[128] M. Monge, A. Lee-Gosselin, M. G. Shapiro, and A. Emami, “Localization of microscale devices in vivo using addressable transmitters operated as magnetic spins,” *Nat. Biomed. Eng.*, vol. 1, no. 9, pp. 736–744, Sep. 2017, doi: 10.1038/s41551-017-0129-2.

[129] S. Sharma *et al.*, “Location-aware ingestible microdevices for wireless monitoring of gastrointestinal dynamics,” *Nat. Electron.*, vol. 6, no. 3, pp. 242–256, Mar. 2023, doi: 10.1038/s41928-023-00916-0.

[130] J. Hummel *et al.*, “Evaluation of a new electromagnetic tracking system using a standardized assessment protocol,” *Phys. Med. Biol.*, vol. 51, no. 10, p. N205, Apr. 2006, doi: 10.1088/0031-9155/51/10/N01.

[131] C. Wang *et al.*, “Monitoring of the central blood pressure waveform via a conformal ultrasonic device,” *Nat. Biomed. Eng.*, vol. 2, no. 9, pp. 687–695, Sep. 2018, doi: 10.1038/s41551-018-0287-x.

[132] A. Koulaouzidis and K. J. Dabos, “Looking forwards: not necessarily the best in capsule endoscopy?,” *Ann. Gastroenterol. Q. Publ. Hell. Soc. Gastroenterol.*, vol. 26, no. 4, pp. 365–367, 2013.

[133] L. V. Wang and Q. Shen, “Sonoluminescent tomography of strongly scattering media,” *Opt. Lett.*, vol. 23, no. 7, pp. 561–563, Apr. 1998, doi: 10.1364/OL.23.000561.

[134] Q. Shen and L. V. Wang, “Two-dimensional imaging of dense tissue-simulating turbid media by use of sonoluminescence,” *Appl. Opt.*, vol. 38, no. 1, pp. 246–252, Jan. 1999, doi: 10.1364/AO.38.000246.

[135] A. Khaleghi, A. Hasanvand, and I. Balasingham, “Radio Frequency Backscatter Communication for High Data Rate Deep Implants,” *IEEE Trans. Microw. Theory Tech.*, vol. 67, no. 3, pp. 1093–1106, Mar. 2019, doi: 10.1109/TMTT.2018.2886844.

[136] F. Alrashdan *et al.*, “Robust Magnetoelectric Backscatter Communication System for Bioelectronic Implants,” *Res. Sq.*, p. rs.3.rs-5463005, Dec. 2024, doi: 10.21203/rs.3.rs-5463005/v1.

[137] A. M. Winkler, K. Maslov, and L. V. Wang, “Noise-equivalent sensitivity of photoacoustics,” *J. Biomed. Opt.*, vol. 18, no. 9, p. 097003, Sep. 2013, doi: 10.1117/1.JBO.18.9.097003.

[138] D. C. Garrett and L. V. Wang, “Acoustic sensing with light,” *Nat. Photonics*, vol. 15, no. 5, pp. 324–326, May 2021, doi: 10.1038/s41566-021-00804-z.

[139] R. Krimholtz, D. A. Leedom, and G. L. Matthaei, “New equivalent circuits for elementary piezoelectric transducers,” *Electron. Lett.*, vol. 6, no. 13, pp. 398–399, Jun. 1970, doi: 10.1049/el:19700280.

[140] J. M. Rothberg *et al.*, “Ultrasound-on-chip platform for medical imaging, analysis, and collective intelligence,” *Proc. Natl. Acad. Sci.*, vol. 118, no. 27, p. e2019339118, Jul. 2021, doi: 10.1073/pnas.2019339118.

[141] L. Zhang, W. Du, J.-H. Kim, C.-C. Yu, and C. Dagdeviren, “An Emerging Era: Conformable Ultrasound Electronics,” *Adv. Mater.*, vol. 36, no. 8, p. 2307664, 2024, doi: 10.1002/adma.202307664.

[142] L. Li *et al.*, “Single-impulse panoramic photoacoustic computed tomography of small-animal whole-body dynamics at high spatiotemporal resolution,” *Nat. Biomed. Eng.*, vol. 1, no. 5, Art. no. 5, May 2017, doi: 10.1038/s41551-017-0071.

[143] L. Lin *et al.*, “Single-breath-hold photoacoustic computed tomography of the breast,” *Nat. Commun.*, vol. 9, no. 1, Art. no. 1, Jun. 2018, doi: 10.1038/s41467-018-04576-z.

[144] K. Sastry *et al.*, “A method for the geometric calibration of ultrasound transducer arrays with arbitrary geometries,” *Photoacoustics*, vol. 32, p. 100520, Aug. 2023, doi: 10.1016/j.pacs.2023.100520.

[145] J.-P. Monchalin, “Optical detection of ultrasound,” *IEEE Trans. Ultrason. Ferroelectr. Freq. Control*, vol. 33, pp. 485–499, Sep. 1986.

[146] W. J. Westerveld *et al.*, “Sensitive, small, broadband and scalable optomechanical ultrasound sensor in silicon photonics,” *Nat. Photonics*, pp. 1–5, Mar. 2021, doi: 10.1038/s41566-021-00776-0.

[147] A. M. Winkler, K. I. Maslov, and L. V. Wang, “Noise-equivalent sensitivity of photoacoustics,” *J. Biomed. Opt.*, vol. 18, no. 9, p. 097003, Sep. 2013, doi: 10.1117/1.JBO.18.9.097003.

[148] G. Wissmeyer, M. A. Pleitez, A. Rosenthal, and V. Ntziachristos, “Looking at sound: optoacoustics with all-optical ultrasound detection,” *Light Sci. Appl.*, vol. 7, no. 1, p. 53, Aug. 2018, doi: 10.1038/s41377-018-0036-7.

[149] S.-W. Huang *et al.*, “Low-noise wideband ultrasound detection using polymer microring resonators,” *Appl. Phys. Lett.*, vol. 92, no. 19, p. 193509, May 2008, doi: 10.1063/1.2929379.

[150] J. A. Guggenheim *et al.*, “Ultrasensitive plano-concave optical microresonators for ultrasound sensing,” *Nat. Photonics*, vol. 11, no. 11, pp. 714–719, Nov. 2017, doi: 10.1038/s41566-017-0027-x.

[151] R. Shnaiderman, G. Wissmeyer, O. Ülgen, Q. Mustafa, A. Chmyrov, and V. Ntziachristos, “A submicrometre silicon-on-insulator resonator for ultrasound detection,” *Nature*, vol. 585, no. 7825, Art. no. 7825, Sep. 2020, doi: 10.1038/s41586-020-2685-y.

[152] L. Chrostowski and M. Hochberg, *Silicon Photonics Design: From Devices to Systems*. Cambridge University Press, 2015.

[153] C. S. Desilets, J. D. Fraser, and G. S. Kino, “The design of efficient broad-band piezoelectric transducers,” *IEEE Trans. Sonics Ultrason.*, vol. 25, no. 3, pp. 115–125, May 1978, doi: 10.1109/T-SU.1978.31001.

[154] P. Hu, L. Li, L. Lin, and L. V. Wang, “Spatiotemporal Antialiasing in Photoacoustic Computed Tomography,” *IEEE Trans. Med. Imaging*, vol. 39, no. 11, pp. 3535–3547, Nov. 2020, doi: 10.1109/TMI.2020.2998509.

[155] R. Ansari, E. Z. Zhang, A. E. Desjardins, and P. C. Beard, “All-optical forward-viewing photoacoustic probe for high-resolution 3D endoscopy,” *Light Sci. Appl.*, vol. 7, no. 1, Art. no. 1, Oct. 2018, doi: 10.1038/s41377-018-0070-5.